Multi-Messenger Astronomy with H.E.S.S: the Starburst Galaxy NGC 253 and the Search for Short Time-Scale Transients

von

Clemens Hoischen

Dissertation

vorgelegt der

Mathematisch Naturwissenschaftlichen Fakultät
der Universität Potsdam

im Juni 2018

angefertigt in der Arbeitsgruppe
für experimentelle Astroteilchenphysik

1. Gutachter: Prof. Dr. Christian Stegmann
2. Gutachter: Prof. Dr. Alexander Kappes
3. Gutachter: Prof. Dr. Martin Pohl

Published online at the
Institutional Repository of the University of Potsdam:
https://doi.org/10.25932/publishup-42452
https://nbn-resolving.org/urn:nbn:de:kobv:517-opus4-424521

Selbstständigkeitserklärung

Hiermit erkläre ich, dass ich die vorliegende Arbeit selbstständig und ohne fremde Hilfe verfasst und keine anderen Hilfsmittel als angegeben verwendet habe.

Insbesondere versichere ich, dass ich alle wörtlichen und sinngemäßen Übernahmen aus anderen Werken als solche kenntlich gemacht habe.

Clemens Hoischen

Potsdam,

Abstract

γ-ray astronomy has proven to provide unique insights into cosmic-ray accelerators in the past few decades. By combining information at the highest photon energies with the entire electromagnetic spectrum in multi-wavelength studies, detailed knowledge of non-thermal particle populations in astronomical objects and systems has been gained: Many individual classes of γ-ray sources could be identified inside our galaxy and outside of it. Different sources were found to exhibit a wide range of temporal evolution, ranging from seconds to stable behaviours over many years of observations. With the dawn of both neutrino- and gravitational wave astronomy, additional messengers have come into play over the last years. This development presents the advent of multi-messenger astronomy: a novel approach not only to search for sources of cosmic rays, but for astronomy in general.

In this thesis, both traditional multi-wavelength studies and multi-messenger studies will be presented. They were carried out with the H.E.S.S. experiment, an imaging air Cherenkov telescope array located in the Khomas Highland of Namibia. H.E.S.S. has entered its second phase in 2012 with the addition of a large, fifth telescope. While the initial array was limited to the study of γ-rays with energies above 100 GeV, the new instrument allows to access γ-rays with energies down to a few tens of GeV.

Strengths of the multi-wavelength approach will be demonstrated at the example of the galaxy NGC 253, which is undergoing an episode of enhanced star-formation. The γ-ray emission will be discussed in light of all the information on this system available from radio, infrared and X-rays. These wavelengths reveal detailed information on the population of supernova remnants, which are suspected cosmic-ray accelerators. A broad-band γ-ray spectrum is derived from H.E.S.S. and *Fermi*-LAT data. The improved analysis of H.E.S.S. data provides a measurement which is no longer dominated by systematic uncertainties. The long-term behaviour of cosmic rays in the starburst galaxy NGC 253 is finally characterised.

In contrast to the long time-scale evolution of a starburst galaxy, multi-messenger studies are especially intriguing when shorter time-scales are being probed. A prime example of a short time-scale transient are Gamma Ray Bursts. The efforts to understand this phenomenon effectively founded the branch of γ-ray astronomy. The multi-messenger approach allows for the study of illusive phenomena such as Gamma Ray Bursts and other transients using electromagnetic radiation, neutrinos, cosmic rays and gravitational waves contemporaneously. With contemporaneous observations getting more important just recently, the execution of such observation campaigns still presents a big challenge due to the different limitations and strengths of the infrastructures.

An alert system for transient phenomena has been developed over the course of this thesis for H.E.S.S. It aims to address many follow-up challenges in order to maximise the science return of the new large telescope, which is able to repoint much faster than the initial four telescopes. The system allows for fully automated observations based on scientific alerts from any wavelength or messenger and allows H.E.S.S. to participate in multi-messenger campaigns. Utilising this new system, many interesting multi-messenger observation campaigns have been performed. Several highlight observations with H.E.S.S. are analysed, presented and discussed in this work. Among them are observations of Gamma Ray Bursts with low latency and low energy threshold, the follow-up of a neutrino candidate in spatial coincidence with a flaring active galactic nucleus and of the merger of two neutron stars, which was revealed by the coincidence of gravitational waves and a Gamma-Ray Burst.

Kurzfassung

Die Gammaastronomie hat sich in den letzten Jahrzehnten als eine wichtige Disziplin für die Suche nach den Beschleunigern der kosmischen Strahlung erwiesen. Dabei ergänzt die Gamma-Strahlung das Bild, welches wir aus Multi-Wellenlängen Studien gewonnen haben ausgezeichnet. Kürzlich sind die beiden neuen astronomischen Boten, Neutrinos und Gravitationswellen, zugänglich geworden. Diese liefern tiefere und neue Erkenntnisse über wichtige Prozesse im Universum und markiert die Geburt der Multi-Botenteilchen Astronomie: eine Form der Astronomie welche Gebrauch vom gesamten elektromagnetischen Spektrum, sowie von kosmischer Strahlung, Neutrinos und auch Gravitationswellen macht.

In dieser Arbeit werden sowohl traditionelle Multi-Wellenlängen Studien, als auch neue Multi-Botenteilchen Studien präsentiert. Dabei wird gebrauch von Daten des H.E.S.S. Experiments gemacht: eine Gruppe von abbildenden Cherenkov-Teleskopen in Namibia. Im Jahr 2012 ist H.E.S.S. in die zweite Operationsphase eingetreten: ein neues, großes Teleskop wurde hinzugefügt welches es erlaubt Gamma-Strahlung mit Energien in der Größenordnung von wenigen zehn GeV zu messen.

Der Multi-Wellenlängen Ansatz wird an dem Beispiel der Galaxie NGC 253 demonstriert. Diese Galaxy befindet sich in einer Episode mit erhöhter Stern-Erzeugungsrate. Die Gamma-Strahlung, welche von dieser Galaxie gemessen wurde, wird im Zusammenhang mit Informationen über dieses System diskutiert die aus Radio, Infrarot und Röntgenstrahlung gewonnen wurden. Diese geben Aufschluss über die große Population von Supernova Überresten, welche exzellente Kandidaten für Beschleuniger von kosmischer Strahlung sind. Ein Breitband Gamma-Strahlungs-Spektrum wurde mit Hilfe von H.E.S.S. und *Fermi*-LAT Daten zusammengesetzt. Die verbesserte Analyse der H.E.S.S. Daten erzielt eine Messung die nicht mehr von systematischen Unsicherheiten dominiert wird. Anhand des kombinierte Spektrum wird das Verhalten der kosmischen Strahlung in der Galaxy NGC 253 diskutiert.

Im Gegensatz zum Langzeitverhalten von einer Galaxie wie NGC 253, erweisen sich Multi-Botenteilchen Studien als besonders interessant für transiente Phänomene. Gleichzeitige Beobachtungen von Gamma-Strahlung und weiteren Botenteilchen können neue Erkenntnisse über beispielsweise Gammastrahlungsausbrüche oder die Quellen von Astrophysikalischen Neutrinos geben. Da gleichzeitige Beobachtungen in der Gammaastronomie erst seit kurzem immer wichtiger werden, stellen solche Beobachtungskampagnen aktuell eine Herausforderung dar. Um die Herausforderungen zu überwinden und gleichzeitig die wissenschaftlichen Studien, für die das neue große Teleskop von H.E.S.S. besonders geeignet ist, zu maximieren, wurde im Rahmen dieser Arbeit ein Alarmsystem für transiente Ereignisse entwickelt. Mit der Hilfe dieses neuen Systems konnten bereits viele interessante Beobachtungen durchgeführt werden. Einige der Interessantesten werden in dieser Arbeit vorgestellt und diskutiert. Darunter sind Beobachtungen von Gammastrahlungsausbrüchen mit kleinen zeitlichen Latenzen und niedriger Energieschwelle, die Nachbeobachtung eines Neutrino Kandidaten welcher räumlich mit einem Aktiven Galaxien Kern, der vorübergehend eine erhöhte Aktivität aufwies, zusammenfiel, sowie Beobachtungen vom Verschmelzen zweier Neutronensterne, was durch Gravitationswellen und einen gleichzeitigen Gammastrahlungsausbruch identifiziert werden konnte.

Table of Contents

TABLE OF CONTENTS

Chapter 1

γ-ray Astronomy

γ-ray astronomy is a relatively new field of astronomy. While modern astronomy dates back more than 400 years to Copernicus, γ-ray astronomy was born only about 50 years ago. The γ-ray energy domain relates to photons with energies above 1 MeV, a factor $\sim 10^6$ more than visible light.

Production mechanisms of γ-rays are π^0 decay, bremsstrahlung and inverse Compton scattering, all processes which are well measurable in the laboratory. Accordingly, γ-ray measurements are able to probe particle physics processes in astronomical systems and objects. What makes the γ-ray window unique compared to lower energy wavebands of the electromagnetic spectrum is the need for non-thermal particle populations. Non-thermal refers to the fact that the energy distribution of the particles giving rise to γ-rays can not be explained in terms of heating. Efficient particle acceleration mechanisms are therefore required. The existence of such particles has first been shown by Victor Francis Hess in 1912 with his detection of cosmic rays [1]. The search for the sources of these cosmic rays is a big field of astro particle physics ever since and presents a central scientific questions of modern γ-ray astronomy. The large potential of γ-rays in this endeavour was recognised already before the advent of γ-ray astronomy. As γ-rays are charge neutral, they are not deflected by interstellar magnetic fields and point back to their production sites – the astrophysical particle accelerators.

The landscape of astronomy rapidly evolved in recent years: The birth of both neutrino and gravitational wave astronomy were just witnessed. This opens new frontiers in astronomy with the possibility to utilise all known astrophysical messengers, including gravitational waves, neutrinos, cosmic rays and of course the entire electromagnetic spectrum up to γ-ray energies. All individual fields are strongly driven by instrumental advancements. The multi-messenger era presents a change to this tradition as the collaboration between infrastructures and communities becomes more and more important.

Modern γ-ray experiments probe the γ-ray sky in the energy range from MeV to GeV in space and from tens of GeV to $\sim$ 100 TeV on the ground. An introduction to space based γ-ray astronomy will be given in section 1.1. The discipline of ground based γ-ray astronomy will be introduced in section 1.2.

Well over 3000 individual γ-ray sources are detected to date. Many classes of γ-ray emitting sources are well established by now. They are usually grouped into galactic (e.g. pulsar wind nebulae, supernova remnants, pulsars and binaries, stellar clusters) and extragalactic γ-ray sources (e.g. active galactic nuclei, starburst galaxies, gamma ray bursts). Another way to distinguish γ-ray sources lies in the time domain. Most of the known γ-ray sources

evolve on astronomical time scales. Others exist for only a short period, which in some cases can be less than a second. This allows to distinguish between stable and transient sources. Known classes of γ-ray transients are gamma ray bursts, flares from active galactic nuclei and novae. All these source classes are known to emit γ-rays mostly at energies of $\mathcal{O}(GeV)$, although flares from active galactic nuclei are commonly found to extend into the energy range of multiple 100 GeV.

The work presented here was carried out for the H.E.S.S. experiment and are focused on ground based γ-ray astronomy which probes γ-rays with energies above a few tens of GeV. This thesis will explore the entire range of time scales of γ-ray sources. Two main science topics will be addressed in this work:

The first topic is the γ-ray emission from the galaxy NGC 253, which is undergoing an episode of enhanced star formation. The typical timescale of such star formation episodes is in the order of a Gyr, making starburst galaxies a prime candidate of a stable source. The emission is believed to originate from hadronic cosmic rays which are accelerated in the numerous supernova remnants in the starburst region. This scenario will be discussed based on the analysis of H.E.S.S. and *Fermi*-LAT data. Details will be presented in chapter 2.

The second and bulk part of this thesis discusses improved strategies of probing transient targets with short time scales. Gamma ray bursts will be discussed in chapter 3, as an example phenomenon of short time scale transients in order to highlight requirements and discuss difficulties in follow-up strategies with experiments like H.E.S.S. The transients alert system, which has been developed and commissioned for the H.E.S.S. experiment as part of this thesis, will be presented in chapter 4. Finally, selected highlights from multi-messenger follow-up observations carried out with the novel transient alert system will be described and discussed in chapter 5.

1.1 γ-ray Astronomy in Space with *Fermi*

First light of γ-ray Astronomy dates back to 1965, when a few γ-ray candidates were detected by the Explorer XI mission [2]. The first sources could be identified only two years later in 1967. These *Gamma Ray Bursts* (GRBs) were detected by the Vela satellites, which were monitoring nuclear weapon tests from space. These results were only published in 1973 [3] due to their military classification. In 1968, only one year after the first GRB detection, Clark et al. [4] announced the detection of γ-rays from the direction of the galactic centre. Constructions for the first ground based γ-ray experiment started the same year.

Efficient detection of γ-ray sources was first possible with the Compton Gamma Ray Observatory (CGRO), which was launched in April 1991. While previous experiments continued to detect γ-ray emission from a hand full of sources, CGRO provided sizeable samples of γ-ray sources with three main instruments:

The Burst And Transient Source Experiment (BATSE) [5]: A specialised experiment to detect GRBs and other transient sources in the keV to MeV energy range. The Imaging Compton Telescope (COMPTEL) [6]: An imaging telescope sensitive in the energy range from 0.8 to 30 MeV, in which γ-ray lines attributed to radioactive isotope decays can be measured (see e.g. [7]). The Energetic Gamma Ray Experiment Telescope (EGRET) [8]: The predecessor to *Fermi*-LAT, covering the energy range from 20 MeV to 30 GeV with $\sim 10'$ localisation accuracy for bright sources and a large field of view. EGRET alone detected ~ 270 distinct γ-ray sources [9].

The *Fermi* mission is today's most successful space based γ-ray instrument. It employs improved instrumentation based on the BATSE and EGRET detectors. In its 8 years of operation, it managed to tenfold the number of individual γ-ray sources compared to EGRET. The instruments onboard the *Fermi* mission are able to detect γ-rays with energies from 8 keV to 300 GeV with a close to 100 % duty cycle and a large field of view. A brief introduction to the different instruments on board the *Fermi* satellite, which is depicted in Fig 1.1, will be given here. Data from the *Fermi* mission are commonly employed jointly with data from ground based γ-ray instruments like H.E.S.S.

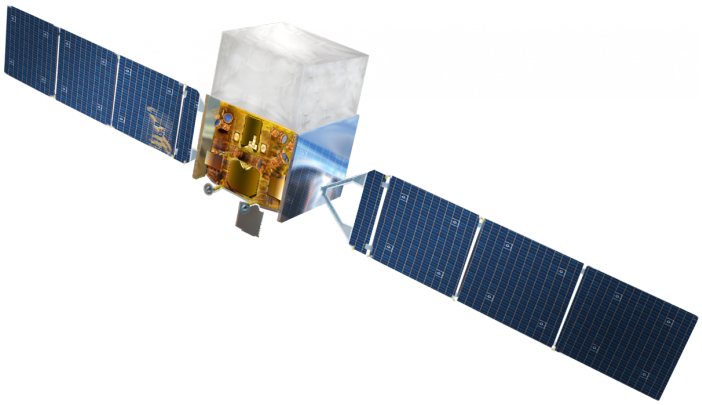

Figure 1.1: Artist illustration of the *Fermi* satellite. Figure from NASA.

The Large Area Telescope on board the *Fermi* satellite

The Large Area Telescope (LAT) [10] on board the Fermi satellite, launched in 2008, has contributed most of todays known γ-ray sources. It increased the number of sources detected by its predecessor EGRET from roughly 300 to more than 3000. The energy range of *Fermi*-LAT spans from $\sim 30\,\mathrm{MeV}$ to $300\,\mathrm{GeV}$ with the high-energy range constrains for Fermi-LAT being due to its size and weight (as usual for space instruments). With an effective area in the order of $\mathcal{O}(1\,\mathrm{m}^2\mathrm{sr})$ the expected rate of γ-rays above $100\,\mathrm{GeV}$ is just a few per year.

The Large Area Telescope consists of three key subsystems: The anti-coincidence detector, tracker and calorimeter. A schematic overview of all components of *Fermi*-LAT is shown in Fig A.1 in the appendix. For a complete review of the Fermi Satellite, the reader is referred to Atwood et al. [10, and therein]for the LAT. In addition to the LAT, the Fermi satellite is hosting the Gamma-ray Burst Monitor (GBM), a specialised all sky instrument for the detection of GRBs. For a full description of this instrument the reader is referred to Meegan et al. [11, and therin]. In the following, only a basic description of the different sub-detectors will be given.

The Anti-Coincidence Detector

The anti-coincidence detector (ACD) consists of plastic scintillator tiles that are connected with wavelength shifting fibers to photomultipliers. Its task is to shield the instrument from the abundant charged cosmic rays. While neutral γ-rays can pass trough the ACD freely, charged particles like protons will emit scintillation light that is collected and enhanced in

photomultiplier tubes. This provides a first way to distinguish between hadrons and gamma-rays. The ACD covers the entire tracker. The calorimeter provides additional shielding from charged particles from the bottom of the detector.

The Pair-Conversion Tracker

The tracker consists of 16 modules arranged in a 4×4 array. Each module has 18 layers, where a layer consists out of a converter material and two layers of silicon strip detectors that are oriented orthogonal to each other. Tungsten is used as conversion layer. Due to the high density of tungsten, γ-rays have a high probability to interact with the tungsten and produce an e^+e^- pair that in the following traverses the rest of the tracker with a small opening angle between them. The silicon strip detectors are able to measure the imprint of charged particles in x- and y-direction in every layer with high accuracy. The tracking allows to reconstruct the vertex of the pair-production from which the original incidence direction of the γ-ray can be deduced.

The Calorimeter

The electron-positron pair will eventually reach the end of the tracker and enter the calorimeter. It has a total vertical depth of 8.6 radiation lengths. It consists of 96 CsI(TI) optically isolated crystals that are arranged in 8 layers with 12 crystals per layer. In addition to the physical location of the crystals, the asymmetry of the light yield at both ends of the crystal improves the spatial imaging of the shower. The total energy of the primary γ-ray can be deduced from the amount of energy collected in the calorimeter. As high-energy events will not be fully contained in the calorimeter, leakage corrections need to be applied. The calorimeter image of the showers is another useful tool to distinguish between background hadrons and γ-rays.

Performance of the LAT

Fermi-LAT has an apparent field of view of roughly 20 % of the sky at all times. Due to the rocking-angle of $\pm\,35$ deg with which the satellite is flying in low Earth orbit, a smooth coverage of the entire sky is achieved every 3 hours (or 2 orbits). The energy range covered by the LAT spans from roughly 30 MeV to about 300 GeV where the form factor results in very small photon statistics.

The energy resolution ranges from 20 % at 100 MeV to roughly 6 % at 10 GeV, limited by multiple-scattering. The angular resolution improves with the energy of the photon, starting from 10 deg at 100 MeV and improving to 0.1 deg at 100 GeV. The point-source sensitivity of Fermi-LAT depends on the location in the sky due to the large-scale diffuse emission following the structure of our galaxy. With 10 years of observations, Fermi-LAT is able to detect a source with a flux as low as $5 \times 10^{-12}\,\mathrm{erg\,cm^{-2}\,s^{-1}}$ at 1 GeV if the source is located in the galactic center. The sensitivity improves to $6 \times 10^{-13}\,\mathrm{erg\,cm^{-2}\,s^{-1}}$ if the source would be located far away from the galactic disc. The differential flux sensitivity for the LAT is shown in Fig A.2 of the appendix.

The Gamma-ray burst Monitor(GBM)

The Gamma-ray burst Monitor is another detector onboard the Fermi satellite. It comprises twelve thallium activated sodium iodide scintillation (NaI(TI)) detectors and two bismuth

germanate (BGO) scintillation detectors. The NaI(TI) detectors cover the lower part of the energy-range of GBM (8 keV - 1 MeV) and provide a direction estimate from the relative count rates measured in each detector due to their arrangement with respect to each other. The BGO detectors are sensitive in the 150 keV to 40 MeV energy range, overlapping with the NaI(TI) detectors energy range as well as with the LAT's. The statistical positional accuracy reached by the GBM ranges from 1 deg to a few tens of deg. Based on a comparison with known localisations of bursts, the systematic uncertainty of the localisation was estimated to lie between 2.2 deg and 7.6 deg (68 % containment), depending on the strength of the burst [12].

Bursts detected by the GBM allow the spacecraft to slew in order to center the LAT field of view in the direction of the burst immediately. The hope is to increase the sample of GRBs that show γ-ray emission in the GeV energy range. GBM detects around 250 bursts each year.

1.2 Ground based γ-Ray Astronomy

Victor Hess's detection of cosmic rays [1] contained vital findings for the development of ground based γ-ray experiments. His measurements revealed particle cascades in our atmosphere induced by high-energy cosmic rays. Particles in these cascades are traveling at relativistic speed, giving rise to Cherenkov light emission. Per cascade one faint Cherenkov flash is emitted. The connection between particle showers induced by cosmic rays and such Cherenkov flashes were first drawn by Galbraith and Jelley in 1953 and builds the foundation of the Imaging Air Cherenkov Telescope (IACT) technique.

Starting from the findings by Galbraith and Jelley, several prototype experiments were launched. They aimed at the detection of γ-ray induced air-showers. While all these prototypes were able to measure the Cherenkov light pulses, it was not until 1985 that a discrimination between the rare γ-ray induced air-showers and the much more abundant cosmic-ray induced air-showers was achieved [14]. A major milestone was reached in 1989, roughly 36 years after the prove of principle from Galbraith and Jelley: At the Whipple Observatory on Mount Hopkins in southern Arizona, a reflector with a 10 m diameter and a camera consisting of 37 photomultipliers was used to observe the Crab nebula [15]. This marked the first ground based detection of a γ-ray source.

From that point on, the development of the field evolved rapidly. In order to further discriminate between background and γ-rays a major improvement in the measurement of γ-ray directions was achieved by employing multiple telescopes in stereoscopic mode with HEGRA at the Roque de los Muchachos Observatory on La Palma [16]. Whipple and HEGRA combined were able to identify 10 γ-ray sources, including the first Active Galactic Nucleus (AGN) and a Supernova Remnant (SNR).

The third generation experiments, namely VERITAS [17], MAGIC [18], H.E.S.S. [19] and Cangaroo [20], brought the actual breakthrough of the field. These new experiments detected 180 individual γ-ray sources. This success was only possible due to a larger general interest in the field initiated by the Whipple and HEGRA discoveries and the subsequent larger investment in the instruments and the accompanied growth of knowledge of air shower physics. Additionally, the development of more sophisticated reconstruction, discrimination and simulation procedures (enabled by the rapid increase in computational power) played a major part. Over the years a jump in sensitivity of roughly a factor 1000 with respect to the

state of Whipple when it first discovered the Crab nebula was achieved. The energy range of this modern generation of experiments extends from roughly 30 GeV up to 100 TeV.

Due to this success, the next generation of imaging Cherenkov telescopes, the Cherenkov Telescope Array (CTA) [21], is under construction. The important step for CTA is not only another improvement in sensitivity by a factor of roughly 10, but also the fact that it will be an open observatory in contrast to the previous generations which truly were *experiments* in the sense of the word.

In the past, every newly detected gamma-ray source in TeV γ-rays was a discovery worth a publication. Today's key efforts are:

- **Deep observations towards well known and important targets for precise measurements:** Notable targets are the Crab nebula and pulsar and the supernova remnant HESS J1713. These are objects which are well measured in many wavelengths. The addition of accurate γ-ray data enables detailed discussions of the astrophysical conditions in these sources. One such source which will be discussed in this thesis is the starburst galaxy NGC 253 (Chapter 2).
- **Surveys of large sky regions** Here the scan of the galactic plane performed by H.E.S.S. [22] and the scan of the Cygnus Region by VERITAS [23] should be mentioned. Whole populations of sources can be identified as well as diffuse components due to cosmic-ray interactions in the milky way [24].
- **Performing population studies:** Large γ-ray source classes such as Pulsar Wind Nebulae (PWNe) or SNRs can further be investigated by analysing constraints from non-detection of γ-ray observations. General source properties can be deduced or constrained. Good examples of such studies are presented in [25] and [26].
- **Transients:** While the first ever detected γ-ray source was a GRB, the exploration of the time-domain is not as developed as other branches of ground based γ-ray astronomy. A few transient sources are known (e.g. flaring pulsars or magnetars). The main results are mostly brought by space based instruments at lower energies. Ground based detections would mark a breakthrough, due to the much larger effective area, which directly translates into γ-ray statistics which is generally sparse due to the short duration of the phenomena.
- **Exploring synergies of γ-rays with other messengers:** Both Neutrino- and Gravitational Wave Astronomy did just mark their break-through. There are many postulated synergies between γ-rays and these new astrophysical messengers. The full exploration is just beginning. This and the previously realm are regarded as exploratory fields.

The Imaging Air Cherenkov Telescope method

The Imaging Air Cherenkov Telescope (IACT) method differs substantially from traditional astronomy, as it does not collect the electromagnetic radiation directly. γ-rays in the GeV - TeV energy range do not reach the ground as they interact with atoms in the atmosphere at about 30 km above sea level. The only way to deduce information about these γ-rays is by analysing the interaction products. This includes identifying if the incident particle was a γ-ray in the first place. Fig 1.2 shows an illustration of an IACT: particles in the air shower cascades emit Cherenkov light which is collected by the telescopes mirror and focused onto

the camera, which is located in the focal plane of the mirror. The key components of this method are the air shower and Cherenkov light which will be discussed in the following. Based on this description common techniques for the reconstruction of γ-ray properties with IACTs will be introduced.

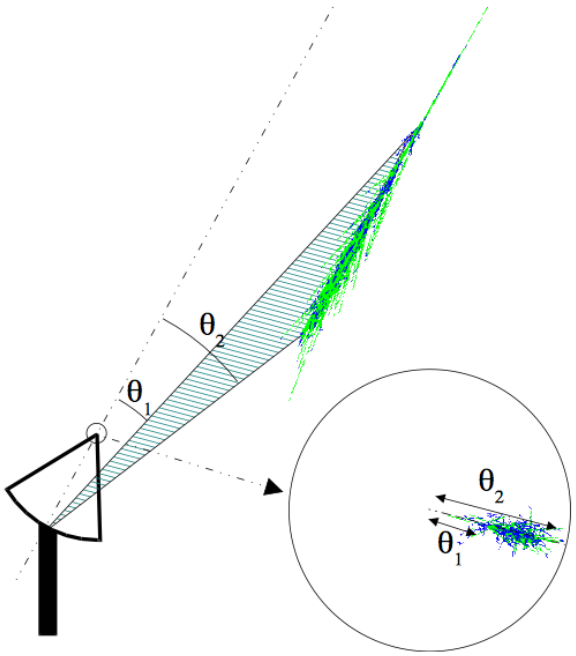

Figure 1.2: Sketch of a particle cascade seen by an IACT. The two angles $\Theta_{1,2}$ illustrate the direction of the particle shower development in the focal plane of the telescope. This figure was taken from [27].

Air Showers

For high-energy particles reaching Earth, the atmosphere effectively acts as a calorimeter with a thickness of about $27\,X_0$, where $X_0 = 37\,\mathrm{g/cm^2}$ is the radiation length in air. Depending on the species of the incident particle, the development of the air shower varies. Electrons and γ-rays will produce electromagnetic cascades driven by (a) Bremsstrahlung of $e^{\pm}$ in the Coulomb field of the atmosphere's atoms and (b) pair production of high-energy γ-rays in the Coulomb field of the atmosphere's atoms. The energy of the incident γ-ray (or electron) is gradually distributed over more and more particles. Ionisation leads to the particle cascade dying out as the energy per particle is further reduced.

High-energy hadrons (protons or heavier nuclei) are mostly scattering inelastically on the parton-parton level with the atmosphere's atoms. During these scatterings a variety of particles are produced. Among these particles are K- and π-mesons which decay further into muons, electrons/positrons and neutrinos. The parton in the incident hadron can carry a fraction of the momentum lateral to the hadrons direction. This transverse momentum translates into showers which are on average broader and more irregular than electromagnetic cascades. As pions are efficiently produced in hadronic interactions, fractions of an hadronic shower will be an electromagnetic cascade induced by a π^0. If this pion is produced early

on in the shower development, an efficient discrimination between a hadronic and leptonic induced cascade is impossible.

Modeling the development of air showers has been carried out since the 50's. Common toolkits are *Corsika* [28] and *Kaskade* [29], which simulate showers induced by any particle species. Examples of shower simulations are shown in Fig 1.3. Based on shower simulations, the Cherenkov telescope response can be investigated.

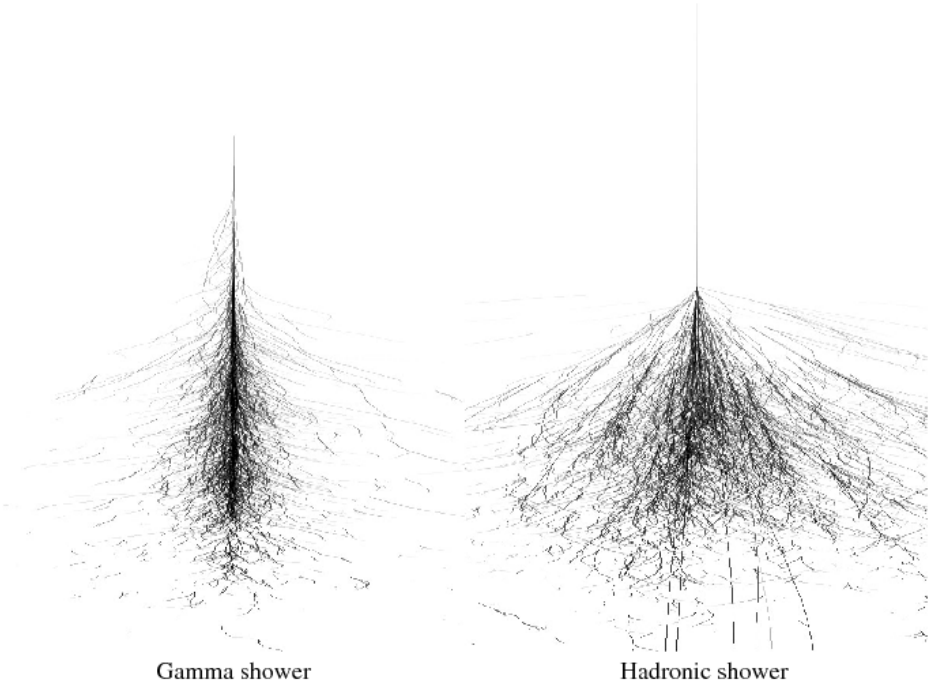

Figure 1.3: Simulated air shower cascades induced by a γ-ray (left) and a hadron (right). Compared to the hadronic shower, the γ-ray induced shower is slim and more axial symmetric. This figure was taken from [30].

Cherenkov Radiation

Relativistic particles in air shower cascades move with a velocity above the speed of light in the atmosphere, which results in the emission of Cherenkov light within a cone with an opening angle θ_c. This angle is given by $\cos(\theta_c) = 1/(\beta\, n)$ [31] where β is the velocity of the particle in a medium with refractive index n.

As the refractive index of the atmosphere increases towards the ground, the opening angle of the Cherenkov cone does so too (from 0.2° at $\sim$ 30 km to 1.5° at sea level. This effect is giving rise to a ring-like feature with a radius of approximately 100 m on the ground. The time structure of Cherenkov light pulses depends on the inclination and distance from the shower axis and is of the order of a few ns.

The energy loss per frequency $dE/d\nu$ a particle with charge q experiences per track length dx is given by [32]:

$$\frac{dE}{d\nu} = \frac{q^2}{4\,\pi}\mu(\nu)\nu\left(1 - \frac{c^2}{v^2\, n^2(\nu)}\right) dx \tag{1.1}$$

with $n(\nu)$ being the refractive index and $\mu(\nu)$ the permeability of the medium. As the energy loss does not depend on the particle species, all particles in an air shower will emit Cherenkov light. The linear dependence on ν of the energy loss indicates, that the Cherenkov radiation intensity is higher at shorter wavelengths. Since ultraviolet light is strongly attenuated in the atmosphere, instruments are optimising their performance for wavelengths of about 350 nm.

The Cherenkov light yield per path length along the atmosphere does not depend on the altitude. The integral Cherenkov yield over the shower age turns out to be approximately proportional to the primary energy of the incident particle. This important aspect allows for the calorimetric estimate of the incident particles energy, even in an inhomogeneous medium as the atmosphere.

IACTs see showers when they sit inside the Cherenkov light ring. The Cherenkov light emitted along the development of the shower is spatially resolved, which results in an elliptical image in the camera frame. This is illustrated in Fig 1.2. The technological challenge lies in a fast readout of the telescopes' cameras in order to separate the faint Cherenkov light from stray starlight or light pollution in the night sky. The cameras are required to be sensitive to single photons in order to be able to see the faint Cherenkov flash. Large mirror areas are required to collect enough Cherenkov light in order to have a measurable signal above the night sky background, even under astronomical darkness conditions. The collected light is then reflected to the camera which typically feature photomultiplier tubes to enhance the signal.

Shower reconstruction with IACTs

As mentioned above, the Cherenkov light is the only trace of particles hitting the Earth's atmosphere that is accessible for Cherenkov telescopes. The following three central parameters of the incident particle need to be reconstructed from the shower images:

- direction in the sky from which the particle originated,
- energy of the particle,
- particle species (discriminating γ-rays from other particles)

In the Whipple and HEGRA era, the reconstruction was essentially a reduction of the full camera image to the parameters of a two dimensional ellipse, the so-called *Hillas parameters* [14]. These parameters are the centre of gravity, length L and width w, *size* (total charge of the image), nominal distance d between the camera centre and the image centre of gravity, azimuthal angle of the image axis ϕ and the orientation of the shower α as depicted in Fig 1.4.

The parameters L, w and *size* are degenerate with respect to the impact distance of the shower with respect to the telescopes. The impact distance can be reconstructed geometrically from the shower images in the camera frame. So-called *scaled* length and width parameters are constructed to eliminate the degeneracy between the parameters and the initial particles energy and shower impact distance. These are based on the expected width and length of a shower ellipse as a function of the measured charge and impact distance. This allows for the discrimination between hadronic and electromagnetic showers, since the latter are systematically narrower than hadronic ones (see Fig 1.3). Hadronic showers can produce neutral pions in one of the first interactions. π^0 mesons decay into two γ-rays which

leads to an electromagnetic cascade. Such showers are largely indistinguishable from γ-ray induced air showers.

The direction reconstruction of the incident particle is not trivial either. The point of origin of a γ-ray lies on the major axis of the shower ellipse, but is degenerate over the whole axis. The *azwidth method* [33] tests the compatibility of the shower image to be a γ-ray with an assumed direction in the camera frame. By testing all possible directions, a best fit direction can be found. With better resolved images, due to an increased number of pixels in the cameras, an estimate of the position along the image axis was possible: The asymmetry of the ellipse along the major axis in combination with the estimated distance, projected on the ground, between the telescope and the shower was exploited [34].

The real break through in direction reconstruction was the stereoscopic approach. Observations of the same shower with multiple telescopes from different sides breaks the degeneracy along the major axis of the ellipse. If all images from a shower are overlaid, the direction of the incident particle is obtained at the intersection of the length axes of the images. This has already been advocated by Hillas [14] in 1985 and has been fully exploited with the HEGRA array [35].

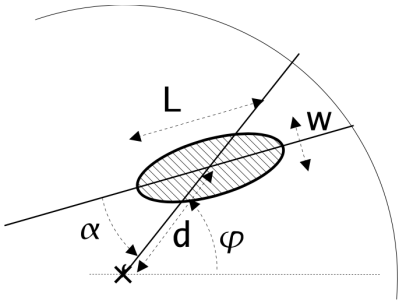

Figure 1.4: Definition of the hillas parameters in the frame of the Cherenkov telescope camera. This figure taken from [27].

1.3 H.E.S.S. – The High Energy Stereoscopic System

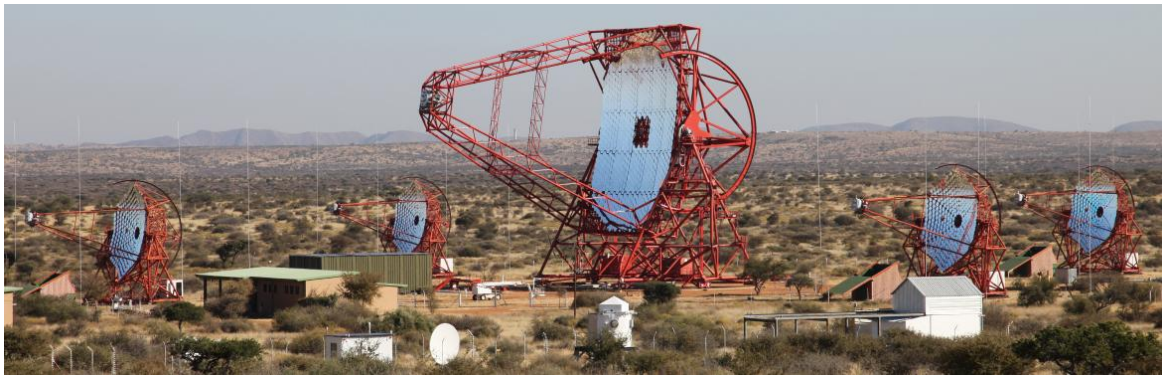

Figure 1.5: The five H.E.S.S. Cherenkov telescopes in the Khomas Highland in Namibia.

The High Energy Stereoscopic System (H.E.S.S.) is an array of five IACTs located in the Khomas highland in Namibia. The array is depicted in Fig 1.5. The area around the Gamsberg is known for its good astronomical seeing conditions [36]. Constructions of the first telescope started in 2002 for the first phase of H.E.S.S. operations. The array, consisting of four 13 m flat-to-flat diameter telescopes called CT1-4, successfully started operations in 2004.

The fifth telescope (CT5), which was added to the array in 2012, is with a diameter of 28 m substantially larger than CT1-4. This results in a significantly lower energy-threshold of $\mathcal{O}(20\,\mathrm{GeV})$ compared to a threshold of $\mathcal{O}(100\,\mathrm{GeV})$ of the previous array of four telescopes. It was placed into the center of the H.E.S.S. array. The layout of H.E.S.S. in Phase I was chosen such, that a large fraction of typical Cherenov light pools is covered by at least two telescopes in order to allow for stereoscopic reconstruction. With CT5, placed in the centre of the array, the best overlap between the two kinds of telescopes is achieved.

Besides the basic information on the telescopes given in Table 1.1, specific aspects of the instruments which are of importance for this thesis will be highlighted in the following. Further, the data taking and calibration will be discussed. Finally, the analysis methodology in H.E.S.S. will be described.

Table 1.1: Collection of parameters for both H.E.S.S. Phase I and II telescopes and cameras.

Parameter	H.E.S.S. I (CT1-4)	H.E.S.S. II (CT5)
Operation start	2004 (4 telescopes)	2012
Number of Telescopes	4	1
Weight per telescope	60 t	580 t
Telescope arrangement	square with side lengths of 120 m	in the centre of the square
Slewing speed	100° min^{-1}	$200^\circ_{\mathrm{Azimuth}}\,100^\circ_{\mathrm{Elevation}}$ min^{-1}
Single telescope Mirror	13 m diameter, Davis Cotton [37]	$24.3\,\mathrm{m} \times 32.6\,\mathrm{m}$ parabolic
Total Mirror area	$107\,\mathrm{m}^2$	$614\,\mathrm{m}^2$
Mirror tessellation	380 circular, 30 cm radius	875 hexagonal, 90 cm radius
Mirror reflectivity	60 % - 80 %	similar to H.E.S.S. I
Focal length	15 m	36 m
Camera Pixels	960 PMTs with 0.16° FoV	2048 PMTs with 0.067° FoV
Total Field of View	5°, 11 % shadowing	3.2°, 7.5 % shadowing
Average Pointing uncert.	$6''_{\mathrm{axis}}$, $20''_{\mathrm{observations}}$ [38]	similar to H.E.S.S. I

Instrumental aspects of special relevance for this work

In the two physics cases addressed in this thesis, different instrumental challenges are faced:

The starburst galaxy NGC 253 is the faintest γ-ray source detected at TeV energies. It was observed with H.E.S.S. I telescopes only. Important factors for the detection and spectral analysis are the following:

Due to the observations being carried out largely at very low zenith angles, the steel structure holding the camera experienced more stress than usually. Deformations of the holding structure directly correspond to the camera moving in the focal plane of the telescope. Also the mirror holding structure can be subject to slight deformations. In order to keep the

nominal performance, a careful correction of the telescopes' pointing position is necessary. This correction is calculated from a mechanical model. Based on the model, corrections to the reconstructed direction of γ-rays can be applied.

With the observations being taken almost in zenith, the tracking of the source position is going much faster in azimuth than usually. In order to track the source position for the nominal run duration of 28 minutes, the allowed range of motion in azimuth is vital. The H.E.S.S. I telescopes allow for a motion range of 540 degree. Before a new observation run is started, the telescope slews into a starting position such that the target can be tracked for the entire 28 minutes.

The observations of transient γ-ray sources target mostly lower energies. Therefore the H.E.S.S. II telescope is the central instrument for these studies. As transients are expected to fade within a short amount of time, the repointing speed is of utmost importance. The maximum velocity of CT5 is $1.67^\circ\,\mathrm{s}^{-1}$. Additionally, the telescope is allowed to slew overhead in the so-called 'reverse' mode. This allows to slew to 90 % of randomly chosen potential target locations within less than 60 seconds [39].

For the observation of transients, a special *ToOObservation* run type was developed. It allows for the start of observations as soon as the new target enters the field of view of CT5, regardless of the state of CT1-4. CT1-4 are able to joint the observation later. In case they experience failures, the observations of CT5 are not interrupted. Apart from the time for the transition needed by hardware, the remaining software overhead is on the level of one second [40].

The energy-threshold of IACTs is largely defined by their mirror area. With its $614\,\mathrm{m}^2$ surface area, CT5 is the IACT with the largest light-collection area to date. Other aspects leading to reduced light collection are: the degrading reflectivity of mirrors, gaps between the Winston cone light-guides sitting on top of the camera pixels, the quantum efficiency of the photomultiplier tubes (PMT). Non-instrumental constraints are also important to note. Most importantly, the zenith-angle Θ_{zen} of the observations scales the energy-threshold as $\cos(\Theta_{\mathrm{zen}})^3$. Increased night sky background light, as found for instance in the η-Carinae region can degrade the energy-threshold further.

Data taking and calibration

Data taking with H.E.S.S. is performed under astronomical darkness. The steering of the telescopes is handled by the central data acquisition system [41]. The read out of events during observations depends on different levels of triggers. First, an event has to trigger an individual telescope. For this, two thresholds exist: i) the pixel-threshold which has to be passed by each pixel contributing in the triggering event. ii) the sector-threshold which requires a set number of triggered pixels in an area of four drawers (units of 4×4 pixels). The layout of the sectors are overlapping for a homogeneous trigger response. This cluster trigger algorithm reduces the single pixel trigger rate of $\sim 100\,\mathrm{MHz}$ to $\sim 3.5\,\mathrm{kHz}$ in the case of CT5. As an event reaches the trigger requirements, all PMT waveforms are integrated over 16 ns around the peak and read out from the ring buffer storage. The integrated signal is obtained in two different gain channels, namely the *High-* and *Low-* gain channels. The Central Trigger is responsible for stereoscopic triggers. It requires at least two telescopes to recognise a triggered event within 80 ns. The small telescopes only contribute to the stereoscopic triggered data, while CT5 data is also stored for monoscopic triggers.

Before the previously introduced analysis techniques can be applied to the recorded events, several calibrations need to be applied. For all details on the different procedures, the reader is referred to [27, 42]. Here, a brief summary of the procedures will be given:

- The analog to digital converted (ADC) signal of the PMTs has to be converted to units of photo electrons. For this, a special procedure is in place in which the cameras are flashed by a light source capable of illuminating the camera with single photons. This is being performed under astronomical darkness while the telescopes are parked in, in order to suppress contamination from the night sky background. The response distribution yields both the pedestal and the single photo-electron peak as a function of ADC counts. The peak position is the conversion factor from ADC counts to photo electrons. This can only be performed in the high-gain channel, as the gain of the low-gain channels amplification does not suffice for a clear separation of the single photo-electron peak and the pedestal.

- In order to translate the measured conversion ratio between ADC counts and photo-electrons to the low-gain channel, the so-called High-Low ratio is calculated from normal observation data. It can be obtained from the slope between the ADC count distribution of both channels.

- The response of all pixels of one camera is homogenised with the so-called flat-fielding procedure. A highly homogeneous light source in the centre of the mirror plane illuminates the full camera. The resulting response distribution (in units of photo electrons) per pixel is then corrected towards the mean of all pixels.

- The response is furthermore homogenised between telescopes using muon events. These events are easily identified by their Cherenkov light ring (or a segment of it) which is captured in one camera. The rate of Cherenkov rings from muons seen by each telescope allows to correct each telescopes response to a mean response. The muon flux serves as a common Cherenkov light source.

All calibration procedures are implemented in two independent chains for cross-check purposes.

Data Analysis

Model Analysis

Modern reconstruction techniques are heavily reliant on the accurate simulation of air shower cascades. One of the most sophisticated analysis frameworks for IACTs is the *model-analysis* [43]. This is a state-of-the-art reconstruction technique available for H.E.S.S. data and was applied throughout this work. This method is no longer based on a parametrisation of the Cherenkov light image in the camera. It compares the exact observed Cherenkov light yield with the one predicted by a semi-analytical model. These models describe the number of particles as a function of the longitudinal, lateral and angular axis of the shower. Many such models are generated for different energies of the incident γ-ray with the help of simulations using the *Kaskade* toolkit. The emitted Cherenkov radiation can be calculated from the number of particles in the shower. This Cherenkov radiation is then fed into the detector simulation which yields camera images which can be compared to the observed images.

The measured and predicted images are compared pixel by pixel. The response per pixel is treated as a Gaussian with width σ which is given by:

$$\sigma = \sqrt{\sigma_p + n\sigma_\gamma + \sigma_f} \tag{1.2}$$

The individual contributions are (a) electronic noise and stray starlight which is measured in the width of the pedestal σ_p, (b) the number of photo electrons n and the width of the single photoelectron peak σ_γ and (c) the intrinsic fluctuations in the development of air showers σ_f.

Based on this, a probability density function (PDF) is built that describes the probability to observe a certain signal value for a given signal expectation. This PDF is given by the convolution of a Poisson distributed number of photo electrons and the Gaussian response of the pixel. The compatibility between the observed image and the predicted one is evaluated using a maximum likelihood method [44] [45]. The likelihood includes all pixels and is maximised by changing the parameters of the incident particle.

The best parameters that are found can be evaluated in order to suppress badly reconstructed events. Cuts are commonly applied on the total image amplitude (in units of photo electrons), the uncertainty of the reconstructed direction, the likelihood of the event to originate from starlight induced noise and more. Another important parameter in the model analysis is the goodness of the fit. Showers which were not induced by γ-rays yield systematically worse fits, as the templates are generated for γ-rays only. All cuts combined allow for an efficient γ-hadron separation. The model analysis improves the signal to background ratio by a factor of more than 6 compared to the classic Hillas analysis approach [43].

Background Subtraction

Air showers induced by protons are much more abundant than γ-ray showers. Hadronic showers which produce a neutral pion in the first generations of the shower are largely indistinguishable from γ-ray induced showers. An additional contribution to this irreducible background originates from air showers induced by cosmic-ray electrons. Such irreducible background contributions in the γ-ray candidates N_{on}, selected from in the target region, need to be subtracted. Protons and electrons are known to arrive at Earth approximately isotropically, while γ-rays point back to their sources. This allows to estimate the contamination outside of the target region, in control regions called *off-regions*. Several approaches are commonly employed.

A commonly used background estimation method is the *MultipleOff* method [46]. In this method many off-regions of the size of the target region are combined. The number of γ-ray candidates in all off-regions combined is N_{off}. The usage of many different regions allows to average out potential fluctuations. Due to multiple regions being used, N_{off} has to be scaled to the exposure in the target region which is given by the parameter:

$$\alpha = \frac{\int_{\text{on}} A^\gamma_{\text{on}}(x, y, \theta_z, t)\, dx\, dy\, d\theta_z dt}{\int_{\text{off}} A^\gamma_{\text{off}}(x, y, \theta_z, t)\, dx\, dy\, d\theta_z dt} \tag{1.3}$$

where A^γ is the γ-ray acceptance as a function of the location in the field of view (x, y), the zenith-angle θ_z and exposure time t. The number of excess γ-ray events above the background in the target region is finally given by $N_{\text{excess}} = N_{\text{on}} - \alpha \times N_{\text{off}}$.

Another commonly employed technique is the so called *ring*-background method [46]. In this approach, the background with respect to a specific target region is chosen to be a ring

around the position. In this case, α is approximately given by the ratio of the angular size of the ring in comparison to the target region. Additional acceptance corrections are however needed, since the ring covers different offsets from the observation position.

Finally, the *reflected-region* background model [46] should be noted. It applies to observations carried out with an offset to the target position, such as the commonly employed *wobble-mode* observations [47] in which the pointing position alternates around the target position with a fixed offset. For the background model, n_{off} regions are defined in a ring around the pointing position, one of them being the target position. With this setup there is no need for an offset correction and $\alpha \approx 1/n_{\text{off}}$ which can differ strongly from run to run.

Both the ring and the reflected-region background models can be applied to any position in the field of view and are thus useful for the creation of significance maps. The MultipleOff method is employed for the computation of photon statistics for spectral fits. Examples for both cases are depicted in Fig 1.6.

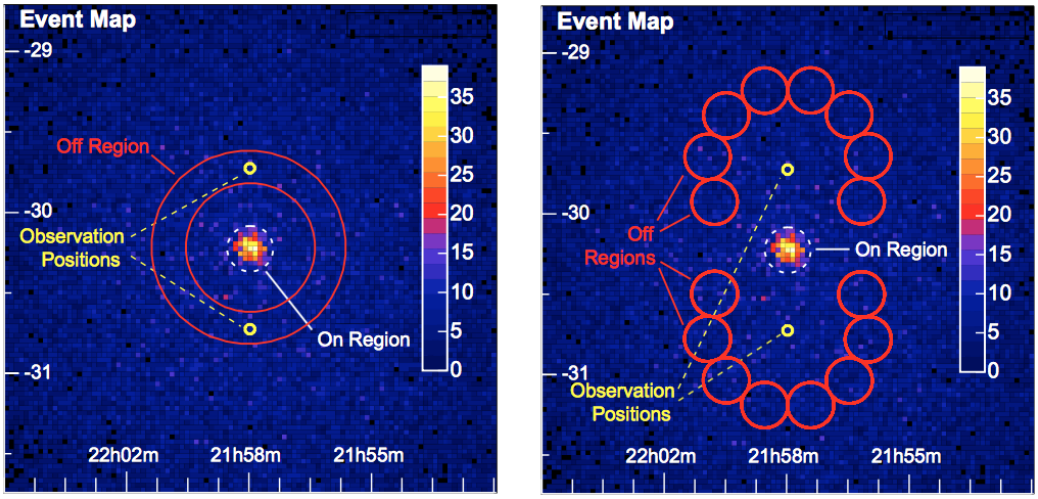

Figure 1.6: Examples for on and off regions for the ring (left) and the reflected-region (right) background models. This examples are based on observations of the active galaxy PKS2155-304 [48]. From [46]

Analysis Procedures

The actual analysis of the data performed in this work follows the previously described model analysis framework. It was adapted for monoscopic applications as reported in [49].

In this work two different kind of target classes are being probed. The starburst galaxy NGC 253, which was observed over the course of several years, is assumed to exhibit a constant γ-ray flux as a function of time. In contrast, the second class of targets are transients: astrophysical phenomena which occur once and fade away quickly afterwards.

Data obtained during the follow-up of transients can not be obtained through further observation of the sky location. Therefore special care has to be taken during the data analysis, starting already at the level of validating the calibration and hardware status during the observations. Data with insufficient quality are often ignored during the analysis of normal steady sources in order to ensure a homogeneous response of the analysis and precise measurements. Such a practice is not possible in the case of transients due to the

small amount and the irreproducibility of the data. The impact of typical problems need to be understood in order to determine if the data can safely be analysed. In rare cases a detailed reprocessing of the data is possible to recover otherwise unusable data. In the following, the procedures for transient analyses, which were established as part of this thesis, will be described. The goals are:

1. Understand potential issues that can be encountered during the analysis of transient data.
2. Understand the impact of such issues on the final results.
3. Evaluate if the analysis can be carried out safely.
4. Reduce the amount of trials.
5. Enable everyone to carry out transient analyses.

A brief overview of the tests and considerations for analyses of transients will be given in the following. These tests and practices were collected and defined during the analysis of several transients and are still evolving in order to cover more and more possible issues. While it was first aimed to present a fixed analysis procedure for GRBs it now finds common usage for any kind of transient analyses.

Familiarisation with the Event and the H.E.S.S. Follow-up Observations Before starting to investigate the data, it is advised to collect all available information about the astrophysical event. This way the target position and its localisation precision and time structure can be accounted for during the analysis. The shift crew, which is operating the telescopes, provides information on complications, weather conditions or hardware failures and other issues or warnings for each night of observations. This information helps to judge the reconstruction and calibration quality and can already point towards potential issues. Ideally the information gathered is sufficient to come up with a step-by-step analysis plan that outlines how observations are merged and which information is most important to derive in order to maximise the science return. Also detected *Fermi*-LAT sources or bright stars in the field of view should be investigated in order to exclude regions of the sky which might exhibit γ-ray emission unrelated to the transient.

Calibration and Reconstruction Validation Judging the validity of the calibration and reconstruction is not an easy task and is done by manually investigating control distributions for each individual dataset. Three main observables were found to be especially helpful in the assessment of the data quality:

Pedestal distribution: The pedestal is a measurement of the electronic noise level and is monitored for each pixel of the camera. The mean and RMS (as well as their temporal behaviour over the course of the observations) of the noise is a useful handle to judge if all pixels were operating nominally. Typical issues that can be detected with these observables are noisy or switched off pixels or entire drawers that were malfunctioning. This observable yields a first indication of the homogeneity of the expected response for each telescope.

Pixel participation fraction: This is the fraction of reconstructed events in which each pixel participated with respect to all reconstructed events. This observable also tracks the

homogeneity of each camera's participation in the event reconstruction. Noisy parts of the camera found due to their increased noise level can further be monitored in order to check if the issues found in the pedestal distributions propagate into the event reconstruction.

Centre of gravity distribution: The distribution of the centre of gravity locations can be mapped in the camera frame for all reconstructed shower images. In addition to the increased rate of participation in the event reconstruction, the centre of gravity map can reveal directional inhomogeneities in the event reconstruction. A homogeneous centre of gravity map ensures a homogeneous response to both γ-rays and hadronic showers.

All observables are collected for each observation run and each telescope. In the case that severe holes or spikes in the centre of gravity map are found, fake signals cannot be ruled out. The calibration and reconstruction can be repeated while artificially switching off problematic parts of the camera in an effort to achieve a more homogeneous response.

The quality of the calibration and reconstruction is judged by the analyser in tight cooperation with analysis and reconstruction experts. The high-level analysis is being performed only when the quality of the data was found to be sufficient.

Final Analysis of the Data The high-level analysis of the data should closely follow the plan that was derived based on multi-wavelength information that was collected before. The approved software versions and cut configurations are mandatory to be used. Typical products of the high level analysis are differential and integral upper limits, upper limit sky maps, light curves and further tests for temporal variation in the data. The settings which are recommended for the usage of the analysis tools were found to keep systematic uncertainties under control. Such settings are for instance the definition of the energy-threshold or the minimal number of background events.

Often the *loose-cut* configurations of the analysis chains are employed, which were optimised for both stable results and a low energy-threshold. Sky maps are typically generated using the ring background method while spectral results are derived from the photon statistics obtained with the MultipleOff background subtraction method (see section 1.3). For upper limits, at least 10 counts in the off region are required. A safe choice for the energy-threshold is the energy at which the effective area has dropped to 15 % of its maximum value [50].

1.4 Sensitivities of γ-Ray Experiments

Space based and ground based instruments are not only quite different in their techniques, they also perform very differently. While space based instruments are able to measure γ-rays directly, the form factor of space based instruments presents a natural limitation at higher energies. With the atmosphere as detector volume, ground based instruments like H.E.S.S. are able to push to higher energies. At lower energies they suffer from higher background rates and fainter, thus harder to reconstruct, Cherenkov light flashes. Additionally, the duty cycle for Cherenkov telescopes is with ~ 10 % rather small compared to the 99 % duty cycle of satellite experiments. Both techniques provide complementary data. This allows to exploit space based experiments as survey instruments which trigger ground based observations.

Sensitivity to Sources with Constant Fluxes

The sensitivity of Cherenkov telescopes depends on many different aspects, ranging from the array configuration to observation conditions (e.g. the zenith-angle of the observation), the assumed source spectrum and the analysis method and configuration. Therefore, the differential energy flux sensitivity is shown for several analysis chains and observation conditions for H.E.S.S. II Mono and Stereo analyses in Fig 1.7. In both cases, the assumed spectrum is the Crab spectrum as measured by H.E.S.S. [51]. The sensitivities are calculated for 50 hours of observations. From the sensitivity curves it is apparent, that the monoscopic mode provides a significantly lower energy-threshold at the cost of less overall sensitivity in the core energy range at around 1 TeV.

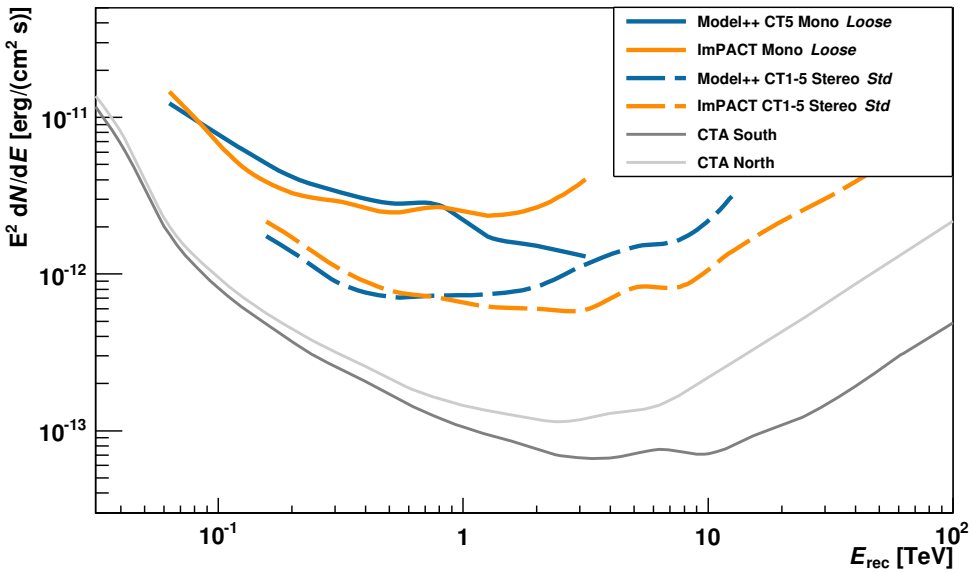

Figure 1.7: Differential sensitivities from different analysis chains and array configurations for observations at $\sim 20^\circ$ zenith. The sensitivities are calculated for 50 h observations of a source with an assumed flux according to the Crab nebula as measured by H.E.S.S. [51]. The differential sensitivities for monoscopic observations with CT5 are shown as well as for stereoscopic observation of CT5 plus one of the smaller telescopes CT1-4. In stereo mode, an overall improved sensitivity in the core energy range is achieved. Mono mode provides a significantly reduced energy-threshold.

Sensitivity to Transient Sources

A second important sensitivity is the flux sensitivity as a function of observation time at fixed energies. This is shown in Fig 1.8 for both Fermi-LAT and H.E.S.S. II at energies of 80 and 200 GeV. For short time-scale events one can see that H.E.S.S. II provides a factor of $\sim 10^5$ more sensitivity than Fermi-LAT at the same energy. It is apparent that this advantage is present up to observation times of more than 3 years, after which the LAT sensitivity supersedes the one from H.E.S.S. II. Such deep exposures have, and probably

will, never been collected for an individual source and are far beyond the expected time structures of transients this thesis will discuss. In fact one can see that the sensitivity is not improving significantly after $\sim$ 30 h of mono observations. Targets with fluxes evolving on such timescales should therefore be observed in stereoscopic mode to make use of the overall jump in sensitivity discussed above. The *Fermi*-LAT sensitivity in their core energy range (around 1 GeV) is naturally better compared to the one presented here at 75 GeV. This gradual improvement is indicated by the *Fermi*-LAT sensitivity curve for 40 GeV. Looking at the differential sensitivity of *Fermi*-LAT (shown in Fig A.2 of the Appendix), it is evident, that IACTs like H.E.S.S. II still outperform *Fermi*-LAT on short timescales by several orders of magnitude.

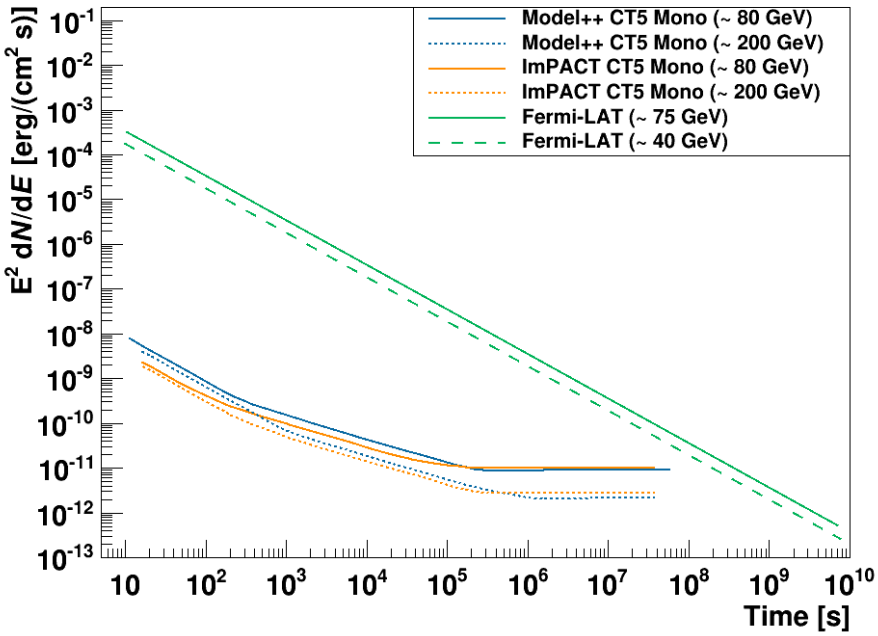

Figure 1.8: Integral energy flux sensitivity as a function of observation time for H.E.S.S. CT5 mono observations in comparison to *Fermi*-LAT. At short exposures in the order of 100 s, the sensitivity of CT5 supersedes the one from *Fermi*-LAT by several orders of magnitude. After $\sim$ 30 h of observations, the sensitivity is dominated by systematics.

1.5 The Age of Multi-Messenger Astronomy

One exceptional example for physics results from the benefits of the multi-wavelength approach is the starburst galaxy NGC 253. The estimation of the starburst activity and gas content comes from infrared, radio and X-ray observations. Its γ-ray spectrum holds important information on the cosmic-ray energy density in the system. Important implications for the large population of starburst galaxies can be discussed on the basis of this single object. The results are of relevance to other messengers beyond the electromagnetic spectrum, as for instance for the origin of Ultra High Energy Cosmic Rays (UHECRs) and neutrino sources.

γ-rays are no longer the only window into the non-thermal universe. Recent breakthroughs brought the advent of two novel branches of astronomy: Gravitational Waves and Neutrinos. The latter are directly connected to γ-rays as they can originate from the same hadronic interactions and the subsequent decay of pions. Gravitational waves as they are being detected today typically originate from the merging of compact objects like neutron stars and black holes. Such mergers have long been discussed as potential progenitors of GRBs.

These new messengers promise joint exploration of astrophysical phenomena and processes beyond the electromagnetic spectrum. Strong collaboration between the infrastructures is key in order for all communities to profit from the unique views provided by the different messengers. Ideally, this collaboration extends into the shortest possible timescales in order to obtain more contemporaneous data. All infrastructures invest into the realisation of such prospects. The major part of this thesis covers the work in H.E.S.S. to make the best use of the information provided by survey infrastructures of all messengers.

With H.E.S.S. in phase II and the advent of both neutrino and gravitational wave astronomy, a growing focus of H.E.S.S. observations lies on multi-messenger targets in the time-domain. The science cases are rich both in diversity and potential rewards, while coming with non-trivial complications for the observations. The challenges for such observations will be motivated based on the GRB science case in chapter 3. The technical execution of such observations with H.E.S.S. will be described in chapter 4. Selected highlights of observations of transient multi-messenger signals with H.E.S.S. will be presented in chapter 5. Therefore a brief overview of the advent of both gravitational wave astronomy and neutrino astronomy will be given here.

The Advent of Gravitational Wave Astronomy

The newest branch of astronomy, Gravitational Wave astronomy, was born in 2015 with the detection of gravitational waves from the merger of two black holes [52] by LIGO. This opened a new view on exceptionally violent events in our universe. Gamma-Ray Bursts, the first detected γ-ray phenomena, are being discussed in the framework of mergers of neutron stars and/or black holes for over a decade. After many decades of incremental improvements of understanding of GRBs, Gravitational Waves will finally be able to reveal the progenitors of GRBs, as demonstrated by the first detected merger of two neutron stars in coincidence with a GRB [53]. As discussed in section 1.1, GRBs are the founding source class of γ-ray astronomy. Therefore, a tight collaboration between the communities is natural.

The next generation of Gravitational Wave instruments are already in planning. They bring prospects for many science cases overlapping with γ-ray astronomy, as e.g. binaries and supernovae [54].

The Advent of Neutrino Astronomy

The diffuse astrophysical neutrino flux has been discovered by IceCube in 2014. The search for sources of neutrinos is however much older. Currently the only identified non-terrestrial neutrino sources are the Sun and supernova 1987A. These neutrinos are however of much lower energies than the diffuse flux at hundreds of TeV. Many of the known γ-ray source classes are also candidate sources for the neutrino flux as both an extragalactic and galactic origin are possible scenarios.

γ-ray and ν astronomy are uniquely coupled due to the common hadronic production mechanism: The interaction of high-energy protons produce many secondary particles among which π- and K-mesons are the most common ones. Their decay naturally leads to the production of both neutrinos and γ-rays. Any source which has proven to accelerate hadrons in γ-rays is therefore expected to produce neutrinos. Due to the different energy loss mechanisms of γ-rays, both messengers potentially probe different regimes of the source. γ-γ absorption typically leads to sources being opaque in regions with high photon densities. Since no such absorption effects apply to neutrinos, they can potentially reveal physical processes at the heart of such particle accelerators.

The absence of strong energy loss processes for neutrinos presents not only a challenge for the detection techniques. It implies that any source at any distance to Earth will contribute to the overall flux. With large numbers of active galactic nuclei (AGN) and starburst galaxies distributed troughout our universe, the neutrino flux might in fact be seen as diffuse by the current experiment generation. Short time scale transients producing neutrinos at a significantly amplified strength might however still stick out. A correlated detection in γ-rays and other wavelengths of the electromagnetic spectrum as well as neutrinos is therefore a smoking gun event to finally identify neutrino sources.

Chapter 2

γ-rays from the Starburst Galaxy NGC 253

Figure 2.1: The two starburst galaxies M82 (left, Hubble Space Telescope composite of infrared and visible light) and NGC 253 (right, 2.2 m telescope at La Silla Observatory). These are two archetypical examples of starburst galaxies and the only two objects of this class known to emit γ-rays at TeV energies. The images originate from NASA and ESO.

Starburst galaxies are galaxies that are undergoing an episode of enhanced star-formation. They are interesting objects for observations in basically any wavelength and messenger. The star-formation activity is accompanied by a similarly enhanced rate of Supernova explosions. Several remnants of supernovae have been observed in our galaxy, yielding strong evidence for the acceleration of cosmic rays. A whole population of supernova remnants (SNR) is present in starburst galaxies. Collectively, these SNRs are filling their galaxies with cosmic rays, making them a prime target for γ-ray and neutrino observations.

The closest example of such a starburst galaxy is NGC 253 which is depicted in Fig 2.1 (right). With a distance of only 3.5 Mpc, detailed measurements in near infrared and X-rays allow for a quite precise picture of the astrophysical conditions in this object. The comparison of the expected γ-ray emission based on the astrophysical conditions with the measured high-energy and very-high-energy γ-ray measurements allows for an estimation of the cosmic-ray flux density and the fraction of the flux which is absorbed in the galaxy itself.

This chapter will present a re-analysis of the data H.E.S.S. acquired during the observations towards the starburst galaxy NGC 253 in the years from 2004 to 2009. Results from this data were published several years ago in [56] and [57]. NGC 253 is, together with M82 which is depicted in Fig 2.1(right), one of only two starburst galaxies that are known to emit γ-rays with energies up to TeV energies. A re-analysis of this important set of data with up-to-date software which is making use of all improvements achieved over the years has been carried out in this thesis. The measurement by H.E.S.S. has been limited by systematic uncertainties in the previous publication. This is no longer the case for the improved analysis presented here.

First, the starburst phenomenon will be introduced in section 2.1 along with astrophysical properties and questions which can be addressed with γ-ray observations . The description of the analysis of γ-ray observations from H.E.S.S. as well as Fermi-LAT towards NGC 253 will be presented in section 2.2. The resulting γ-ray spectrum and its implications for the underlying population of cosmic rays in the starburst nucleus will be discussed in section 2.3. An outlook for future γ-ray observations of NGC 253 and the starburst phenomenon will conclude this chapter.

This work is also published in [58] in a more compact form.

2.1 Starburst Galaxies and Cosmic Rays

The starburst phenomenon

Star formation is a process at the heart of astrophysics as it describes the origin of stars and planetary systems. Star formation drives structure formation and evolution from individual galaxies to clusters of galaxies. Objects or regions are classified as undergoing a starburst phase based on the SFR which is determined over the measurement of the gas-consumption time. The starburst term applies when the SFR in the system is out of equilibrium and higher than the large-scale and long-term SFR of the system. Another classification requires that the SFR can not be sustained for more than a small fraction of the Hubble time ($<$ 10 %) which implies gas consumption times of much less than one Gyr [59]. Even though galaxies with enhanced SFR are called starburst galaxies, the starburst is usually confined to localised regions in these galaxies.

The mechanisms which trigger starburst phases are not well understood. The beginning of a starburst episode is commonly characterised with gravitational disturbances and tidal disruptions. The two following observations strengthen this hypothesis:

- Diaz et al. [60] associated a high mass concentration to an arc of star formation in M83 and conclude that the starburst arc is a result of the massive object crossing through.

- More prominent is the example of the ultra luminous infrared galaxy Arp 220 where Norris [61] found evidence for two galactic nuclei in radio observations. This observation is interpreted as evidence for a recent merger of the galaxy with a companion ore a satellite galaxy.

Both gravitational disturbances are interpreted as the mechanism which brought the system out of equilibrium by applying pressure on the gas, thus leading to a period of enhanced star formation.

The Supernova - Cosmic Ray Connection in Starburst Galaxies

The consequence of a higher rate of star formation is a larger number of massive stars which undergo supernova explosions. More frequent supernova explosions yield a larger population of supernova remnants (SNR). SNR are believed to be one of the main sources of cosmic rays (CR), galaxies that undergo a starburst phase are therefore providing a promising testbed to probe the SNR–CR acceleration paradigm.

The local cosmic-ray spectrum is dominated by protons (roughly 88 %). There is strong observational evidence, that cosmic rays are in fact efficiently accelerated in the shocks of some SNRs in our galaxy. Prime examples are IC 443 and W 44 [62] in which the spectra exhibit a so called *pion bump*, the kinematic signature in γ-ray spectra produced by decaying π^0 mesons. The *pion-bump* is a smoking gun signature of proton acceleration as π mesons are efficiently produced in proton-proton (*pp*) interactions. Based on these findings, it is reasonable to assume, that SNRs accelerate protons in our galaxies as well as in distant galaxies. Hence, their CR spectrum should similarly be dominated by protons.

The most common source class detected at TeV energies in our galaxy are however pulsar wind nebulae (PWN) [22]. Their γ-ray emission is best described in the framework of leptonic energy losses like bremsstrahlung, synchrotron and inverse Compton radiation. Ohm and Hinton [63] estimated that synchrotron and bremsstrahlung yield insignificant contributions to the observed γ-ray flux in starburst environments. Inverse Compton radiation however is of relevance due to the strong far-infrared radiation fields which are present in starburst galaxies which can cool leptons very efficiently. Ohm and Hinton [63] found that the inverse Compton contribution fails however to describe the HE γ-ray emission seen from starburst galaxies by *Fermi*-LAT, but might contribute to a distinct feature at VHE γ-rays which could be probed with the next generation of IACTs. In the broad picture, the assumptions that hadrons are dominantly contributing to γ-ray emission from starburst galaxies is reasonable and broadly consistent with theoretical models and observations.

Detailed knowledge of the CR energy density in the starburst nucleus is of relevance for many other disciplines in astrophysics: CRs are an efficient source of ionisation and are therefore an important factor for chemical reactions in molecular clouds [64]. Additionally, Papadopoulos and Thi [65] pointed out that regions of very high CR densities might exhibit a lack of low-mass star formation due to CR heating.

To address such questions, a measure of the energy density in CRs in the starburst region is necessary. The well understood particle collision and energy loss processes of CRs make γ-rays an excellent messenger to deduce the CR spectrum. One of the central hypothesis this work is based upon needs however to be verified: The γ-ray emission does not originate from an active black hole in the centre of the galaxy. Active galactic nuclei (AGN) are the most common source found in the γ-ray sky. The γ-ray emission seen from these objects is thought to originate from energy release of accreted matter which is transferred to particles which are ejected in relativistic outflows. Such scenarios are interesting in their own right. In such a case, the SNR-CR paradigm outlined above would be overshadowed completely. Most AGN exhibit strong variability. The long-term monitoring of the γ-ray emission of starburst galaxies can therefore be used for the search for variability which is not expected if the γ-ray emission indeed originates from the supernova remnant population in it.

Cosmic rays in starburst galaxies

Assuming that hadrons dominate the cosmic-ray spectrum in starburst galaxies, γ-ray observations can provide an estimate of the CR spectrum. Not all CRs in the starburst will interact and subsequently produce γ-rays. CRs can loose their energy trough several mechanisms which all should be considered. Addressing these mechanisms needs input from particle interaction physics as well as the astrophysical parameters of starburst galaxies.

Advection

The escape of CRs by advection is an energy independent process. In starburst galaxies, the collective mechanical power of many supernovae and stellar winds accumulate to superwinds which are able to sweep cosmic rays along with interstellar gas out of the galaxy [66]. While this process will remove a fraction of the CRs, the spectral distribution will remain unchanged. The advective loss time is given by $\tau_{\rm ad} = (H/2)/v_{\rm wind}$ [67] with wind speeds $v_{\rm wind}$ in the order of a few hundred km/s and H being the height of the starburst volume. With typical starburst galaxy parameters, this loss time is of the order of 10^5 years and therefore much shorter than the duration of the starburst phase. Hence, a significant fraction of the CRs which were accelerated over the history of the starburst episode may in fact be removed from the nucleus. Accordingly, γ-ray observations only probe CRs from the recent starburst history of such systems.

Adiabatic losses

The CRs apply pressure to the gas in the system leading to an adiabatic expansion. During adiabatic expansion, severe energy losses can occur. The energy loss can be derived from the loss of internal energy U in an expanding volume V. The loss is given by $dU = -p\,dV$ with p being the pressure of the gas applied by the CRs. Approximating the CRs as a monoatomic gas, the internal energy and pressure is given by $U = 3/2nkTV$ and $p = nkT$ where n is the number density of particles with temperature T. The mean energy per particle is given by $E = \frac{3}{2}kT$. Applying these relations leads to $dU = nV dE = -2/3\,nE dV$. With $N = nV$ being the total number of particles it follows $\frac{dE}{dt} = -\frac{2nE}{3N}\frac{dV}{dt}$, where $\frac{dV}{dt}$ is the rate of expansion of the volume which is dictated by a velocity field $\mathbf{v}$. Using a taylor expansion for small changes this equations reduces to $\frac{dE}{dt} = -2/3(\nabla\mathbf{v})E$. For relativistic particles the energy loss is modified to $\frac{dE}{dt} = -1/3(\nabla\mathbf{v})E$. The exact energy loss therefore depends on the morphology of the velocity field $\mathbf{v}$ [32].

The expansion is driven mostly perpendicular to the galactic plane with height H in starburst galaxies. Due to the winds, the velocity field should be 0 at the galactic plane and $v_{\rm wind}$ at the distance $H/2$. The velocity field can therefore be expressed as $\mathbf{v} = (0, 0, v_{\rm wind} z\frac{2}{H})$ [57]. The adiabatic energy loss in this geometry is therefore given by:

$$\left(-\frac{dE}{dt}\right) = \frac{1}{3}E\,v_{\rm wind}\frac{2}{H} \tag{2.1}$$

Integrating over energy, assuming the CRs to follow a power-law as E^{-s}, yields the energy loss time scale $\tau_{\rm adiab} = \frac{3}{2}\frac{H}{v_{\rm wind}}\frac{1}{s-1}$ or $\tau_{\rm adiab} = 3\,\tau_{\rm ad}/(s-1)$ [57]. The energy loss time scale due to adiabatic expansion is therefore of the same order as the energy loss time scale due to advection for spectral indices of the order of 2.

Hadronic interactions

If a cosmic-ray proton with sufficient energy interacts with an ambient gas atom it will be scattered inelastically. A cascade of lower energy particles will be created as a result of the scattering. π mesons are among the dominant scattering products. All three types of pions ($\pi^{\pm}, \pi^0$) are produced approximately equally often. While the charged pions will decay into μ and ν_μ pairs, the neutral π^0 will decay (almost instantaneously) into a photon pair. The production of π-mesons is only possible if the fraction of the cosmic-ray protons kinetic energy that is transferred to the newly created pion exceeds the production threshold of $E_{\mathrm{Thresh}} = 2\, m_\pi c^2 (1 + m_\pi / 4\, m_p) \approx 280\,\mathrm{MeV}$. CRs with energies below this threshold will ionise the gas.

Since a whole cascade of secondary particles is created in the collision, effective γ-ray production will only take place if the fraction of energy transferred is large enough. This requires the neutral pion to be one of the leading particles in the cascade. The mean fraction of the protons kinetic energy transferred to the π^0-meson is ≈ 0.17 in the GeV to TeV energy range [68]. The cross-section for proton-proton interaction rises rapidly to about 30 mb at the energy-threshold of 280 MeV. At higher energies (above ≈ 2 GeV) it continues to rise only logarithmically. A good approximation of the inelastic cross-section was introduced by Kafexhiu et al. [69] and is displayed in Fig 2.2. The gamma-ray spectrum expected from π^0 decay therefore traces this rise in the cross-section and drops rapidly around the production threshold. This is the aforementioned pion-bump, the smoking gun signature for proton acceleration which was found in the γ-ray spectra of the two Galactic SNRs, IC 443 and W 44 [62].

The loss time of *pp* interactions can be expressed as $\tau_{pp} = (0.5\, n_g\, c\, \sigma_{pp})^{-1}$ [68]. Due to the high gas density n_g in starburst galaxies (which is a factor of a few hundred higher than the average found in our galaxy), *pp*-interactions are a dominant energy loss mechanism for CRs in such an environment. Employing an average value of $\sigma_{pp} \approx 33\,\mathrm{mb}$ and a gas number density $n_g \approx 500\,\mathrm{cm}^{-3}$ one obtains a loss time of the order of $\tau_{pp} \approx 10^5\,\mathrm{yr}$ which is again in the same order as the advection loss time.

Diffusion

Another important particle escape mechanism is diffusion. In the *Leaky Box* picture [73], particles traversing the interstellar medium are scattered on the magnetic field irregularities, effectively randomising their trajectory. This randomisation produces the high level of isotropy of the arrival directions of CRs on Earth. As the scattering on the magnetic field is the central action, a dependency on the rigidity of the particles is expected. The chance for a particle to escape from the galaxy due to a random scattering is therefore larger for particles with higher energies. Diffusive CR escape is accordingly negligible at the lowest energies, since the CRs gyro-radius is much smaller than the size of the region.

The most accurate measurement of the rigidity dependence of diffusion in our galaxy originates from the flux ratio measurement of primary and secondary nuclei. Most prominently the boron to carbon ratio is considered for such studies. While carbon is thought to be mainly produced and accelerated in CR sources, boron nuclei are likely produced only in collisions of heavy nuclei (e.g. carbon and oxygen) with interstellar matter. The ratio B/C is $\propto h/D$ at high rigidities, with h being the halo hight of the region and D being the diffusion coefficient. The energy dependence is found to follow a power law in particle rigidity $\propto R^{-\delta}$. Currently the energy dependence is measured to $\delta \approx 0.3$ [74].

Such measurements are of course not possible to carry out in distant galaxies. We can still evaluate the diffusion in NGC 253 based on theoretical arguments. Based on the assumption, that an isotropic diffusion model is able to capture all particle dynamics in the region. For a typical escape times $\tau_{\rm diff}$, the diffusion equation can be expressed as $D\nabla^2 N - N/\tau_{\rm diff} = 0$ which can be simplified to [see chapter 15.7 of 32]

$$D \approx \frac{L^2}{\tau_{\rm diff}} \tag{2.2}$$

where L denotes the size of the region. Diffusion is in competition with advection. As discussed above, the diffusion time goes to infinity at low energies. Therefore, particle escape should be completely dominated by advection at low energies. This can be translated into an upper limit on the diffusion time if we assume our common geometry, yielding the formula for the diffusion time $\tau_{\rm diff} = (H/2)^2\, D^{-1}$. The limit can be calculated by requiring $\tau_{\rm ad} \approx \tau_{\rm diff}$, which corresponds to diffusion coefficients of $D < \mathcal{O}(10^{27}\,{\rm cm^2\,s^{-1}})$. This is three orders of magnitudes below the value found for our galaxy of $D_{\rm gal} \approx 1.5 \times 10^{30} (E\,/1\,{\rm TeV})\,{\rm cm^2\,s^{-1}}$. Additionally, the slowest possible diffusion, corresponding to scattering in a completely randomised magnetic field, can be considered. This scenario corresponds to the Bohm limit which is given by $D_{\rm Bohm} \approx 1.2 \times 10^{25} \times (E/40\,{\rm TeV}) \times (100\,\mu G/B)$ with E being the particles energy and B the (rather uncertain) magnetic field strength in the strongly magnetised starburst environment. Converting this back to the diffusion time yields $\tau_{\rm diff}^{\rm Bohm} = \mathcal{O}(10^8{\rm yr})$, much longer than the previous estimate and in the same order as the duration of a typical starburst phase.

A more precise estimate of the diffusion time scale would be possible if a break in the γ-ray spectrum would be seen. As this is not the case in current starburst galaxy γ-ray measurements, one has to assume that advection dominates over the whole energy range currently probed by γ-ray experiments. Further arguments in favour of this assumption come from theoretical considerations: The winds in starburst galaxies are typically very strong due to gas heating which can not be compensated for by radiative cooling, which implies the dominance of advection. CRs are also able to amplify magnetic fluctuations which are expected to be large due to the high rate of SNe in the small volume. This effect is again favourable for advection [68], rendering diffusion a subdominant energy loss in starburst environments up to CR energies of tens of TeV which corresponds to a few TeV in γ-ray energies.

Combined particle transport

All discussed processes can be combined in the transport equation of particles $f(\mathbf{x}, p, t)$ [75]:

$$\frac{\delta f}{\delta t} + \nabla(\mathbf{v}f - D\nabla f) - \frac{1}{p^2}\frac{\delta}{\delta p}\left(p^2 \frac{p}{3}(\nabla \mathbf{v}) f\right) = Q(\mathbf{x}, p, t) - \frac{f}{\tau_{pp}} \tag{2.3}$$

Q is the particle production rate of the CR sources. In a steady state approximation the first term $\frac{\delta f}{\delta t} = 0$, which corresponds to the case that γ-ray measurements probe the recent starburst history during which only small changes occur. The previously discussed energy losses can be recognised: $\frac{p}{3}(\nabla \mathbf{v})$ corresponds to the energy loss due to adiabatic expansion and $\frac{f}{\tau_{pp}}$ corresponds to hadronic interactions. $(D\nabla f)$ is the diffusion term with D being the energy dependent diffusion coefficient which is assumed to be independent of the distance to the source. The gradient of the $(\mathbf{vf})$ term corresponds to advective particle transport.

The integration over the starburst volume, and the CR momentum in which pion-production is possible (multiplied with the kinetic energy of the particle) allows to rewrite the transport equation into the following approximate balance relation (see appendix of [57] for details):

$$E_{pp}^{\pi}\left(\frac{1}{\tau_{\mathrm{ad}}}+\frac{1}{\tau_{\mathrm{adiab}}}+\frac{1}{\tau_{pp}}\right)\approx Q^{\pi} \tag{2.4}$$

E_{pp}^{π} is the energy in CRs above the pion-production threshold and Q^{π} accordingly the CR energy input rate above the pion-production threshold provided by the sources. Based on this formula it is evident, that all three dominant processes, namely advection, adiabatic expansion and *pp*-interactions, remove a fraction of the CRs which are produced in the sources. The effect depends only on the respective loss-time. γ-ray observations can be used to infer the fraction that is lost in *pp*-interactions. The remaining fraction of CR energy that is lost has to be modelled based on the astrophysical conditions of the starburst region.

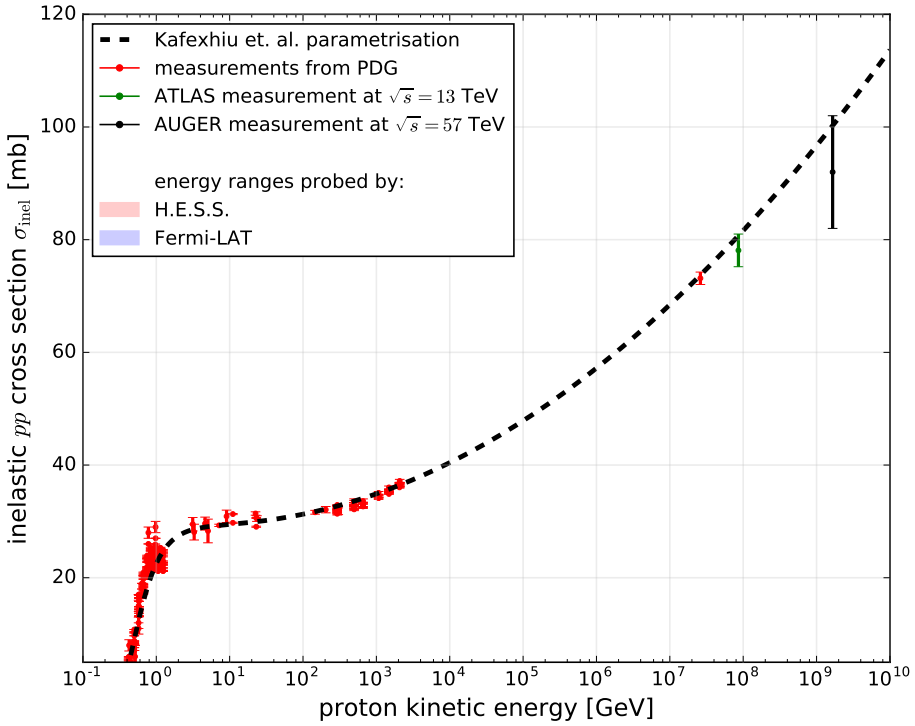

Figure 2.2: The cross-section for inelastic pp interactions as a function of the kinetic energy of a proton (calculated for a fixed target scenario in order to reflect the situation of a high-energy CR interacting with a gas atom that is approximately at rest). Both the pion-production threshold of ~ 300 MeV and the logarithmic rise are easily identified. The dahed line indicates the parametrisation from [69]. Measurements of the cross-section collected in the PDG [70] and the ATLAS [71] and AUGER [72] experiments are indicated in red, green and black respectively. The blue and red shaded areas correspond to the proton kinetic energies which are probed by *Fermi*-LAT and H.E.S.S. respectively. The approximation describes the data quite well, while the major part of the energy range probed by H.E.S.S. relies on the extrapolation over a large energy range.

2.2 The γ-ray Spectrum of NGC 253

NGC 253

NGC 253, depicted in Fig 2.3, is the most prominent starburst galaxy in the Southern hemisphere. It is part of our extended local group and is extensively measured in all wavelengths. Apart from M82 in the Northern hemisphere there is no other starburst galaxy which is found to emit γ-rays up to the VHE regime.

The origin of the starburst phase in NGC 253 is still an open question. The galaxy is in an fairly isolated environment compared to other star forming systems, making close encounters with neighbouring galaxies an unlikely option. Das et al. [77] modelled the velocity fields in the centre of NGC 253 and found them to be twisted. Das et al. argue that this is suggestive of an object with $10^6\,M_\odot$ which was accreted about 10^7 years ago and thus triggered the starburst activity we observe today. Lucero et al. [78] argue that the hard X-ray observations presented in [79] show indications for a double nucleus which would further support this merger scenario.

Tightly connected to the question of the starburst origin is the discussion if NGC 253 contains an active galactic nucleus (AGN) or not. The strongest source in the nucleus found in VLA observations of NGC 253, reported by Ulvestad and Antonucci [80], is *TH2* and was found to be consistent with a low-luminosity AGN at the time. Similar arguments were made based on the X-ray emission observed with Chandra from a central source in the NGC 253 starburst region in 2002 by Weaver et al. [81]. Deep 22 GHz VLBI observations with the VLA, reported in [82] found that such a AGN hypothesis is disfavoured and that the central region of NGC 253 is dominated by the starburst activity. On this basis, the line of argumentation presented in section 2.1 can nicely be applied to NGC 253.

The rate of supernovae in the starburst nucleus is of central importance for the discussion of the outlined paradigm that CRs are accelerated in SNRs. The supernova rate can be estimated using several methods, with one of the methods being based on the number, size and expansion rate of supernova remnants. In a detailed discussion of this approach, Lenc and Tingay [83] used the population of supernova remnants detected in the nucleus of NGC 253. They find that approximately 50 % of all detected radio sources in the nucleus can be associated with supernova remnants which have on average a size of 3 - 8 pc. The resulting upper limit on the supernova rate is $\nu_{\mathrm{SN}} < 0.14 \left(\frac{v}{10^4\,\mathrm{km\,s^{-1}}}\right) \mathrm{yr}^{-1}$ with v being the average expansion speed of the remnants. Lenc and Tingay [83] additionally discuss an estimate of the supernova rate based on the far infrared emission. If one assumes that all energy of supernovae is thermalised over time, the measured far infrared luminosity can give an upper limit on the supernova rate. This limit amounts to $\nu_{\mathrm{SN}} < L_{\mathrm{FIR}}/E_{\mathrm{SN}} \approx 1.1 \times 10^{44}\,\mathrm{erg\,s^{-1}} \,/\, 10^{51}\,\mathrm{erg} \approx 3.5\,\mathrm{yr}^{-1}$ with the canonical assumption of an energy release of 10^{51} erg per supernova. This limit is however a dramatic overestimate as far infrared emission is also known to originate from gas which was heated by stars.

A more careful exploitation of the proportionality of the far infrared luminosity to the supernova rate was described in [84]. With this method a supernova rate of $\nu_{\mathrm{SN}} = 0.03\,(0.08)\,\mathrm{yr}^{-1}$ was obtained, where 0.08 corresponds to the total supernova rate of NGC 253, while the rate in the starburst nucleus alone is $\approx 0.03\,\mathrm{yr}^{-1}$ assuming an outdated distance measurement of NGC 253 of 2.5 Mpc [85]. This value still holds significant uncertainty. Based on the supernova rate in this order of magnitude, Melo et al. [86] found that the mass of stars being formed in NGC 253 amount to roughly $5\,M_\odot\,\mathrm{yr}^{-1}$ in the nucleus alone which is 70 % of the entire galaxy's star formation rate.

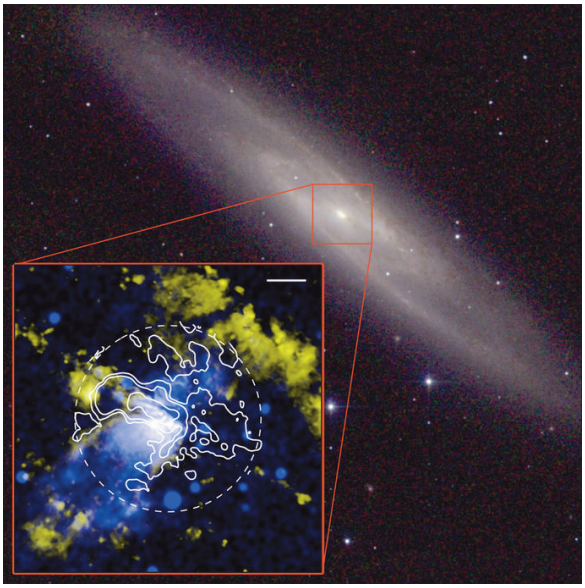

Figure 2.3: The starburst galaxy NGC 253 pictured by 2MASS. The inset shows a false color zoom of the nuclear starburst region with blue indicating soft X-rays and yellow indicating $H\alpha$ emission. The contours represent radio emission measurements. The X-ray emission nicely depicts the plasma flowing out of the starburst nucleus, which is refered to as *superwind* in this work. The picture has been taken from [76]

The morphology of the starburst region in NGC 253 is largely based on high resolution X-ray observations. Weaver et al. [81] argue that the nucleus is surrounded by a rotating dusty torus with an absorbing column density of $N_H = 10^{23}\mathrm{cm}^{-2}$ based on absorption features. Due to the density of this torus it collimates the outflow of the starburst region to a superwind with a velocity of $v_{\mathrm{wind}} \approx 300\,\mathrm{km/s}$.

The most important astrophysical parameters of NGC 253 are collected in Table 2.1. These values will be used throughout this work as they allow for estimates of the CR population in NGC 253 independent from the γ-ray measurement. Some of the values (e.g. the Supernova rate) depend on the distance of NGC 253. Therefore, the uncertainty in the distance measurement propagates into additional uncertainties for these parameters.

Table 2.1: Astrophysical parameters of the starburst region in NGC 253.

Parameter	symbol & unit	value	Reference
Distance	d [Mpc]	3.5 ± 0.2	[87]
Starburst nucleus radius	r [pc]	150	[81]
Starburst nucleus hight	H [pc]	60	[81]
Supernova rate	ν_{SN} [yr^{-1}]	0.05 - 0.15[1]	[85]
Gas density	n_g [cm^{-3}]	580	[88]
Total gas mass	M_g [$M_\odot$]	6×10^7	[86]
Super-wind speed	$v_{\mathrm{wind}}[km\,s^{-1}]$	≈ 300	[67]

NGC 253 was first detected in VHE [56] and HE [89] γ-rays in 2009. Since then several updates on the γ-ray measurements were presented. In the following, the most up-to-date γ-ray data from 100 MeV to 5 TeV will be discussed. This is an update to the currently best estimate of the NGC 253 very-high-energy γ-ray spectrum which was presented in [57]. The HE γ-ray spectrum was reported in several publications since the initial detection in 2010: As part of a population study of starforming systems by Ackermann et al. [90] in 2012, as well as one of the sources in the 3FGL [91] in 2015 in which data from 4 years of *Fermi*-LAT observations were employed.

High-Energy γ-rays from NGC 253

The LAT on board the *Fermi* satellite is the most sensitive HE γ-ray experiment in operation. Since its start in 2008 it accumulated more than 8 years of data which is available to the public. The release of pass 8 data products [92] allowed for an additional gain in sensitivity and performance. These improvements are most notably at the lower energy end of the *Fermi*-LAT energy range of around 100 MeV, where differences between hadronic and leptonic emission processes are best visible. Improvements at the higher energy end are also important in order to have a full coverage, even in between the core energy ranges of H.E.S.S. and *Fermi*-LAT. Therefore, a new analysis of this source with more than double the statistics and improved performance was performed.

Fermi-LAT data

The datasets of observations towards NGC 253, used in this analysis, spans from 04 Aug 2008 to 26 Jan 2017 (which corresponds to MET 239557417 - MET 507108410), more than 8 years in total and a factor two more than the dataset used in [57]. The analysis followed the standard *Fermi*-LAT analysis procedures and is based on the *Fermi*-LAT science tools[2].

γ-rays in a square region of interest (ROI) of $15 \times 15\,\mathrm{deg}^2$ centred on the optical centre of NGC 253 were considered in the analysis. Cuts to suppress albedo background events from the Earth's limb were imposed as well as restrictions to the zenith angle under which the region of interest was visible for the LAT. The exact requirements are spacecraft tilts of less than 52 deg and angles between the ROI and the instruments pointing direction of less than 90 deg. γ-rays with energies down to 30 MeV were considered in the analysis in order to circumvent biases due to energy dispersion effects at low energies.

New HE γ-ray spectrum

Instrument response functions of version P8_R2_v6 were employed for the spectral analysis. In a first pass, a likelihood analysis in the energy range from 60 MeV to 500 GeV was performed using the *gtlike* tool. Not only γ-ray emission from NGC 253 was considered in this fit. Also γ-ray emission from all known 3FGL sources in the ROI as well as the diffuse galactic γ-ray emission (as modelled in *iso_P8R2_SOURCE_V6*) and the isotropic diffuse γ-ray emission (as modelled in *gll_iem_v06*) were considered as background contribution to γ-ray emission from NGC 253. The spectral parameters of all components were left free during this fit. NGC 253 is re-detected with a significance of $\sim 22\,\sigma$ (or a TS value of 480). The flux of

[1] This value has been rescaled to the most up to date distance estimate of 3.5 Mpc from the values cited in the text.

[2] v10r0p5, `http://fermi.gsfc.nasa.gov/ssc`

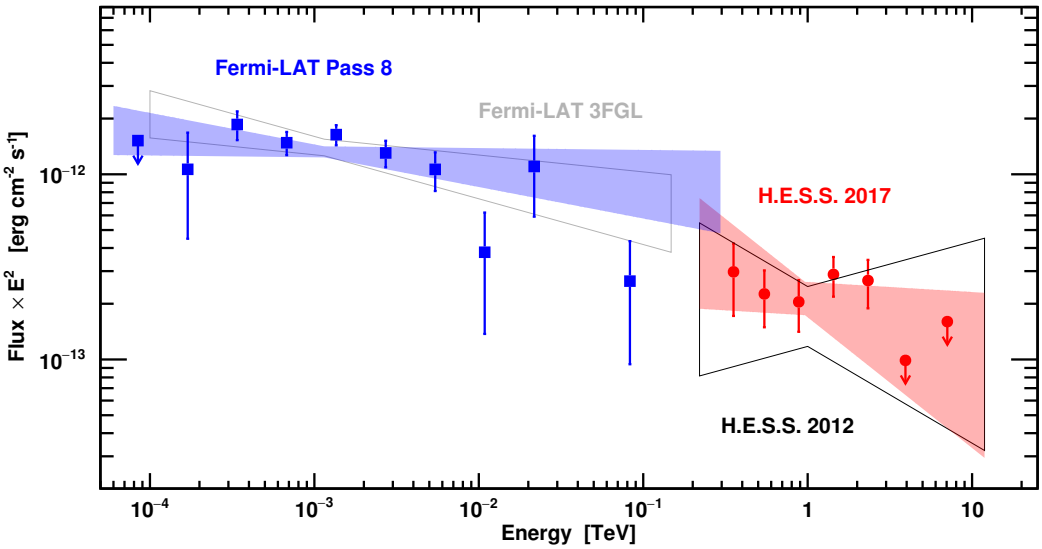

Figure 2.4: H.E.S.S. and *Fermi*-LAT Pass 8 γ-ray spectral energy distributions are shown in red and blue, respectively. All error bars represent 1σ statistical uncertainties. The upper limits are given at 95% confidence level. The red shaded area represents the 1σ confidence region of the H.E.S.S. fit with combined statistical and systematic uncertainties. The black contour shows the 1σ confidence region of the H.E.S.S. fit from [57]. The grey box shows the *Fermi*-LAT 3FGL best fit. Note that the *Fermi*-LAT measurement uncertainties are dominated by the low statistics. The systematic error of the *Fermi*-LAT points range from 5 % to 20 %. The blue area shows the best fit power-law to the *Fermi*-LAT Pass 8 data.

NGC 253 above 60 MeV $F(E > 60\,\mathrm{MeV})$ amounts to $1.56 \pm 0.28^{\mathrm{stat}} \pm 0.15^{\mathrm{sys}} \times 10^{-8}$ cm^{-2}s^{-1}. The best fit spectral index assuming a power-law model is $\Gamma_{\mathrm{HE}} = 2.09 \pm 0.07^{\mathrm{stat}} \pm 0.05^{\mathrm{sys}}$.

In a second pass of the fit, the spectral energy distribution is derived in discrete energy bins. Nine logarithmic spaced bins in the energy range from 60 MeV to 30 GeV were chosen. The high end of the energy range (30 GeV to 300 GeV) was merged due to the low expected γ-ray statistics. A new likelihood analysis was performed in each bin. This time the spectral parameters of all background contributions were fixed to the values obtained in the global fit before. Only the normalisation of the diffuse components and NGC 253 were left free. The resulting spectral energy distribution of NGC 253 is shown in Fig 2.4 in blue. All spectral points correspond to a significance of at least $2\,\sigma$. At the lowest energies (60 to 120 MeV), NGC 253 is not detected significantly. The emission in this energy range is constrained by the upper limit displayed in Fig 2.4 at 95 % confidence. The highest energy photon detected from the direction of NGC 253 had an energy of 214 GeV. When the energy resolution of ~ 8 % at 215 GeV is considered, the highest energy bin is limited to 230 GeV. The statistical uncertainties of the highest energy points are on the level of 50 % which diminishes the chance to find structure in the transition between the HE and VHE γ-ray bands.

Very High Energy γ-rays from NGC 253

Observations towards NGC 253 were carried out in 2005 and from 2007 to 2009 with all four 12 m H.E.S.S. telescopes. The data used in this work are identical to the data presented and analysed in [57]In total the dataset amounts to 241 hours of data. Restricting the sample to observations with at least three telescopes yields 162 h of total lifetime. The observations were performed at zenith angles ranging between 1 and 42 deg with a mean value of ~ 12 deg. The target position was observed in *wobble-mode*, meaning that the target position was offset from the centre of the field of view in alternating directions for an improved homogeneity of the exposure and allowing for a better background estimation due to more available off regions.

H.E.S.S. Data Analysis

The analysis follows the procedures described section 1.3 and utilised the *model analysis* [43]. The much improved sensitivity of the model analysis compared to the classical Hillas parameter based analysis depends on the accurate modelling of the camera positions with respect to the telescope dishes. As such it is more susceptible to imperfections in the description of the instrument response than the simpler Hillas parameter based analysis. Since the publication in 2012, a misalignment in the description of the camera positions with respect to the telescope dishes was found. This was not fully corrected for in [57]. It was found that the misalignment resulted in a broader point spread function as well as a shift in the γ-ray classification parameter of the model analysis towards the non-γ-ray parameter range. The classification parameter shift introduced an underestimation of the γ-ray flux, further motivating a renewed analysis of the NGC 253 data. The same misalignment was encountered in the analysis of N 157B in the Large Magellanic Could [93, supplement]. In the case of N 157B it was further noted, that the cross-check analysis is less susceptible to such effects as it uses image-based parameters instead of a pixel-wise likelihood and was not affected. The estimated flux of NGC 253 differed in the order of 60 % between the main and the cross-check analysis and was taken into account as a systematic uncertainty at the time. A renewed analysis of the data might therefore significantly reduce the measurements uncertainties.

VHE γ-ray spectrum

In addition to the γ-ray spectrum, an updated position, extension limit and light curve were derived.

The source is detected with a slightly lower significance of $7.2\,\sigma$ compared to $8.4\,\sigma$ in [57]. The updated source position is RA $= 0\mathrm{h}\,47\mathrm{m}\,32.54\mathrm{s} \pm 0\mathrm{m}\,11.2\mathrm{s}$, Dec $= -25\mathrm{d}\,17'\,25.4'' \pm 0'\,10.3''$ (J2000), which changed only marginally towards an even better agreement with the optical center of NGC 253 at RA $= 0\mathrm{h}\,47\mathrm{m}\,33.1\mathrm{s}$, Dec $= -25\mathrm{d}\,17'\,18''$.

As the point-spread function improved due to the accurate modelling of the camera position, an extension of the γ-ray emitting region in NGC 253 is even better constrained to $\leq 1.4'$ at $3\,\sigma$ compared to $\leq 2.4'$ in [57]. The new extension limit of the γ-ray emission is below the apparent size of the entire galaxy of $30.7' \times 7.3'$ [94], but still much larger than the size of the starburst region.

The γ-ray spectrum was extracted at the best fit position. The background subtraction for the spectral analysis was estimated using the *MultipleOff* method [46]. The chosen model hypothesis for the unbinned spectral fit is a power-law. The best fit is depicted in Fig 2.4 as

the red shaded band. The flux normalisation $F_0(1\,\mathrm{TeV}) = (1.34 \pm 0.14^{\mathrm{stat}} \pm 0.27^{\mathrm{sys}}) \times 10^{-13}\,\mathrm{cm}^{-2}\,\mathrm{s}^{-1}\,\mathrm{TeV}^{-1}$ is $\sim 40\,\%$ higher, and the best-fit spectrum is with a spectral index of $\Gamma_{\mathrm{VHE}} = 2.39 \pm 0.14^{\mathrm{stat}} \pm 0.25^{\mathrm{sys}}$ somewhat softer yet consistent within errors compared to [57], where a spectral index of $\Gamma^{2012} = 2.14 \pm 0.18^{\mathrm{stat}} \pm 0.30^{\mathrm{sys}}$ and a normalisation at 1 TeV of $F_0^{2012} = (9.6 \pm 1.5^{\mathrm{stat}}\,(+5.7, -2.9)^{\mathrm{sys}}) \times 10^{-14}\,\mathrm{TeV}^{-1}\,\mathrm{cm}^{-2}\,\mathrm{s}^{-1}$ was reported. Regardless of the flux increase, NGC 253 remains the faintest γ-ray source detected at TeV energies.

The spectral points depicted in Fig 2.4 have a minimum significance of $2\,\sigma$. At energies beyond 4 TeV, there are not enough photon candidates, such that two upper limits with 95 % confidence are given.

A power-law fit to all data points at energies above 3 GeV is found to yield a spectral slope of $\Gamma_{\mathrm{HE-VHE}} = 2.22 \pm 0.06^{\mathrm{stat}}$. The integrated γ-ray flux using the whole γ-ray measurement translates into a γ-ray luminosity of $L_\gamma = (1.19 \pm 0.35^{\mathrm{stat}}) \times 10^{40}\,\mathrm{erg\,s}^{-1}$ using a distance of $d = 3.5\,\mathrm{Mpc}$.

Estimation of systematic uncertainties

In [57], the estimated systematic uncertainties were dominated by the comparison between the main and cross-check analysis. This comparison is often employed as both chains use fully independent calibration and reconstruction chains and γ-ray classification algorithms. As the cross-check framework was found to be unaffected by the camera position modelling, its results are still being used as a cross-check. In [57], the difference in the flux normalisation between the two analysis chains was found to be 50 %, while the re-analysed flux normalisations agrees within 2 %. The best fit spectral index differs at the 10 % level. As 2 % are likely a major underestimation of the systematic uncertainties further tests within the model analysis framework were performed.

One potential systematic uncertainty can be introduced by applying data quality criteria which are identical to the ones used in [57]. Comparing the spectral results with up to date data selection criteria yielded a flux difference of 10 % and change in the spectral index of 3 %.

The analysis was performed using cuts which were optimised for faint sources with low signal to noise ratios. The specific choice of cuts might alter the results systematically. Therefore the analysis was repeated using standard cuts which most importantly have a less restricting cut on the image brightness. The comparison yielded differences of 13 % and 5 % in the flux normalisation and spectral index respectively.

In addition to choices made in the analysis of the data, there are general uncertain aspects for any analysis of IACT data. Most importantly the limited knowledge of the atmospheric conditions, such as the density profile over the course of the observations, may change analysis results. The light yield of Cherenkov light from atmospheric showers is uncertain by $\sim 10\,\%$. In order to estimate the influence of this, the effective area was artificially shifted by $\pm\,10\%$ in energy during the fit. The comparison to the standard analysis results indicated uncertainties on the level of 10 % and ± 0.09 for the flux normalisation and the spectral index respectively.

All studied aspects are summarised in table 2.2. A conservative estimate of the overall systematic uncertainties associated to the chosen analysis approach of the NGC 253 data set is obtained by summing the individual components quadratically. The total systematic uncertainty is included in the red shaded area in Fig 2.4. The uncertainties of the data points in this figure correspond to the statistical uncertainties only. The systematic uncertainties are found to be on a comparable level to the statistical uncertainties and therefore no longer dominate the uncertainty of the γ-ray flux estimation. The black contour in Fig 2.4 indicated

the 68 % containment systematic and statistical uncertainty of NGC 253's γ-ray flux estimate reported in [57]and highlight the improvement.

Table 2.2: Estimated systematic uncertainties of the H.E.S.S. observations towards NGC 253.

Origin of uncertainty	spectral index	normalisation
reconstruction, calibration & analysis	± 0.19	2 %
run selection	± 0.07	10 %
selection cuts	± 0.11	13 %
atmospheric modelling	± 0.09	10 %
Total systematic uncertainty	$\pm$ **0.25**	**19 %**

2.3 Cosmic-Ray Escape and Calorimetry in NGC 253

With the accurate γ-ray flux estimates ranging from 60 MeV to 4 TeV at hand, aspects discussed in section 2.1 can be explored. It was discussed, that high-energy cosmic rays are able to loose energy or escape from the starburst nucleus via advection, adiabatic expansion, hadronic interactions or diffusion. The individual contribution can be quantified with the specifics of NGC 253 and the γ-ray flux measurements.

Efficiency of Energy Loss Processes in NGC 253

The energy loss time due to advection was reported to depend on the superwind speeds of the starburst region and its height. With the astrophysical parameters collected in Table 2.1, this loss time amounts to $\tau_{\rm ad} = (H/2)/v_{\rm wind} = \frac{60\,\rm pc}{2}\frac{1}{300\,\frac{\rm km}{\rm s}} \approx 10^5\,\rm yr$ which is much shorter than the duration of a typical starburst episode of $\mathcal{O}(10^7\,\rm yr)$. It was further motivated that diffusion and advection are competing processes. A transition between the two would be indicated by a break in the CR spectrum due to the energy dependence of diffusion. Such a break would leave its imprint in the γ-ray spectrum. The γ-ray data, however, reveal no indication for a break with the current precision. Therefore, advection should indeed dominate over diffusion up to CR energies of ~ 40 TeV which corresponds to 4 TeV in γ-ray energies.

In the estimation of the energy losses due to the adiabatic expansion of the starburst volume, a dependence on the CR spectrum was noted. The γ-ray data revealed that the spectral index is indeed of the order of 2.3, which yields an adiabatic energy loss time of $\tau_{\rm adiab} = 3\tau_{\rm ad}\frac{1}{\Gamma_{CR}-1} \approx \frac{3}{1.3}\,\tau_{\rm ad} \approx 2\times 10^5\,\rm yr$. These loss times can be compared to the estimate of the *pp* interaction loss time of $\tau_{pp} \approx 10^5$ yr. The energy loss scales with the inverse of the loss times. The ratio

$$\frac{1/\tau_{pp}}{1/\tau_{\rm adiab} + 1/\tau_{\rm ad}} \approx \frac{2}{3} \tag{2.5}$$

reveals, that hadronic interactions are in fact quite efficient in NGC 253. Out of all CRs which are removed from the starburst, two out of three are estimated to loose all their

energy in *pp* interactions rather than leaving the galaxy with the starburst wind or losing their energy through adiabatic expansion. As these are fractional estimates, an absolute estimate of the energy and particle density in CRs in the starburst region of NGC 253 is necessary.

NGC 253 as a cosmic-ray calorimeter

In order to estimate the energy in CRs, the fraction of particles (and their energy distribution) which remain in the starburst region is necessary. Since the estimate will relate to the γ-ray measurement, a statement will only be possible at proton kinetic energies above the pion-production threshold of 280 MeV. The fraction of particles with high enough energies for pion-production can be expressed as [57]:

$$E_{pp}^{\pi}\left(\frac{1}{\tau_{\mathrm{ad}}}+\frac{1}{\tau_{\mathrm{adiab}}}+\frac{1}{\tau_{pp}}\right)=Q^{\pi}=f_{\pi}\,Q \tag{2.6}$$

where Q is the total particle energy from the integral of the particle transport equation (Eq 2.3) over all momenta and the starburst volume. $f_\pi < 1$ corresponds to the fraction of particles that is capable of producing pions. Int the appendix of [57] it has been demonstrated that the fraction f_π can be estimated as $f_\pi \approx 3-\Gamma$ with Γ being the cosmic-ray spectral index which has to lie in the range of $2 < \Gamma < 3$ for the approximation to hold.

The CR spectral index can be estimated in an extreme, yet simple, scenario: One can assume, that all particles above the pion-production threshold in the starburst volume interact with the gas (called *thick* target gas scenario hereafter). In this case the observed γ-ray spectrum resembles the shape of the CR spectrum. The fit to the γ-ray data above 3 GeV yielded a best fit of $\Gamma_{\mathrm{thick}}^{CR} = 2.22 \pm 0.06^{\mathrm{stat}}$. The threshold of 3 GeV is needed to avoid the low energy part of the spectrum where kinematic effects alter the γ-ray spectrum shape. Similar to the thick case, one can build a thin target gas scenario. In this case one assumes that a set fraction of CRs is able to escape from the starburst nucleus through the processes discussed previously. In this case, the energy dependence of the *pp* interaction cross-section needs to be accounted for. Due to the logarithmic rise of the cross-section, higher energy particles are more likely to interact than low energy CRs. Therefore the observed γ-ray flux at higher energies overestimates the CR flux compared to lower energies which needs to be corrected for.

An evaluation of this *thin* target gas scenario can be achieved by making use of the astrophysical parameters of NGC 253, the full γ-ray measurement as well as an accurate parametrisation of the *pp* cross-section. A tool which allows for all this is *NAIMA* [95]. *NAIMA* employs the markov chain monte carlo technique from [96] which is implemented in *emcee* [97]. Hadronic interactions are implemented using the *pp* interaction differential cross-section from Kafexhiu et al. [69]. The CR test distributions parameters are fitted based on the comparison of the measured γ-ray spectrum and the γ-ray spectrum estimated from neutral pion decay from *pp* interactions. The pion-production cross-section is taken from PYTHIA 8 [98]. The CR spectrum assumption is a power law in proton momentum with normalisation N_0 at a reference momentum p_0 and spectral index α in the energy range from 0.1 GeV to 0.5 PeV. This spectrum is given by $N_p(E) = \frac{N(p_0)}{\beta\, c} \times \left(\frac{p}{p_0}\right)^{-\Gamma}$ for protons with total energy E, momentum p and velocity β in units of c. Using both the *Fermi*-LAT and H.E.S.S. spectral points derived before, the best fit yields a CR spectral index of $\Gamma_{CR}^{\mathrm{thin}} = 2.46 \pm 0.3^{\mathrm{stat}}$. In order to estimate the systematic uncertainties, different

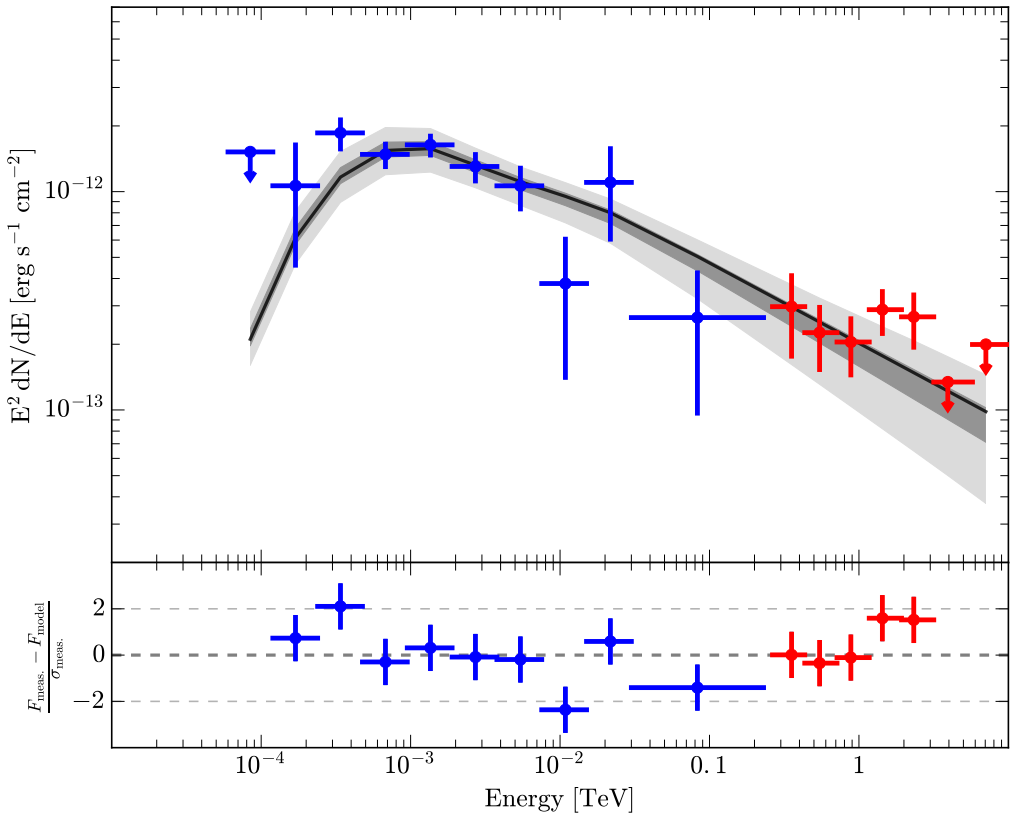

Figure 2.5: The energy flux spectral points derived previously are given in blue and red for *Fermi*-LAT and H.E.S.S. respectively. The black line indicates the γ-ray spectrum that is produced from the best fit proton population fitted with NAIMA . The statistical uncertainty of the best fit is indicated by the differently grey shaded area for 1 and 3 σ. The residual of the γ-ray measurements with respect to the best fit model are shown in the lower panel.

model descriptions of the pion-production cross-section were applied, yielding a change of the spectral index of $\pm 0.03^{\mathrm{sys}}_{\mathrm{interaction}}$. Artificially increasing/decreasing the flux of the H.E.S.S. spectral points by $\pm 20\,\%$, the estimated systematic uncertainty of the measurement, also changes the best fit index $\Gamma^{\mathrm{thin}}_{CR}$ by $\pm 0.03^{\mathrm{sys}}_{\mathrm{H.E.S.S.}}$. If the H.E.S.S. measurement is excluded from the fit, the best fit value is 2.6, which undershoots the H.E.S.S. measurement. The best fit model obtained in the thin scenario is shown in Fig 2.5 together with the γ-ray measurements.

The total CR luminosity can be estimated using the canonical assumptions that a fraction Θ of the SN kinetic explosion energy is transferred into the acceleration of CRs. The luminosity is then given by $L^{\mathrm{tot}}_{\mathrm{CR}} = \nu_{\mathrm{SN}}\,\Theta\,E_{\mathrm{SN}}$ with E_{SN} being the explosion energy per supernova and ν_{SN} being the supernova rate, factors which are all independent from the γ-ray measurement. Assuming $\Theta \approx 0.1$, $E_{\mathrm{SN}} \approx 10^{51}$ erg and $\nu_{\mathrm{SN}} \approx 16 \times 10^{-10}\mathrm{s}^{-1}$ yields a CR luminosity of $L^{\mathrm{tot}}_{\mathrm{CR}} = 1.6 \times 10^{41}\,\mathrm{erg\,s^{-1}}$. [99] shows that the explosion energy for standard

type II core-collapse supernovae roughly ranges between $\sim (0.6 - 2) \times 10^{51}$ erg with the average being roughly consistent with the canonical value of 10^{51} erg (see Fig 6 in [99]). Θ is largely uncertain. Historically it is assumed to be in the order of 10 % which dates back to the first proposal of SNRs being the sources of CRs in the Milky Way [100].

The fraction of CR luminosity which is visible in the γ-ray spectrum can be calculated with this estimate. For this, $L_{\rm CR}^{\rm tot}$ has to be corrected for the fraction of CRs with energies above the pion-production threshold $L_{\rm CR} = f_\pi \times L_{\rm CR}^{\rm tot}$ with $f_\pi \approx 3 - \Gamma$, as discussed before. The ratio of the CR luminosity inferred from the γ-ray measurement to $L_{\rm CR}$ is called the calorimetric fraction $\mathscr{F}_{\rm cal}$, as it indicates the fraction of CRs which are calorimetrically absorbed in the starburst nucleus. For the ratio, the γ-ray luminosity has to be corrected for the branching ratio $\eta \approx 1/3$, with which neutral pions are produced in *pp* interactions. The calorimetric fraction is then given by:

$$\mathscr{F}_{\rm cal} \approx \frac{L_\gamma/\eta}{f_\pi \nu_{\rm SN} \Theta E_{\rm SN}} \tag{2.7}$$

The fraction of pion producing particles f_π can be calculated for both the thin and the thick case scenarios. The resulting values are $f_\pi^{\rm thick} = 0.78$ and $f_\pi^{\rm thin} = 0.54$ with a mean of 0.66. The calorimetric value obtained using average values is

$$\mathscr{F}_{\rm cal} \approx 0.34 \left(\frac{L_\gamma/\eta}{3 \times 1.19 \times 10^{40}\,{\rm erg\,s^{-1}}}\right)\left(\frac{0.66}{f_\pi}\right)\left(\frac{15.9 \times 10^{-10}\,s^{-1}}{\nu_{\rm SN}}\right)\left(\frac{10^{50}\,{\rm erg}}{\Theta E_{\rm SN}}\right) \tag{2.8}$$

meaning that around 30 % of the CRs can not leave the starburst nucleus by any of the discussed escape mechanisms (see section 2.1), but perform inelastic hadronic interactions. Uncertainties on f_π arise from the scenario choice, as well as uncertainties on the measured γ-ray luminosity. This allows to explore the extreme values of $\mathscr{F}_{\rm cal}$. The lowest supported value of f_π is 0.48 assuming the thin target gas case with the addition of the quadratic sum of the statistic and systematic uncertainties of $\Gamma_{CR}^{\rm thin}$. If in addition the γ-ray luminosity is reduced by $1\,\sigma$, $\mathscr{F}_{\rm cal}$ reduces to ~ 0.29. The other extreme yields a value of ~ 0.90 which is very close to the calorimetric limit of 1. Values above unity would be unphysical, since the starburst galaxy can not absorb more CRs than it produces. Additional uncertainty is present in the astrophysical parameters $\nu_{\rm SN}, \Theta, E_{\rm SN}$. Their uncertainty further broaden the allowed range of calorimetric fractions. Therefore, this estimate should be seen as an order of magnitude estimate of the level of CR calorimetry in NGC 253. The presented method constrains this level of calorimetry to the range between 10 - 100 %.

2.4 Conclusions and Outlook

The most up to date analysis of NGC 253 γ-ray data shows that a significant fraction of CRs in the nucleus is lost in *pp* interactions. The estimated fraction of CRs that contribute to chemical reactions, ionisation and heating is found to be in the range from ~ 10 to 100 %, corresponding to a CR luminosity in the order of $\sim 10^{40} - 10^{41}\,{\rm erg\,s^{-1}}$. This CR luminosity can be compared to the CR luminosity of the entire Milky Way of $(0.6-3)\times 10^{41}\,{\rm erg\,s^{-1}}$ [101].

This result is remarkable also beyond the calorimetric estimate: The CR luminosity inferred from the γ-ray measurements combined with *pp* interaction measurements is in the same order of magnitude as the estimate based on the astrophysical properties of NGC 253

which are determined by radio, optical and X-ray measurements. This nicely demonstrates the power of astro-particle physics and the multi-messenger approach.

The large uncertainty in the CR luminosity estimate originates largely from the astrophysical parameters. The supernova rate estimates will likely improve with observations from SKA [102], which will allow to associate radio sources in the starburst nucleus to SNRs with unprecedented precision. Significant uncertainty will remain in the base energy input in cosmic rays from supernova remnants. The kinetic explosion energy and CR-acceleration efficiency will always vary from one Supernova to the next. Detailed knowledge of both distributions for the specific case of NGC 253 would be necessary to reduce this uncertainty.

Further improvements in the γ-ray domain are to be expected in the future. The low energy end of the γ-ray spectrum will be measured by e-ASTROGAM [103]. This is of importance as the pion-bump feature might be detectible with this data. Together with already existing X-ray measurements as the ones presented in [79], a detailed decomposition of hadronic and leptonic contributions might be possible. At higher energies ($E > 30$ GeV), the Cherenkov Telescope Array will provide high precision γ-ray data [104]. The γ-ray measurements with large uncertainties in the 10 - 200 GeV energy range will be superseded, allowing to probe for spectral breaks. Such breaks can be introduced in the transition from advection-dominated to diffusion-dominated particle escape. CTA will also measure the γ-ray spectrum to energies beyond 10 TeV, at which cutoffs due to the limit of particle acceleration in SNRs might be observable. The cutoff in γ-rays can be translated into the cutoff of the CR spectrum. The Pierre Auger Observatory observes an intermediate-scale anisotropy in the arrival directions of Ultra High Energy CRs from a direction consistent with NGC 253 [105]. The detection of a high-energy γ-ray cutoff may thus have broad implications for the search for the sources of Ultra-High-Energy Cosmic Rays. A disentanglement between γ-γ absorption effects and the acceleration limits of CR sources will be of great importance and limit the discussion of ultra-high-energy CRs and very-high-energy γ-rays in NGC 253 in a coherent way.

Starburst galaxies are also of great relevance for disciplines working with other messengers. As inelastic hadronic interactions produce pions quite efficiently, also neutrinos are expected from starburst galaxies. The decay channel is $\pi^+ \rightarrow \mu^+ + \nu_\mu \rightarrow e^+ + \nu_e + \bar{\nu}_\mu + \nu_\mu$. For every π^0 (decaying to γ-γ), two charged pions are created which decay in to 6 neutrinos in total. Neutrinos therefore outnumber γ-rays by a factor of 3. The expected neutrino flux from e.g. NGC 253 alone is however out of reach for the current generation of neutrino detectors. A large fraction of the cosmic star formation activity took place at a redshift of $z \sim 2$. As neutrinos propagate trough interstellar space without being attenuated, the neutrino signal from all starburst activity in the universe could be visible to neutrino detectors as one part of a diffuse neutrino signal [106], much like the present astrophysical neutrino flux detected by IceCube [107]. Based on the diffuse γ-ray emission seen by Fermi-LAT, starburst galaxies can only contribute a fraction of the astrophysical neutrino flux [108].

As starburst galaxies produce many massive stars, they are also likely hosts of the illusive Gamma Ray Burst (GRB) phenomenon, which was briefly introduced in chapter 1. In deed GRB distance measurements seem to trace the star-formation history of the universe. A star in NGC 253 which is massive, rapidly rotating and magnetised enough could therefore present a progenitor to a GRB. With an overall supernova rate of $\sim 0.1\,\mathrm{yr}^{-1}$ it is unfortunately very unlikely to see such an event in NGC 253 within the next century.

Chapter 3

Gamma Ray Bursts in the Multi-Messenger Era

In contrast to starburst galaxies, Gamma Ray Bursts (GRBs) are transient sources. Our understanding of the GRB phenomenon has greatly improved over the last few decades. Today we know, that they are linked to extreme supernovae and the merger of neutron stars. Due to the violence of these events, they have, and still are, being discussed as potential sources of Ultra-High-Energy cosmic rays. Additionally, gravitational waves are able to provide further insight in the progenitors of GRBs. Neutrinos might also point towards new classes of GRBs. This makes GRBs true multi-messenger phenomena.

While GRBs have been detected right at the advent of γ-ray astronomy, a detection from ground based γ-ray experiments was still not possible to date. Other transient phenomena which have been detected in γ-rays with energies up to a TeV are for instance outbursts of active galactic nuclei (AGN). One very prominent example is the extreme flare of the AGN PKS 2155-304 in 2006 [109]. During this flaring episode, the energy flux in TeV γ-rays increased by a factor of more than 15 with respect to the quiescent state. This corresponds to 7 times the flux of the Crab nebula above 200 GeV at a distance of more than 250.000 times farther away than the Crab nebula. The flare lasted less than 2 hours in total. A comparable flare has not been seen from this object since. This is a prime example of a transient γ-ray event from which first important aspects of transient astronomy can be deduced:

1. No planning of the observation is possible. The transient happens when it happens. There is no possibility to re-observe the event.

2. Events can evolve rapidly. Quick reactions are necessary in order not to miss transient events. In the case of PKS-2155 the flare was identified serendipitously during the observation of the source.

3. The brightest transients can easily outshine any other object in the sky. They can therefore provide exceptional photon statistics for detailed studies.

4. An observation of flaring sources are high risk – high gain observations. Transients in TeV γ-rays are not well predictable which can lead to null observations.

The specific knowledge that can be drawn from observations of such transients is highly dependent on the phenomenon. The central phenomenon that will be discussed in more detail in this chapter are GRBs, not only the first ever detected γ-ray source, but also the

most violent phenomenon known. Section 3.1 will give an introduction to observations of GRBs. Spectra and temporal structures observed in GRBs will be discussed in section 3.2, followed by an overview of the current paradigms which explain the origin of GRBs emission and their astrophysical origin in sections 3.3 and 3.4. Finally, aspects for GRB observations in the VHE γ-ray domain will be discussed in section 3.5.

3.1 Observations of Gamma Ray Bursts

Due to the long observational history of GRBs there is a wealth of data for this phenomenon. The first instrument that provided an extensive set of GRB observations was the Burst and Transient Source Experiment (BATSE) onboard the Compton Gamma Ray Observatory (CGRO) [5]. The 2704 GRBs BATSE detected within its 9 years of operation yielded many central findings which still build the foundation of our knowledge of GRBs today:

- GRBs are distributed uniformly in the sky, which implies that they are of extragalactic origin due to the lack of a correlation with e.g. the Galactic Plane [110] (see Fig 3.1).
- GRBs have different durations. They were classified as Long- and Short-GRBs, separated at durations of roughly 2 seconds. About 500 GRBs had a duration of less than 2 seconds, while 1500 had a duration of more than 2 seconds [111][1]. Shorter bursts were found to be slightly harder than long bursts. In addition, the emission was found to vary on timescales of ms.
- The spectrum averaged over the duration of the bursts are well described by two smoothly joint power-laws. The spectrum is typically hard at lower energies and softer at higher energies. This so-called *band-function* was very successful at fitting GRB spectra. The parameters vary from burst to burst without a universal law [112].
- The typical time-averaged energy flux is on the level of a few 10^{-7} erg cm^{-2} s^{-1} – about one order of magnitude more than the Crab nebula. The closest GRBs are typically seen at redshifts of $z > 0.1$ (still more than 400 Mpc) and even reach cosmological distances. This puts GRBs among the most luminous known explosions with isotropic equivalent luminosities in the $10^{48} - 10^{53}$ erg range.

The BATSE era was also the birth of GRB observations utilising a multi-wavelength approach: The rapid downlink of the data combined with publicly announcing detected GRBs with short delays enabled the first optical counterpart detections [113] in 1999. Such follow-ups ultimately allowed for redshift measurements. Coward et al. [114] found the mean redshift of GRBs detected by the newer transient X-ray experiment *Swift*-BAT [115] to be in the order of 2.2. GRB 090423 even held the record of being the most distant object detected until 2016 with a redshift of $z = 8.2$ [116].

Today the Gamma-ray Burst Monitor (GBM) on board the *Fermi* satellite is the leading instrument detecting GRBs. More than 2000 GRBs were detected to date with *Fermi*-GBM alone [119]. The general GRB properties observed in the BATSE era still hold. An investigation of the cataloged GRBs is shown in Fig 3.2. Pannel (b) shows the time integrated energy flux in the 10 - 1000 keV energy band as a function of the measured duration in which 90 % of the energy flux was measured. While the average GRB lasts around 10 seconds, the

[1]Not all GRBs had an accurate time measurement

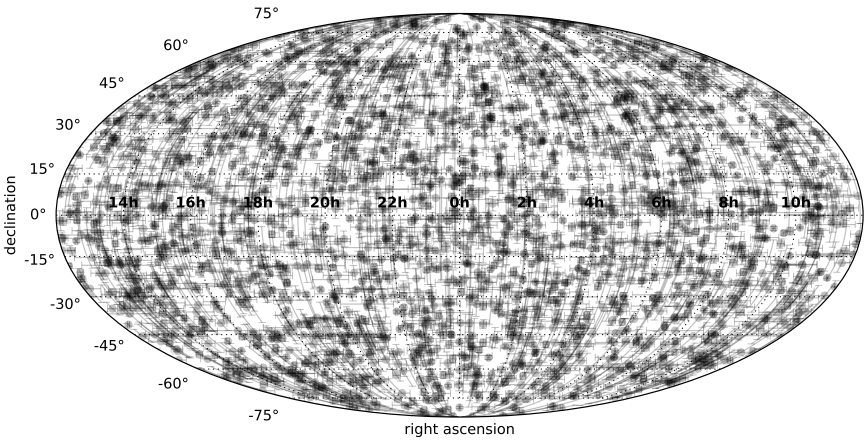

Figure 3.1: Sky map displaying all GRB localisations from BATSE. GRBs occur uniformly distributed over the whole sky. The data for the production of this figure was taken from the current BATSE GRB catalog [117, 118].

two classes of short and long GRBs are still clearly visible. Pannel (a) shows the energy flux for the same bursts as a function of the low-energy spectral index α. Comparing panels (b) and (a) from Fig 3.2, one can identify the trend that shorter GRBs exhibit harder spectra. Short bursts also exhibit higher energy fluxes than long bursts. Long bursts however tend to be more luminous as they sustain the energy flux level longer and are found to be more distant than short bursts.

Explaining the high luminosities on such short times-scales requires strong boosting. This has been extensively discussed under the term *compactness problem* [120]: In GRBs the energy released is often beyond $E = 10^{50}\,\mathrm{erg}$. At the same time the emission is found to vary on timescales of tens of ms. This limits the size of the emission region to $R \approx 3000$ km. Calculating the black-body radiation temperature T assuming the energy is distributed evenly in a sphere of radius R yields temperatures in the order of a few hundred keV and a photon density of $n \approx E/(kT\,R^3)$. Using the pair-production cross-section σ one can calculate the optical depth as $\tau \approx \sigma E/(kTR^2)$. Values in the order of $\tau \approx 10^{15}$ are obtained, meaning that all photons are performing pair production. Ultimately, the electron positron pairs would be in thermal equilibrium with the photons which is in contrast to the observed non-thermal power-law spectra. The introduction of Lorentz boosting to the emission zone circumvents such high optical depths: If the emission zone is moving towards the observer with a bulk Lorentz boosting factor of Γ, the radius from which the radiation is emitted is allowed to be a factor Γ^2 larger, which contributes squared to the optical depth. Additionally, the energy of the photons is shifted to higher energies by the boosting which results in an additional factor of $\Gamma^{2\alpha}$ with α being the measured power-law index. Both effects combined yield a reduction of the optical depth of in total $\tau_{\gamma\gamma} \propto 1/\Gamma^{4+2\alpha}$ [121]. Still boosting by a factor of $\Gamma > 100$ (in some cases even 1000) is required to reduce the optical depth to levels at which photons can efficiently escape from the emission zone. Additionally the boosting implies, that the emission is focused in jets with small opening angles of $\Theta \sim 1/\Gamma$ which isotropic equivalent luminosity estimates have to be corrected for.

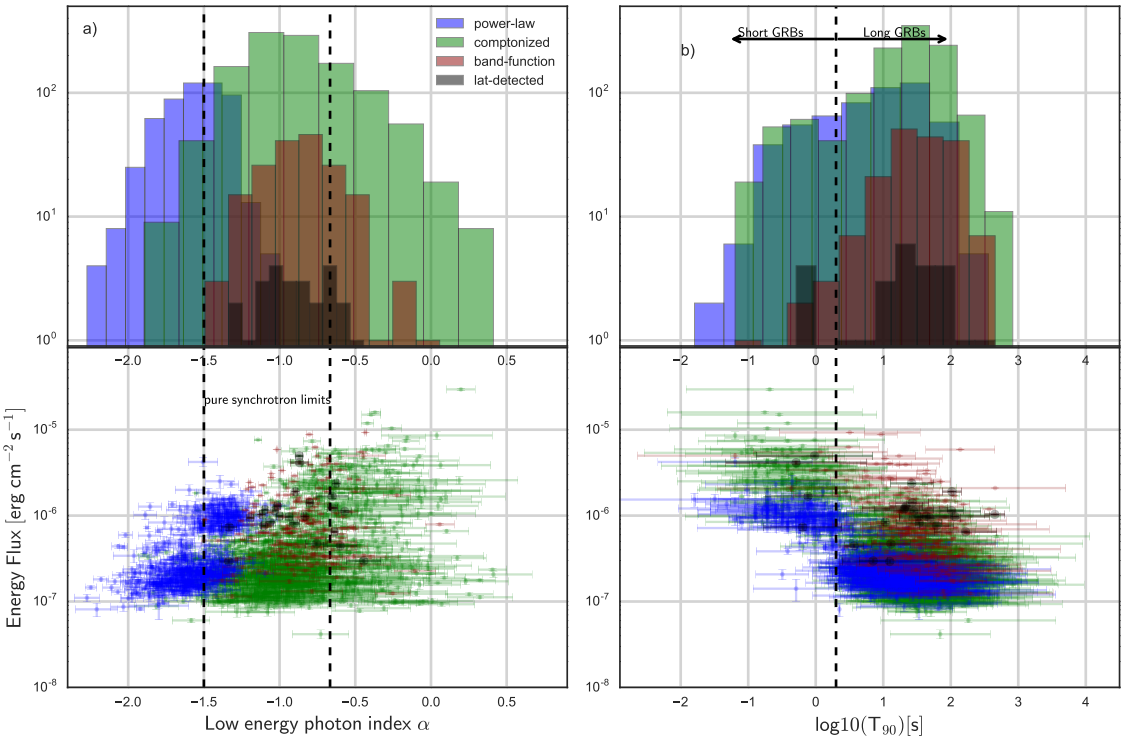

Figure 3.2: Distributions of *Fermi*-GBM detected GRBs which are best fit by power-laws, comptonized models and band-functions displayed in blue, green and red respectively. Grey corresponds to GRBs which have also been detected by *Fermi*-LAT. The left panel (a) shows the low-energy spectral index of the time integrated spectrum. The distribution is shown on top of the measured energy flux of the burst as a function of the best fit index. In the right panel (b) the low-energy index is exchanged with the time in which 90 % of the bursts flux was measured (T_{90}). One can easily identify, that short bursts typically exhibit higher energy fluxes and are harder than long bursts. The data for the creation of this plot was taken from [122, 119, 123] and [124]

3.2 Gamma Ray Burst Spectra and Temporal Evolution

GRB spectra

A phenomenological description of GRB spectra was already possible and quite successful with the previous generation of X-ray experiments. Band et al. [112] found that the spectra averaged over the duration of the bursts were well described by two smoothly joined power-laws, the so-called *band-function*:

$$f_{\mathrm{BAND}}(E) = A \times \begin{cases} \left(\frac{E}{100\,\mathrm{keV}}\right)^{\alpha} \exp\left[-(\alpha+2)\frac{E}{E_{\mathrm{peak}}}\right], & E \leq \frac{(\alpha-\beta)}{\alpha+2} E_{\mathrm{peak}} \\ \left(\frac{E}{100\,\mathrm{keV}}\right)^{\beta} \exp(\beta-\alpha)\left[\frac{\alpha-\beta}{\alpha+2}\frac{E_{\mathrm{peak}}}{100\,\mathrm{keV}}\right]^{\alpha-\beta}, & E > \frac{(\alpha-\beta)}{\alpha+2} E_{\mathrm{peak}} \end{cases} \tag{3.1}$$

This empirical function allows to represent many different spectral shapes: It represents a single power-law in the case that the low-energy spectral index α equals the high-energy spectral index β, an exponential cutoff power-law in the case that β is chosen very large.

α and β can also be chosen in relation to particle spectra population predictions which are giving rise to the observed photon spectrum.

The low-energy part of GRB spectra typically features a rather hard spectral index α with values ranging from -2 up to 0, while the high-energy part of the spectrum is softer with power-law indices β in the range of -4 to -2. The range of peak energies lies between 100 keV and a few MeV. While most bursts were well described by the band-function, the variety of the model parameters still showed that GRBs are not universally describable with a single model [112].

In today's *Fermi*-GBM era, the time averaged spectra are typically fitted with additional models:

- a simple power-law, $f_{\mathrm{PL}} \propto (E/E_{\mathrm{ref}})^{\alpha}$, with a reference energy E_{ref} and a spectral index α.
- a 'comptonized model', $f_{\mathrm{COMP}} \propto (E/E_{\mathrm{ref}})^{\alpha} \times \exp\left[-(\alpha+2)E/E_{\mathrm{peak}}\right]$ with a reference energy E_{ref}, a spectral index α and the peak energy E_{peak} after which the exponential cutoff takes effect[2].

For the sample of *Fermi*-GBM detected GRBs which are best fit with f_{BAND}, f_{PL} or f_{COMP} models, the time-integrated best fit models are shown in Fig 3.3 in colours corresponding to the same scheme as used in Fig 3.2. As *Fermi*-GBM is only sensitive in the 10 - 1000 keV energy range, the models are only valid within this energy range. Among these models, the power-law is able to fit softer spectra better with a mean value of -1.6 compared to the other two models which typically find larger values of α with a mean of -0.9. Another aspect to keep in mind is the different number of parameters of the three models of $n_{\mathrm{par}}^{\mathrm{PL}} = 2$, $n_{\mathrm{par}}^{\mathrm{COMP}} = 3$ and $n_{\mathrm{par}}^{\mathrm{BAND}} = 4$. A significant improvement of the fit with an additional parameter is not always given. This yields a large abundance of GRBs which are best fit with f_{COMP} with respect to the number of bursts which favour the band-function. The case that f_{PL} fitted the spectrum best could hint at a peak energy well beyond the GBM energy range ($>$ 1MeV). The distributions for the found indices are shown in Fig 3.2(a).

In addition to the GBM, the *Fermi* satellite features the Large Area Telescope (LAT), which provided the first sizeable sample of GRB detections at γ-ray energies above 20 MeV [124]. While EGRET detected a few GRBs [125, 126, 127] at γ-ray energies, a coherent picture of GRBs at these energies was out of reach with this sample size. The *Fermi*-LAT GRB catalog examined 733 GRBs detected by *Fermi*-GBM and detected 35 GRBs above 20 MeV out of which 28 were also detected above γ-ray energies of 100 MeV, a fraction of less than 5 %. The best fit models based on the *Fermi*-GBM detection for the small sample of LAT detected bursts are highlighted in cyan in Fig 3.3. The fraction of detected GRBs above 10 GeV is even smaller and lies below 1 % [128].

Partially this low fraction is expected due to the constraints of the instrument, namely the relatively small field of view of the LAT. The fraction of bursts detected by the LAT with respect to all GBM detected bursts recorded inside the LAT field of view is in the order of 10 %. Above 10 GeV, the fraction of detected GRBs is below 1 % [128]. Around 10 GRBs are detected by the LAT per year. Due to the recent improvement in the LAT performance (Pass 8) [92] this detection rate has increased recently by 50 % to roughly 15 GRBs per

[2]Comptonization describes the energy transfer from a thermal electron plasma with temperature T_e to photons by means of Compton scattering in the Thomson regime. The energy gained by the photons per collision is proportional to T_e and leads to a power-law spectrum with an exponential-cutoff at the characteristic energy of the plasma [32].

year [129]. The comparison of the peak energy flux of the LAT and GBM detected bursts in Fig 3.3 shows that *Fermi*-LAT typically only detects GRBs which are bright in the 100 - 1000 keV energy range.

The LAT detected sample of GRBs is best fit with a hard component with a photon index of ≈ 2 which extends into the GeV energy range on top of the band model. In fact, a simple extrapolation of the best fit model based on the GBM measurement shown in Fig 3.3 would not allow for a *Fermi*-LAT detection in most cases as indicated by the 30 s sensitivity limit of the LAT [128]. An example for this additional spectral component is visible in GRB 130427A. Both the spectrum and the light curve of this burst are shown in Fig 3.5 [130]. The spectrum (c) clearly shows the additional power law component with a comparable energy flux level as the peak of the band function.

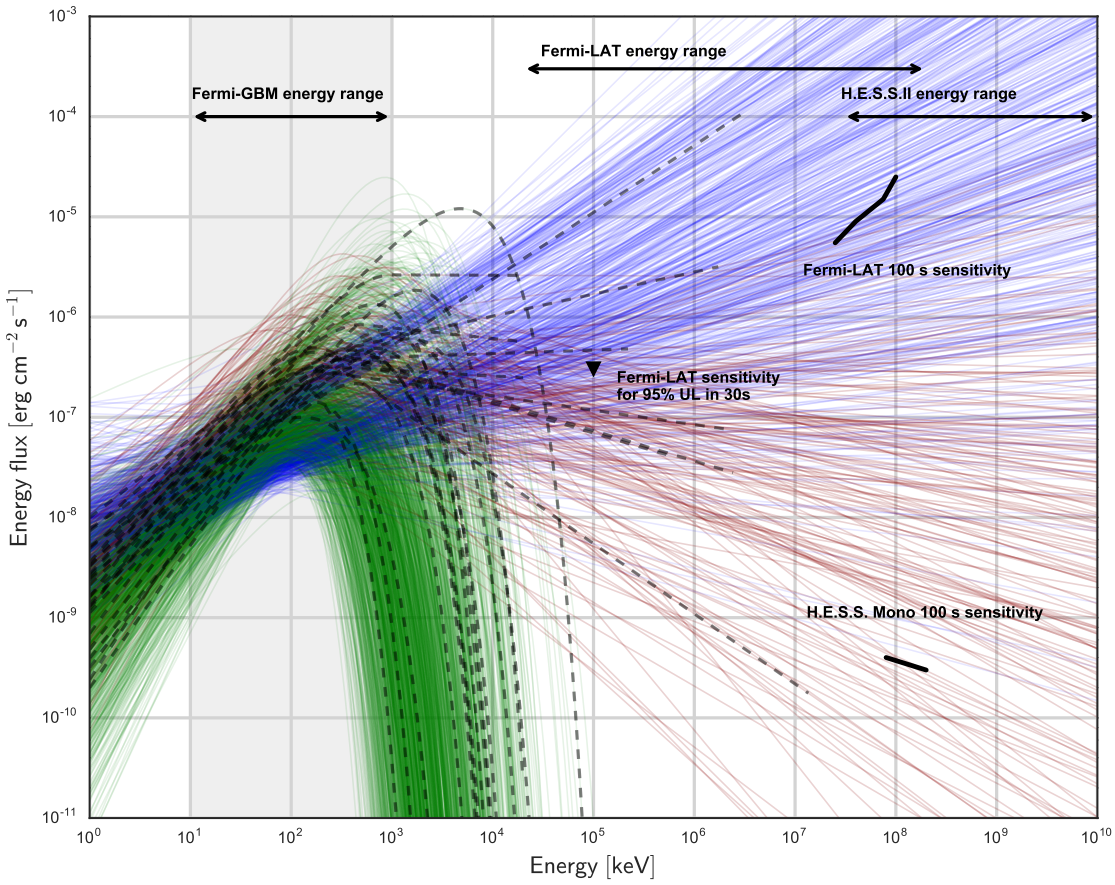

Figure 3.3: Shown are extrapolated best fit spectral models of GBM detected GRBs coloured according to the colour scheme in Fig 3.2. The ones also detected by *Fermi*-LAT are highlighted as dashed black lines and are drawn up to the highest energy photon detected by the LAT. The solid lines indicate energy ranges of different experiments and their sensitivities. H.E.S.S. II typically achieves sensitivities in the oder of $10^{-11}\,\mathrm{erg\,cm^{-2}\,s^{-1}}$ on a timescale of 30 minutes around 100 GeV. The grey shaded area indicates the energy range of *Fermi*-GBM. The extrapolated models are only valid within this energy range. The sensitivities of both *Fermi*-LAT and H.E.S.S. in the high-energy range are indicated by the solid black lines. The H.E.S.S. sensitivity is taken from Fig 1.8. The LAT sensitivity is from `https://www.cta-observatory.org/science/cta-performance/` *prod3b-v1*. Additionally the *Fermi*-LAT sensitivity for 95 % confidence level upper limits within 30 seconds is indicated by the black arrow [128]. It is evident, that *Fermi*-LAT detected numerous GRBs which are well below their sensitivity. H.E.S.S. is able to probe such GRBs with 5 orders of magnitude better sensitivity at around 100 GeV. The data for the creation of this plot was taken from [122, 119, 123] and [124].

GRB Temporal evolution

GRBs feature a wide variety of temporal structures in addition to the spread in duration spanning 5 orders of magnitude (see Fig 3.2 b). Fig 3.4 shows a selection of prompt emission light curves of GRBs detected by BATSE. In addition to a single peak of emission, precursors and multiple peaks can appear in the light-curve.

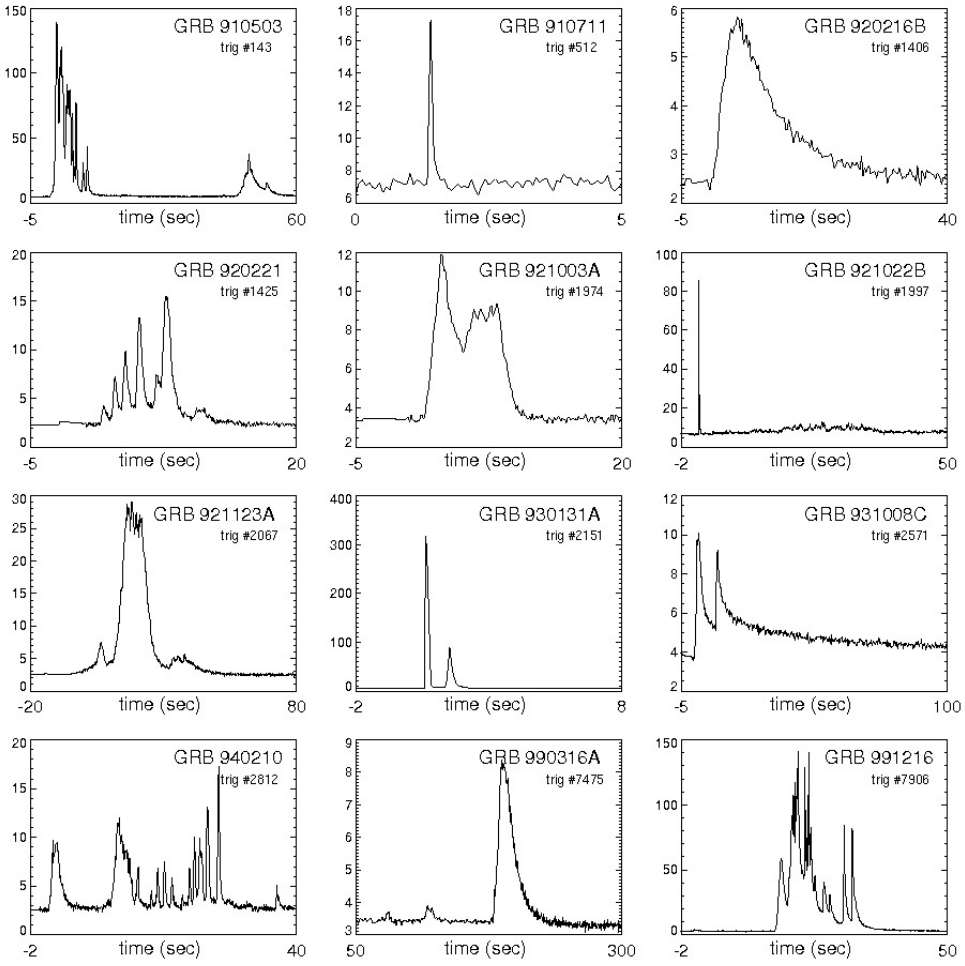

Figure 3.4: Examples of prompt emission light curves of GRBs detected by BATSE. Many different behaviours are seen, ranging from multiple peaks (trig #1425), long lived decays (trig #1406) and precursors (trig #2067). The prompt emission can vary on millisecond time scales. This figure was taken from [131].

Some GRBs are bright enough in order to measure time-resolved spectra. Among the brightest bursts ever recorded is the aforementioned GRB 130427A. Ackermann et al. [130] presented the time-resolved spectra for this burst which also highlights the additional spectral component mentioned already before (see Fig 3.5). Interestingly, this additional power-law component was not present during the peak emission in the keV band, but only afterwards. Additionally, this high-energy component was still present after the prompt emission in the GBM band already faded.

Beyond the initial *prompt* emission phase, a longer lasting *afterglow* emission is often seen in soft X-rays. The instrument bringing the most insight in this phenomenon is *Swift*-XRT

which is sensitive to soft X-rays with energies from 0.2 to 10 keV. Due to it's relatively small field of view, a quite accurate localisation is necessary in order to make a long-term monitoring of the afterglow emission possible. Nousek et al. [132] found that the emission fades as $f(E,t) \propto f(E) \times t^{\alpha_i}$ where i corresponds to the following three stages:

- steep fading with an index α_1 of -3 to -5 of the emission during the prompt phase up to t_1. This phase is thought to be linked to the deceleration of the jet.
- a stage during which the emission stays relatively stable and decays with an index of only $\alpha_2 = -0.5$ to -1 from t_1 to t_2. This is interpreted as emission from larger fractions of the jet opening angle becoming visible.
- a further somewhat steeper fading of the emission after t_2 with an index α_3 that ranges from -1 to -1.5. This is supposedly linked to an adiabatic cooling of the jet material.

The flat stage is typically reached after less than $t_1 = 500\,\mathrm{s}$ while t_2 ranges from $10^3\,\mathrm{s}$ to $10^4\,\mathrm{s}$. These findings were based on the first 27 afterglow observations of *Swift*-XRT.

At high γ-ray energies another aspect which was first seen in EGRET is at play. *Fermi*-LAT confirmed the delayed onset of high-energy emission ($100\,\mathrm{MeV} \leq \mathrm{E}_\gamma \leq 10\,\mathrm{GeV}$) with respect to the emission measured by GBM of up to 40 seconds in the case of long GRBs [124]. At GeV energies, the LATs sensitivity is rather poor at such short timescales so that detections above 10 GeV usually rely on single photons. This renders a measurement of the time structure at these energies extremely difficult.

The duration of GRBs detected by LAT is also interesting to note. In panel (b) of Fig 3.2 the duration measured in the GBM energy range (T_{90}) of LAT detected GRBs does not differ from the larger sample of GRBs. Individual LAT detected bursts did however exhibit long lived emission at GeV energies. GRB 130427A is again among the most unique bursts in this regard with GeV emission lasting 20 hours. In the LAT GRB catalog the duration (T_{90}) of bursts was evaluated in different energy ranges. Significantly longer durations were found in the energy range from 100 MeV to 10 GeV compared to the range of 50 - 300 keV as shown shown in Fig 3.6.

3.3 Radiation Processes in Gamma Ray Bursts

In the previous sections, several observational findings have been collected that have to be reproduced by any successful model description of the GRB emission both spectrally and temporally:

- extreme energy output on short timescales,
- short-term variability during the prompt emission phase,
- band model behaviour in the keV energy range during the prompt emission.
- several GRB detections up to tens of GeV in energy,
- delayed onset of the GeV emission,
- long lasting afterglow emission with characteristic decay.

The prevalent framework in which GRBs are described since the late 90's is the so-called *fireball model* [121]. In this picture, the merger of two neutron stars or the collapse of a

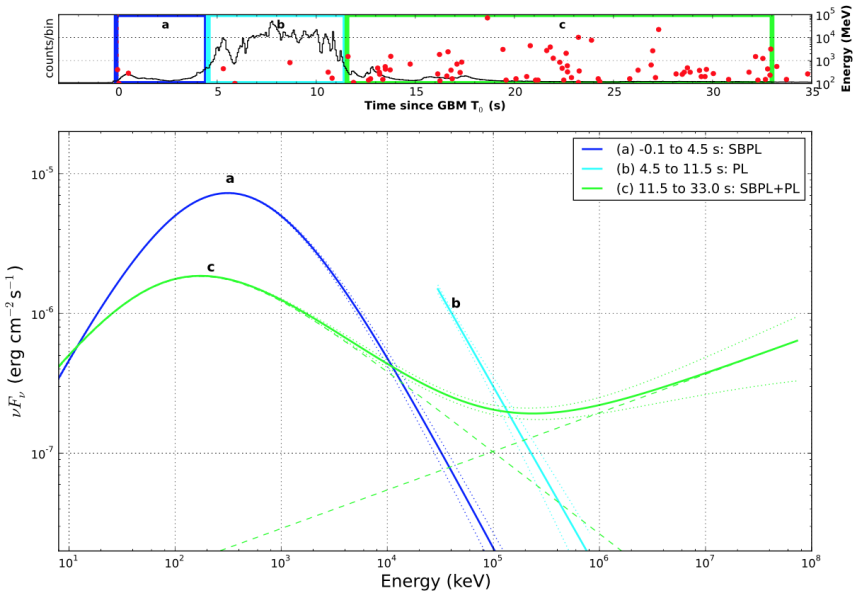

Figure 3.5: Time resolved spectra of GRB 130427A as measured by *Fermi*-GBM and -LAT. The top panel shows the light curve of the burst in the GBM (black line) and in the LAT (red dots indicating individual photons and their energy). The colours indicate the different integration times for the time resolved spectra shown in the bottom panel. This figure was taken from [130].

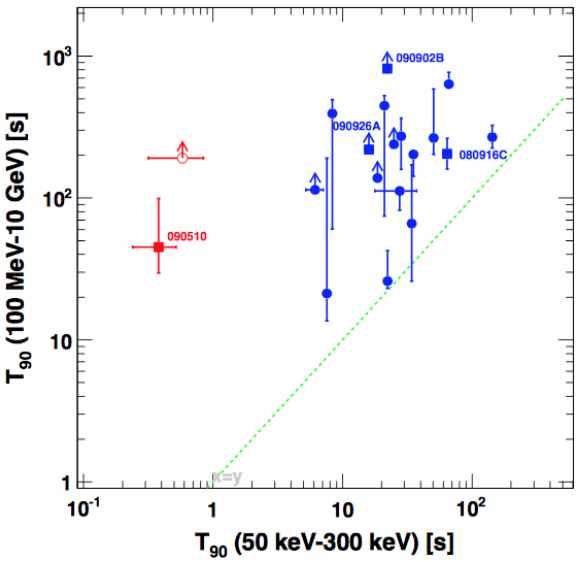

Figure 3.6: This figure shows a comparison of GRBs (T_{90}) duration in different energy bands. The duration of the burst in $E > 100\,\mathrm{MeV}$ is shown on the y-axis in comparison to the duration estimated in the central energy range of GBM (50 - 300 keV). The green dashed line indicates equal durations. The HE emission is found to be systematically longer than the X-ray duration. This figure was taken from [130].

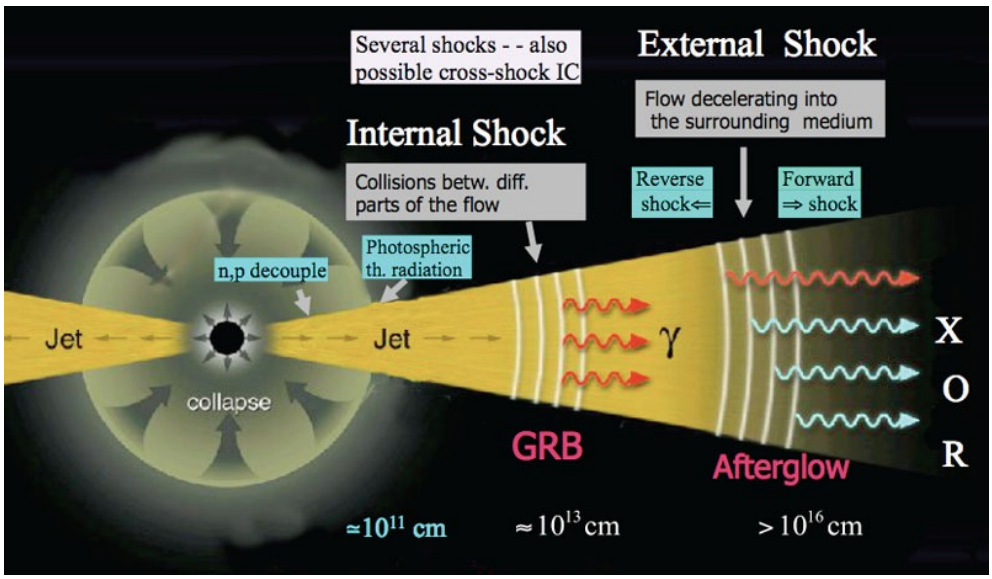

Figure 3.7: Sketch of the many aspects of the fireball model. The central engine is created by a collapse (or a merger which is not displayed here). Several shocks can occur in the collision of plasma shells with different Lorentz factors (Internal Shocks). Another shock front forms where the jet hits the interstellar medium (External shocks). This figure was taken from [131].

massive star creates a 'central engine' that transforms the energy that is freed during the merger/collapse into an ultra-relativistic flow of an electron-photon plasma which might be loaded by a fraction of baryons. The nature of the central engine and the energy transfer mechanisms are however largely unknown. In general, the 'fireball' framework allows for numerous micro-physics contributions which can be fine tuned in order to fit essentially every GRB observation to date.

The prompt radiation is assumed to originate from the collisions of magnetised plasma shells inside the bulk flow. If one assumes a distribution of Lorentz factors for the individual plasma shells they will eventually collide and merge. Particles are co-moving in the individual plasma shells, pre-accelerated by the central engine. The shocks, forming during the collisions of the shells, further accelerate the particles. The accelerated particles radiate due to the magnetic fields, which is giving rise to the bursts of X- and γ-rays. These collisions are typically referred to as 'internal shocks' and are able to explain the variability of the prompt emission on short time scales.

Additionally, a shock is expected at the point of collision of the highly relativistic flow with the interstellar medium, the so-called 'external shock' which is the emission region which is thought to be responsible for the afterglow emission. A sketch of the fire-ball model is depicted in Fig 3.7.

The most important radiation mechanisms which are thought to be at play in GRBs are Synchrotron radiation, Inverse Compton (IC) radiation and the combination of the two – Synchrotron Self Compton (SSC) radiation. Detailed discussions of these processes can be found in [133] and [32]. Here, only a brief introduction to these processes will be given.

Synchrotron Radiation

Charged particles that are accelerated by a magnetic field will radiate. In the non-relativistic regime this is known as cyclotron radiation in which the frequency of the emitted radiation is the gyration frequency. The relativistic counterpart is the Synchrotron radiation. The radiation emitted by electrons in such a situation can be calculated from the relativistic equations of motion from the electromagnetic forces $\mathbf{F}_{\text{Lorentz}} = q\,\mathbf{v} \times \mathbf{B}$ and $\mathbf{F}_{\text{Coulomb}} = q\,\mathbf{E}$ expressed as [133]:

$$\frac{d}{dt}(\gamma m \mathbf{v}) = \frac{q}{c}\,\mathbf{v} \times \mathbf{B} \tag{3.2}$$

$$\frac{d}{dt}(\gamma m c^2) = q\,\mathbf{v} \cdot \mathbf{E} = 0 \tag{3.3}$$

From the last equation it is apparent, that $\gamma =$ constant which allows to modify the first equation to:

$$m\gamma \frac{d\mathbf{v}}{dt} = \frac{q}{c}\,\mathbf{v} \times \mathbf{B} \tag{3.4}$$

By separating the perpendicular and parallel velocities one finds $\frac{d}{dt}v_{\parallel} = 0$ and $\frac{d}{dt}v_{\perp} = \frac{q}{m\gamma c}v_{\perp} \times B$ which describes a uniform circular motion parallel to the magnetic field ($v_{\parallel} = const.$) which is accelerated perpendicular to the field with $a_{\perp} = \omega_{\mathrm{B}} v_{\perp}$ where $\omega_{\mathrm{B}} = \mathrm{qB}/\gamma mc$ is the gyration frequency. The radiated power is given by $P = \frac{2q^2}{3c^3}\gamma^4(a_{\perp}^2 + \gamma^2 a_{\parallel}^2)$ [133]. The total energy loss averaged over all pitch angles results to [32]:

$$\left(-\frac{dE}{dt}\right)_{\text{Sync}} = \frac{4}{3}\sigma_T c \beta^2 \gamma^2 U_{\mathrm{B}} \tag{3.5}$$

Here $\sigma_T = \frac{8\pi}{3}(\alpha_F \frac{\hbar c}{m_e c^2})^2 = 6.65 \times 10^{-25}\,\mathrm{cm}^2$ is the Thomson scattering cross-section with α_F being the fine-structure constant. The central dependency to note is $\gamma^2 U_{\mathrm{B}}$ where $U_{\mathrm{B}} = B^2/2\mu_0$ being the magnetic energy density. The resulting spectrum is a power-law up to a critical energy after which the spectrum decays exponentially [133].

While a single photon gyrating inside a magnetic field emits a spectrum of photons, it is useful to approximate, that electrons with energy E emit photons at a fixed frequency $\nu = \nu_{\max} = 1.9\left(\frac{E}{100\,\mathrm{TeV}}\right)^2\left(\frac{B}{1\,\mathrm{nT}}\right)\mathrm{keV}$ which corresponds to the peak frequency of the synchrotron spectrum emitted by the electron in a magnetic field with a strength B. This allows for the use of the following relations [32]:

$$\nu \propto E^2 B \longleftrightarrow E \propto \nu^{1/2} B^{-1/2} \longrightarrow dE \propto \nu^{-1/2} B^{-1/2} d\nu \tag{3.6}$$

Taking now an electron distribution $N(E)\mathrm{d}E = KE^{-p}\mathrm{d}E$, the energy flux per frequency ν can be calculated to

$$J(\nu)d\nu = -\frac{dE}{dt} \times N(E)dE \;\propto\; \sigma_T U_B\, E^2 K E^{-p} \nu^{-1/2} B^{-1/2} d\nu \;\propto\; B^{(p+1)/2}\nu^{(1-p)/2} \tag{3.7}$$

yielding a differential energy flux index $s = (p-1)/2$ which translates into a differential photon index of $\alpha = s + 1 = (p+1)/2$. This result holds in the central region of the energy distribution of the electrons. Cutoffs in the electrons energy distribution are somewhat smoothed out by the spectrum emitted by each individual electron. Still, such a break would

leave their traces by altering the resulting photon spectrum at the synchrotron frequency corresponding to the electron break energy. Sufficient photon statistics would allow for the characterisation of such a break.

Two extreme scenarios of synchrotron emission can be considered. First, the case in which electrons loose all their energy instantaneously through synchrotron radiation. The synchrotron prediction in this case gives spectral indices of $\alpha < -2/3$. In the second extreme scenario, electrons are allowed to cool on timescales much shorter than the burst time. This leads to a prediction of $\alpha > -3/2$ [134]. The latter limit being not so strict as self-absorption can further soften the synchrotron spectrum. Both limits are independent of the spectral shape of the electron distribution.

Inverse Compton Scattering

Inverse Compton scattering is, as the name suggests, the reverse process of Compton Scattering. In Compton scattering, a photon transfers energy to an electron with lower energy. In Inverse Compton scattering this is reversed: An electron transfers energy to a lower-energy photon. The cross-section for the scattering depends on the centre of mass energy of the collision of the photon and electron which can be expressed (unitless) as $x = E_\gamma E_e/(m_e c^2)^2$. The case $x \ll 1$, corresponds to the Thomson regime and the cross-section of the Inverse Compton scattering is proportional to the elastic Thomson scattering cross-section σ_T.

The energy loss electrons experience due to Inverse Compton scattering in the Thomson regime is given by [32]:

$$\left(-\frac{dE}{dt}\right)_{IC} = \frac{4}{3}\gamma_e^2 \sigma_T c U_{rad} \tag{3.8}$$

The proportionality to γ^2, seen previously in synchrotron radiation, is found again. In this case it is coupled to the energy density in the radiation fields U_{rad}. Therefore the same argumentation for the resulting spectrum given in the case of Synchrotron radiation applies.

Values of x in the order of unity or larger correspond to the Klein-Nishima regime in which the scattering no longer remains elastical. In this regime the cross-section can be approximated to $\sigma_{KN} = \frac{3}{8}\frac{1}{x}(ln(2x)+\frac{1}{2})\sigma_T$ [133], decreasing with centre of mass energy as $1/x$ in the relativistic regime. This leads to lower scattering rates with larger amount of energy radiated per scattering. Taking the squared centre of mass energy $b = 4E_\gamma E_e/(m_e c^2)^2$, the maximum energy gain per scattering can be expressed as $\frac{b}{b+1}E_e$ which corresponds to the total energy of the electron for large values of b. In the Klein-Nishima regime the radiated spectrum is therefore directly linked to the spectrum of the electrons as they loose almost all their energy in a single scattering [32].

Application to GRBs

These two processes are of great importance in the case of GRBs. Their contribution is balanced by the the ratio of energy densities in the emission zone. The ratio of the Inverse Compton and Synchrotron energy loss as given by [32]

$$\eta = \frac{(dE/dt)_{IC}}{(dE/dt)_{Sync}} = \frac{U_{rad}}{U_{mag}} = \frac{U_{rad}}{B^2/2\mu_0} \tag{3.9}$$

As discussed in section 3.1, the photon energy density is quite high in GRBs. Therefore it is not unreasonable to assume that η can be larger than 1. In this case Synchrotron Self-Compton radiation becomes possible: The relativistic electrons perform Inverse Compton

scattering with the photons produced through Synchrotron radiation. The same electrons which are giving rise to the Synchrotron radiation in the first place.

In the case of relativistic electrons with bulk Lorentz factors of $\gamma = 100 - 1000$, as possible in GRBs, the synchrotron photons already extend into the keV energy range. These can be up-scattered by a factor of γ^2, which corresponds to values of $10^4 - 10^5$. The Synchrotron Self Compton radiation produced in such scenarios extends well into the GeV, and potentially even into the TeV energy range.

As demonstrated in section 3.1, the keV to MeV energy range is the best studied energy range of GRBs. The Synchrotron radiation yields concrete predictions for the spectral slope of the emission. Fast cooling is necessary in order to allow for the small timescale variability observed in GRBs [135]. This corresponds to the Thompson regime as scattering is inefficient in the Klein-Nishima regime. Taking the description given above, a spectral index of $\alpha = -(p+1)/2$ is expected from an electron distribution with a spectral slope of $-p$. A canonical index of $p = 2$ is reasonable in the case of electrons being accelerated by shocks. This yields a photon index of $\alpha = -3/2$ and sits well within the observed slopes as displayed in Fig 3.2.

The limits to the predicted synchrotron spectral index values of $-2/3 > \alpha > -3/2$ are however violated in numerous cases. These deviations are being addressed in many different forms, ranging from long timescales on which particles are preheated before the burst [136], changes in the pitch-angle distribution of electrons [137] or with adjustments to the small scale structure of the magnetic fields [138, 139]. Or by entirely new contributions to the spectrum in addition to synchrotron radiation such as photospheric components [140].

In order to explain the observed short-term variability Bošnjak and Daigne [141] show, that fine-tuning of the Lorentz factor distribution of the plasma shells in the fireballs internal shock framework allows to reproduce the exact short-term variability seen during the prompt emission phase on a case by case basis.

3.4 Gamma Ray Burst Progenitors and Classes

The current paradigm favours two scenarios for the progenitor of GRBs. The short GRBs with durations of less than 2 seconds are thought to originate from the merging of two compact objects where one of the two should be a neutron star. GW/GRB170817 [52] is the first definitive observational evidence that such short bursts are indeed linked to neutron star mergers [142].

Bumps in the optical light curves have been seen in several long GRB afterglow observations. Optical spectroscopy is often able to determine the origin of this bump as that of a core-collapse supernova [143]. On the other hand not all long GRBs with confirmed optical counterparts show the existence of supernovae. The majority of core-collapse supernovae are observed without a GRB. The specific properties of the progenitor, e.g. the rotation and mass, of the massive star are believed to be the deciding factors in order to understand whether a GRB is produced trough the supernova. Such constraints ask for stellar candidates that feature extreme values of mass and rotation. Shenar et al. [144] studied emission lines of local (meaning in our galaxy as well as in the LMC) Wolf Rayet (WR) stars in a model in which the stellar rotation is accounted for. They found the emission lines to be best described with high rotation velocities in the order of $2000 - 3000\,\mathrm{km/h}$ for the test WR stars with masses in the order of $20 - 30\,M_\odot$ while demanding strong magnetic fields: all indicators outlined as mandatory for long GRB progenitors. If such parameters are al-

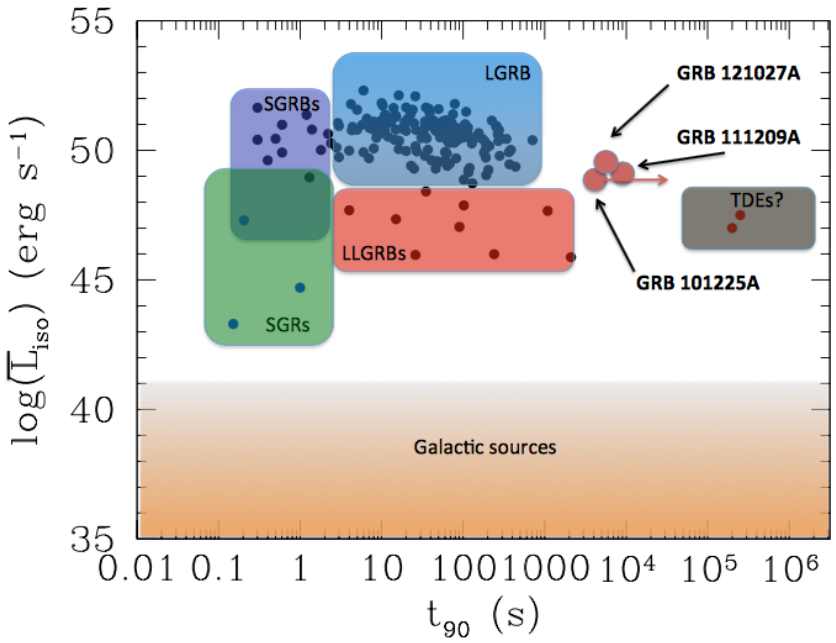

Figure 3.8: The phase space of transients in isotropic equivalent luminosity as a function of the duration of the transient. different classes of GRBs are highlighted as well as other transients such as Soft Gamma Repeaters (SGRs) and Tidal Disruption Events (TDEs). The samples of detected Low-Luminosity GRBs (LL-GRBs) and Ultra-Long GRBs (UL-GRBs, indicated by the three red markers) seem to be detected less often than the classic short and long GRBs. This figure was taken from [145].

ready feasible in our direct neighbourhood, more extreme stars are to be expected in distant galaxies.

The classical phenomenological view of GRBs is starting to break down as the diversity of GRB sub-populations is growing well beyond the *short* and *long* classes. With more and more astrophysical counterparts being identified, a paradigm shift from the generic GRB term towards actual astrophysical progenitors seems to be starting. multi-wavelength observations play a crucial role in this development by e.g. searching for supernovae associations more efficiently. More insight in the astrophysical nature of GRBs is expected to be brought about by more detections at γ-ray energies above 1 GeV and by extending the multi-wavelength observations into Multi-messenger observations with the addition of Neutrino and Gravitational Wave observations. Three classes which are predominantly discussed in the Multi-messenger GRB community are Low Luminosity GRBs (LL-GRBs), Ultra Long GRBs (UL-GRBs) as well as the so called Kilonovae. All three classes present difficulties for current X-ray detectors. In these cases observations of other wavelengths or messengers might play a crucial role in unraveling the nature of transient bursts of γ-rays.

Ultra Long GRBs

Levan et al. [145] reported about the three GRBs with durations of several thousand seconds (see Fig 3.8). They determined that all three are very similar in terms of the X-ray light-curve and UV emission. All three were located in the cores of compact but active star forming

galaxies. Such long timescales pose severe challenges with respect to the requirements on the central engine activity and thus to the progenitor scenario. In their paper Levan et al. [145] discuss Population III stars while Zhang et al. [146] consider the long-lasting fall-back accretion from Blue Super Giants as progenitors for these UL-GRBs.

Detection-wise, such long timescales pose difficulties for the standard approach as exposures are exceeding the maximum time the position can be observed in a single orbit of the spacecraft. As such long exposures are rarely possible, the true rate of UL-GRBs might be much higher than the actual detected rate suggests [145].

Low Luminosity GRBs

LL-GRBs are a sub-class of *long* GRBs and exhibit low isotropic equivalent luminosity of typically $10^{46} - 10^{48}$ erg with a smooth single pulse light curve in the prompt emission (see Fig 3.8). The low luminosity allows for detections only at low redshifts ($z < 0.1$). With four detected LL-GRBs the event rate is of the order of $230\,\mathrm{Gpc}^{-3}\,\mathrm{yr}^{-1}$ which is $100 - 1000$ times higher than the rate of long GRBs pointing toward Earth. The leading explanation makes use of the reduced luminosity and variability constraints which results in smaller boosting and larger opening angles [147].

LL-GRBs are of special interest for the neutrino community. The stacking analysis of all GRBs reported in Abbasi et al. [148], Aartsen et al. [107] determined that less than 1 % of the astrophysical neutrino flux originates from such classical GRBs [149, 150]. Therefore GRB scenarios in denser environments are being put forward [151, and references therein]. In these scenarios the GRB jet is choked and stopped within the extended material. Due to the missing or weak jet, such GRBs might be missed by the current generation of X-ray missions. Whether GeV to TeV γ-ray emission is produced is not clear. Waxman et al. [152] argue that one of the LL-GRBs, namely GRB 060218, was a case in which the GRB jet barely escaped from the dense environment. Similarly Wang et al. [153] discussed potential non-thermal photon components.

Realtime detections of neutrinos might be a probe for such LL-GRBs which can be used in order to perform follow-up observations even though these phenomena might be missed in X-rays. In order to efficiently produce neutrinos, a sufficient amount of baryons needs to be available in the emission zone. Such enhanced baryonic loading can be feasible if the environment of the emission is dense.

Gravitational Waves and Kilonovae

The 'kilonova' (or 'macronova') phenomenon was first discussed in 1998 by Li and Paczyński [154]. It is thought to be an electromagnetic counterpart to the merger of either a Black Hole with a Neutron star (BH-NS) or a merger of two NSs (NS-NS). Therefore the kilonova is another counterpart to the previously discussed short GRBs. During the merging process, a relatively small fraction of matter of $\approx 10^{-2}\,M_{\odot}$, is ejected with mildly relativistic velocities in the order of $0.2\,c$. [155]. The ejected material is thought to be neutron rich which leads to a rapid neutron capture (r-process) which heats the ejected material.

In contrast to short GRBs, the kilonova is approximately isotropic [155] and can therefore be a useful probe for GRBs with jets that are not directed towards Earth. The mostly thermal kilonova can therefore be a useful proxy to perform observations of GRBs which are typically not or only faintly detected by X-ray spacecrafts due to large viewing angles with respect to the GRB jet axis. BH-NS and NS-NS mergers are strong sources of gravitational

waves [155]. Counterparts in all wavelengths might be discovered without a detection from X-ray detectors, triggered by the detection of Gravitational Waves consistent with such merger events.

GW170817 [53] is one example of this. While this NS-NS merger event happened not too distant from earth, only a faint GRB has been detected by GBM [156]. The subsequent multi-wavelength follow-up [157] determined that the broad-band emission is consistent with a kilonova [158].

As the sensitivity of the existing Gravitational wave observatories improves, Gravitational Waves will play an important role for all observatories in order to perform follow-up observations of many different kinds of extreme phenomena beyond GRBs, also for IACTs.

3.5 Gamma Ray Bursts in the TeV γ-Ray Domain

The prospects to observe γ-rays with the IACT method from GRB-like phenomena is generally considered to be a question of time until the first detection happens. Rich scientific rewards are expected. As presented in section 3.2 *Fermi*-LAT has already shown that γ-rays with energies in the order of 100 GeV are emitted in a fraction of GRBs [130, see GRB130427A] which is well in reach for the current generation of IACTs already. Ground-based observations of GRBs like the ones detected by *Fermi*-LAT in the multi-GeV energy range would result in tremendous photon statistics. By comparing the sensitivities of *Fermi*-LAT and e.g. H.E.S.S. (see Fig. 1.8) one would expect in the order of 10000 photons where *Fermi*-LAT only detected one. This would allow for:

- precise measurements of the delay between X-ray and γ-ray emission
- precise measurements of the spectral cutoff either due to intrinsic particle acceleration, emission processes or absorption effects
- estimates on the ratio of the energy in magnetic fields and in particles.

The lack of a detection to date however is not to be forgotten in the interpretation of results from a hoped for first detection. The spectral and temporal variety in X-rays alone outlined before as well as the changes in the observed HE γ-ray behaviour will raise one central issue: how are general GRB properties going to be extracted from a single or a few detection at energies beyond HE γ-rays while a huge number of follow-up observations yielded non-detections. What kind of a sub-population of GRBs will this be? Therefore one has to expect that a first detection will likely not reveal general properties that apply to all GRB classes. Several challenges and difficulties apply in the VHE-γ-ray domain which will be discussed in the following.

Extragalactic Background Light constraints

Photons traveling through interstellar space can perform γ-γ interactions with the history of all light emitted, known as the Extragalactic Background Light (EBL). The EBL photons which affect a γ-ray with energy E_γ the most has an energy of $E_{\mathrm{EBL}} = 4m_e^2c^4E_\gamma^{-1}$ [159]. For γ-rays with energies in the order of TeV, this lies in the eV (optical light) range. The attenuation modifies the observed γ-ray spectrum with an exponential cutoff $e^{-\tau}$. Fig 3.9 shows different attenuation levels τ as a function of redshift and γ-ray energy. This indicates the redshift horizon for VHE γ-rays. γ-ray emission in the 100 GeV energy range from a

distance of $z = 1$ is already attenuated by a factor of $1/e$. Going to larger redshifts requires data with lower energy thresholds which are only possible in low zenith-angle observations, effectively reducing the phase space for such observations. Detections under such conditions with good photon statistics would present the opportunity to independently measure the EBL. For this, a larger sample of sources at many different redshifts would be required. With no IACT detection to date, this is a study one can only wish to carry out in the future. Furthermore, one should note that EBL attenuation of course affects all extragalactic sources, not only GRBs and other distant transients.

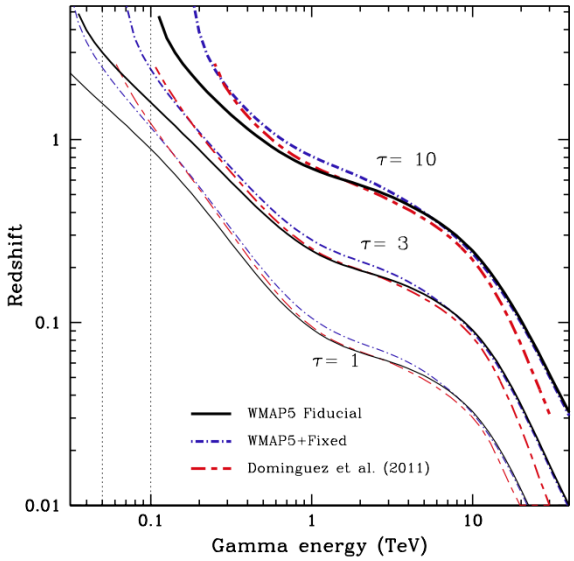

Figure 3.9: Different EBL attenuation levels as a function of redshift and γ-ray energy. The redshift horizon for attenuations of $\tau = 1$ is at redshifts of $z \approx 2$ for 50 GeV γ-rays. This figure taken from [159].

The distribution of distances at which GRBs occur is not known well. Out of the $\sim$ 3000 GRBs, the redshift is only known for approximately 10 % of them (or 30 % of the *Swift* detected bursts). One trend that is visible however is, that short GRBs are typically occurring closer than long GRBs. The redshift distribution for GRBs for which a counterpart with redshift measurement was able to be identified was found to peak at around 2.2 [114]. Additionally the GRB redshift distribution resembles the star formation history of the universe [160] which implies GRBs getting rarer at redshifts $z > 2.5$.

One major question therefore is: Is the small fraction of GRB detections at multi-GeV energies due to the EBL, or due to the particle acceleration processes and effects of the GRB environment or due to the rarity of the HE-γ-ray emitting GRB class? As *Fermi*-LAT has a substantial sensitivity at energies around a few hundred MeV too (at which the EBL attenuation is negligible), one has to expect that the EBL is not the main constraining factor for GRB detections at VHE energies currently.

Today, optical facilities no longer follow-up on every GRB detection in order to estimate the redshift. This poses a problem as any detection made at TeV energies might be lacking an accurate distance measurement. This complicates drawing conclusions from the detection. In any case, redshift estimates become available usually with a delay of several hours. At this stage, H.E.S.S. observations have likely concluded due to the geographic offset between

Namibia and Chile, where most of the optical facilities which are able to access the Southern sky are located.

Repointing speed constraints

Another factor limiting the potential to observe GRBs with IACTs is the timescale of the emission. If the high-energy γ-rays are emitted simultaneously with X-rays, a very fast repointing procedure is necessary to start the observations during the prompt phase. In fact the short GRBs might be out of reach with a repointing approach since the detection and circulation of the burst information usually takes longer than the prompt emission phase itself. Based on the *Fermi*-LAT results, the time structure of the high-energy γ-ray emission is different compared to X-rays. A common HE γ-ray temporal evolution model is however not yet determined. In addition to the delayed onset in GeV γ-rays, the GeV emission lasts systematically longer than in X-rays with afterglows lasting up to 20 hours. Follow-up observations with IACTs should therefore try to cover both the simultaneous time range of the X-ray detections of the GRB as well as longer timescales in order to cover all viable timescales on which emission could be expected.

The current generation IACTs already achieved remarkable repointing times of less than 30 seconds in some cases. One could argue that the repointing constraint is not as severe as commonly pointed out. However one should note that the major fraction of reported GRB follow-up observations still starts with delays of more than 100 seconds, often into the multiple hour range, due to the duty cycle constraints of IACTs. The two factors to consider are: i) The technical possibility to react very quickly to GRB detections while ii) keeping a large enough phase space for follow-up observations in terms of observation conditions. One could argue for the reduction of the GRB follow-up observations to the most promising candidates. These would be the LAT detected bursts with confirmed GeV emission. Such constraints would essentially result in only a few observations over the course of a decade at best.

3.6 Conclusions

While GRBs are among the oldest transient phenomena in the high-energy sky, we still know very little about the actual processes giving rise to these intense bursts. In the recent years the paradigm of explaining all GRBs in the common fireball model framework slowly starts to change. More and more GRBs can be connected to astrophysical counterparts which allowed for building sub-classes of GRBs and an increased discussion of microphysics affecting the measured GRB spectra.

Current emission models still manage to predict γ-rays beyond the GeV energy range. Neutrinos and Gravitational waves present new interesting messengers which might be able to shed more light on the origin of GRBs or distinguish even more sub-classes. Therefore, all possible astrophysical messengers should be taken into consideration for the planning of follow-up observations with IACTs. This includes Gravitational Waves and Neutrinos as messengers for potential GRB-like phenomena beyond classical GRBs.

Historically every additional observation of GRBs in other wave-bands yielded interesting constraints on models and correlation to astrophysical phenomena: The now quite clear correlation of some GRBs with supernovae was only possible through the successful optical follow-up of GRBs. Likewise the HE γ-ray observations by *Fermi*-LAT seem to break the

decade of band-model descriptions of GRB spectra by revealing additional spectral and temporal features.

More such breakthroughs are possible in the future with more successful follow-ups in other wavebands and messengers. The importance of the addition of Gravitational Waves to GRB observations was impressively demonstrated by GW 170817, the first observation of a NS-NS merger in electromagnetic radiation as well as with Gravitational Waves, which will be discussed in more detail later.

The scientific reward of a GRB detection at γ-ray energies with IACTs is certainly not to be underrated. The most extreme GRBs detected by *Fermi*-LAT suggest that such a detection should be in reach already today. The fact that not a single GRB was detected over the course of more than 10 years of operation of the current generation IACTs however should not be neglected. The first IACT detection of a GRB will have to judged in the light of all previous non-detection, making this anticipated burst a quite unique one.

The trend is clearly pointing towards an emphasis on multi-wavelength and messenger astrophysics approach. IACTs will take part in this development providing the picture in VHE γ-rays to many astrophysical transient phenomena beyond GRBs.

Ways to improve observations of transients in the VHE γ-ray domain are: i) Repoint faster to cover all timescales of emission; ii) Improved energy thresholds are necessary in order to extend the EBL horizon; iii) Information from all available messengers should be combined to improve the chances for detections of multi-messenger transients in the future.

H.E.S.S. has addressed ii) with the addition of CT5 to the array in 2012. The challenges behind, and current solutions of i) and iii) will be addressed in the following chapter in more detail.

Chapter 4

Observing Transients with H.E.S.S.

As seen in the previous chapter, the TeV energy regime of GRB related phenomena is largely unexplored. Several improvements to the observation strategy were identified which would increase the chances for detections in VHE γ-rays. For H.E.S.S. these points are: i) Exploit the lower-energy threshold of the large Cherenkov Telescope CT5 in order to increase the Extragalactic Background light horizon, ii) Observe on various timescales from prompt follow-up to multiple hours in order to probe all potential timescales of emission and iii) incorporate as many wavelengths and messengers into the follow-up programs as possible in order to increase the coverage of GRB-like phenomena and triggering channels.

The considerations outlined in the previous chapter apply to essentially any other transient event too. Therefore, the identified points for improvement are general requirements for a successful era of multi-messenger transients observations with H.E.S.S.

This chapter will highlight how H.E.S.S. is participating in the field of transient astronomy. Transient astronomy is largely driven by the capabilities of survey experiments which still present severe constraints on how i)-iii) can be addressed with pointed observations. Therefore an overview of todays landscape of high-energy related transient astronomy instruments with a brief outlook for the coming decade will be given in section 4.1.

The time allocation between observations of transients and stable sources with H.E.S.S is a balance between the different science interests of the collaboration. H.E.S.S. tries to optimise this balance and works out observation programs. For transients, this includes defining trigger criteria for all phenomena and hypotheses that are being probed. Section 4.2 will summarise the short-timescale transient follow-up programs H.E.S.S is currently running.

The execution of transients follow-up observations is carried out by the H.E.S.S. transients alert system which was developed as part of this work. The system has to reflect the observation programs which are defined by the collaboration. The systems functionality covers: reacting to incoming transients alerts and evaluating all defined trigger criteria, determining a follow-up strategy, autonomous communication with the components that steer the telescopes and monitor the data in real-time. Details of the transient alert system will be described in section 4.3. The systems performance will be discussed in section 4.4.

4.1 The Landscape of Transients Astronomy Instruments

Communication of detected transients

While the requirements given above may seem straight forward, several aspects complicate the execution of them. One central aspect is the fact that typically not all information on transient detections is available instantaneously.

The idea to publicly share the coordinates of transient phenomena has been established due to a hardware failure of BATSE (Burst and Transients Source Experiment) on board the Compton Gamma-Ray Observatory (CGRO). The on-bard tape recorders had failed which meant that the data had to be transmitted to the ground in real-time in order not to lose the data forever. The system that was setup in an effort by NASA was called BACODINE (BATSE coordinates distribution network) and was developed within only a few months, starting operating in May 1993. Since then, most new space-based experiments with transient detection capabilities also share coordinates of detections through this system which lead to a name-change to GCN (Gamma-ray burst Coordinates Network) [161]. This practice has proven to open new frontiers in the study of GRBs by enabling follow-up observations of GRBs which enabled a first distance measurement in 1998 [162]. GCN is still operating today and distributes coordinates of transients detections from many experiments. Due to the large number of contributing experiments the GCN is still among the largest sources of public alerts on transient detections. The modes of communication of such localisations evolved from E-Mails and pager notifications to machine readable binary packets that are transferred over a socket connection. In order to perform automated reactions to alerts, only the socket based connection is a viable option.

Another service, that acts as a hub of alerts from a variety of experiments is 4πSky [163]. They distribute transients localisations from GAIA [164], LOFAR [165, 166] and ASASSN [167]. With these alerts from experiments that measure in the optical and radio wavelengths, the combination of both GCN and 4πSky results in a diverse set of transient science accessible in addition to the different GRB scenarios discussed in chapter 3.

Both GCN and 4πSky are services which publish results in near real time and machine readable format. More detailed information is often shared on longer timescales with humans in the loop. GCN features the so-called *Circulars* which present preliminary results that were obtained from more sophisticated analyses of observations reported in previous alerts. In the case of GRBs such information can be spectral information but also retractions of alerts due to false triggers. Circulars are typically available a few hours after the initial alert. Also other astronomers can respond to alerts with e.g. redshift measurements or non-detection announcements.

Another traditional form of communicating transients which presents rather robust results with physics conclusions on longer timescales are Astronomers Telegrams (ATels) [168]. ATels cover essentially all transient phenomena, even information on comets has been published as ATels. Information given in ATels is available only in a human readable form and is useful in order to judge if a follow-up campaign should be continued in the long run.

Experiments in transient astronomy

Two main categories of instruments can be identified: Instruments with a large field of view which are able to cover large portions of the sky with a high cadence, making them *survey* instruments. The other category are small field of view instruments which are able to perform detailed measurements with better sensitivity and resolution compared to survey instruments. The small field of view of these make them *pointing* instruments. Both classes are in a synergetic relation. Interesting phenomena are first identified by survey instruments which are then followed and classified by pointed instruments. This philosophy is what brought many breakthroughs in GRB observations (e.g. association of supernovae with GRBs or determining the extragalactic origin of GRBs with cosmological distances).

The wide range of instruments providing information in the high-energy domain are not only different with respect to the messengers or energy ranges that they cover. They also have a varying focus on the following aspects:

- coverage in energy
- localisation precision
- duty cycle
- repointing capabilities
- sky coverage
- sensitivity on small time scales

Improved performance in one of these domains usually comes at the cost of reduced performance in another. KONUS-WIND for instance provides light curves and spectra of high temporal accuracy and broad energy coverage of transients but can't reconstruct a localisation of the transient on their own [169]. The most important aspects for an incomplete list of instruments that actively participate in time domain high-energy astronomy are summarised in Table 4.1. Instruments like *Swift* implement both pointing and survey type instruments on a single spacecraft. *Swift*-BAT scans large fractions of the sky for transients and alerts *Swift*-XRT and *Swift*-UVOT to repoint towards the transient.

IACTs fall in the pointing instrument class and rely on transient triggers from survey experiments. *Fermi*-GBM is very efficiently detecting GRBs with a high duty cycle and a large field of view, the localisation uncertainty is typically not better than a region with a 3 deg radius due to systematic effects. This is larger than the field of view of H.E.S.S. and nicely exemplifies one of the challenges within the synergetic relation of survey and pointed observations. The mismatch between the localisation uncertainty and the field of view ultimately requires H.E.S.S. to either scan large regions with multiple pointings or to focus the exposure on the most probable sky region.

Experiments for transient astronomy with H.E.S.S.

Experiment		Messengers	Phenomena	Energy range	localisation precision	sky coverage	detection sensitivity	References
Fermi	-GBM	X-rays	GRBs	10 - 1000 keV	3 deg	50 % full sky duty cycle	$0.5\,\mathrm{ph\,cm^{-2}\,s^{-1}}$	[11]
	-LAT	γ-rays	GRBs	30 MeV - 300 GeV	0.17 - 2 deg	2.4 sr Field of view	$4 \times 10^{-5}\,\mathrm{ph\,cm^{-2}\,s^{-1}}$ for 30 s	[10]
Swift	-BAT	X-rays	GRBs	15 - 150 keV	0.3 deg	1.4 sr Field of view	$10^{-8}\,\mathrm{erg\,cm^{-2}}\,s^{-1}$	[170]
	-XRT	X-rays	GRBs	0.2 - 10 keV	0.004 deg	$23.6 \times 23.6\mathrm{arcmin}^2$	$10^{-13}\,\mathrm{erg\,cm^{-2}}\,s^{-1}$ in 1000 s	[171]
	-UVOT	optical	GRBs	170 - 650 nm	0.0007 deg	12 arcsec aperture	down to 22.3 Mag within 1000 s	[172]
IceCube		ν	Unknown	300 TeV - 1 EeV	1.5 deg	99 % duty cycle with varying sensitivity	few events per year (see reference)	[173]
Antares		ν	Unknown	10 TeV - 50 PeV(?)	0.5 deg	99 % duty cycle with varying sensitivity	few events per year (see reference)	[174]
LVC		GW	from BBH to NNS mergers	-	30 - 600 deg^2	full sky duty cycle depends on maintenance campaigns	$\sim 1 - 20$ events per year	[175]
H.E.S.S.		γ-rays		20 GeV - 20 TeV	0.008 deg	2×2 deg	see section 1.4	see section 1.4

Table 4.1: Summary of key features of the experiments involved in the H.E.S.S. transient follow-up programs. Detections of transients from the sub-detectors GBM and BAT from *Fermi* and *Swift* allow for a repositioning of the spacecraft in order to perform follow-up observations with the other sub-detectors on board the spacecraft. The two neutrino telescopes IceCube and Antares are more sensitive towards the Northern and Southern hemisphere respectively due to their location. The different detector layouts lead to different energy scales which are being probed. LVC is the consortium of LIGO and Virgo, which correlate their measurements in near real-time for improved precision. H.E.S.S. is given as one example of IACTs here. MAGIC and VERITAS are similar with respect to their performance. Follow the given references for more detailed information.

Future missions

A large variety of missions with strong transients science programs are in the process of either being under construction or advanced planning. A timeline for all major planned missions in all wavebands and messengers are shown in Fig 4.1 [104]. Missions are going online within the next decade in essentially all wavelengths.

The amount of planned missions underlines the shifting paradigm outlined in the previous chapter: Essentially all future missions aim to build on the synergies between wavelengths and messengers. This development poses strong requirements on the transients science community with respect to the technical systems that are being used for the distribution of alerts, as well as on the political traditions of sparse exchange of information between experiments (which applies most importantly to the TeV γ-ray community).

The largest scientific overlap with Cherenkov Telescopes is expected from SKA [102] in radio, LSST [176] in optical and SVOM [177] in X-rays. Pathfinder projects of SKA such as ASKAP [178] are already detecting many Fast Radio Bursts (FRBs) [179] during their currently limited operation time.

With respect to GRB science, SVOM is going to outperform *Swift* significantly in many regards. The SVOM mission involves a network of optical ground based telescopes to determine the redshift for large fractions of GRBs detected by the X-ray satellite.

LSST will be a potent partner experiment for SVOM with a large field of view and many prospects for transients. First studies have shown that LSST will detect up to one million variable objects each night. Phenomena LSST will probe range from common variable stars, over GRB afterglows to rare tidal disruption events.

These large infrastructures will truly change the current landscape of transient astronomy. A viable strategy to communicate and handle scientific alerts of transients in an efficient way is a major challenge in the whole multi-wavelength community which has to be solved in order to make the best use of all the great data that is expected to be taken.

The Cherenkov Telescope Array (CTA) will be the predecessor of MAGIC, VERITAS and H.E.S.S. Exploring different or new techniques of inter-infrastructure communication is therefore valuable input to the design of CTA and the science cases that are currently being built for transients [104].

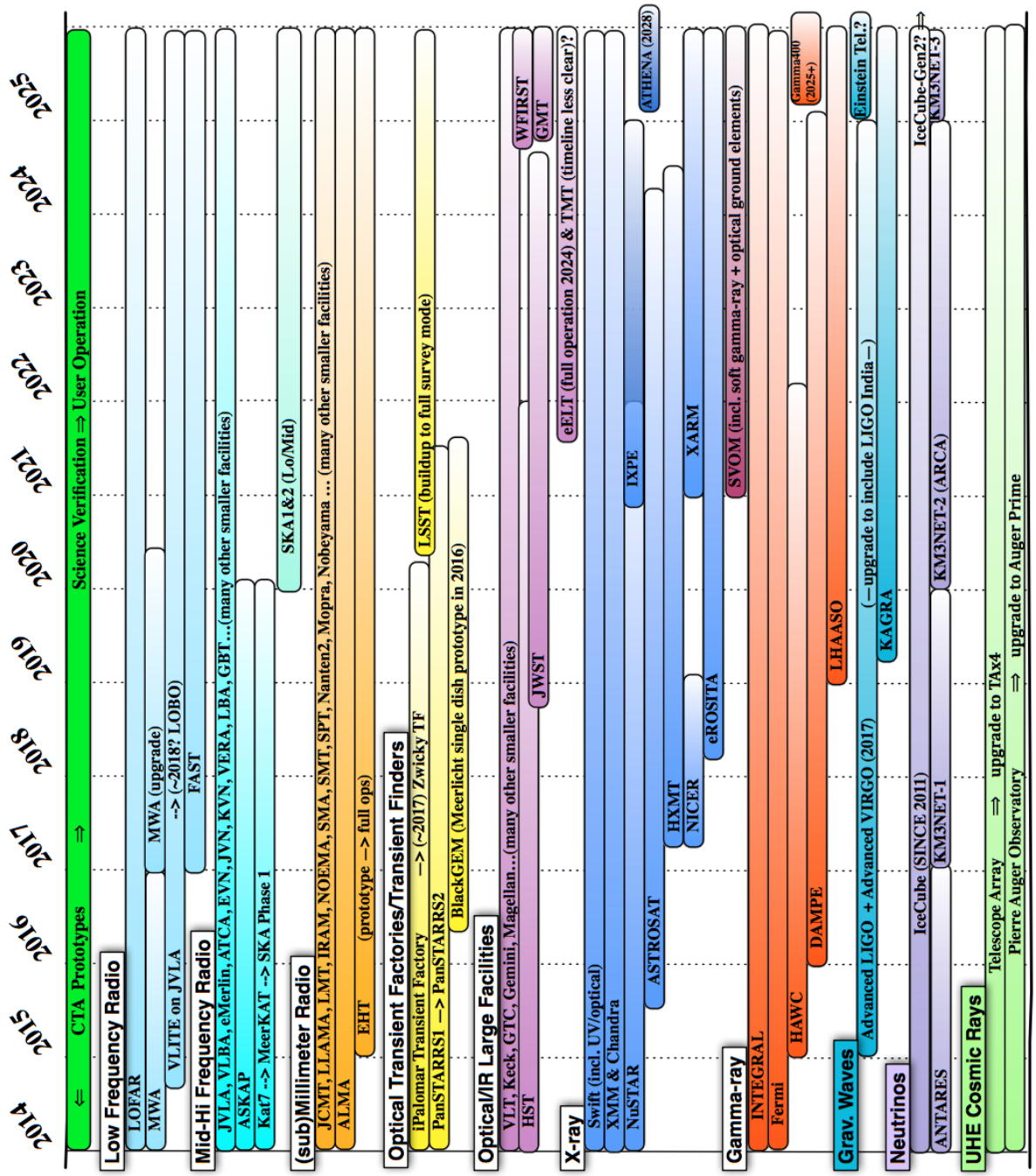

Figure 4.1: Tentative timeline for current and next generation facilities with transients and MWL programs for the next decade. The facilities are grouped according to their energy range and messenger, starting with low-energy wavelengths on the top of the figure, ranging to higher energies up to γ-rays. Gravitational Waves and cosmic particles like neutrinos and ultra-high-energy cosmic rays conclude the figure. This figure was taken from [104].

4.2 H.E.S.S. Transients Follow-up Programs

Observation strategies and programs should always be driven by the science potential. For transients however, another important factor needs to be taken into account. The phase space of transient phenomena that one wants to probe has to be evaluated with regards to the timing and content of information that is being provided by survey instruments.

While the observation of stable sources can be planned based on their coordinates long in advance, the observation of transients requires clear trigger conditions and observation strategies. The trigger conditions have to be balanced such, that a suitable number of triggers of high enough relevance results while not overshadowing the planned observations of stable sources by too much. The limited knowledge about a transient at the time of its detection further complicates this.

In this section, an overview of the transient observation programs which rely on rapid repointing will be given. The focus will be on the observation programs based on GRB, neutrino and gravitational wave triggers. The execution of these programs is heavily based on the technical system which implements all presented criteria and issues the observations.

The GRB follow-up program

H.E.S.S. follows up on GRB detections since its start of operation in 2003 [180]. Since then, the requirements and procedures with which these observations are carried out were revised numerous times. Most notably the addition of CT5 to the array as well as the development and deployment of the Target of Opportunity alert reaction scheme [40] had significant impact on this program.

To date, H.E.S.S. follows up on GRBs detected by both the *Swift* and the *Fermi* missions. More accurately detections from *Swift*-BAT, *Fermi*-GBM and *Fermi*-LAT are considered for follow-up observations. The trigger conditions are separated into two classes of follow-up types:

1. 'prompt': GRB localisations which are observable with a delay of less than 5 minutes.
2. 'afterglow': GRB localisations that are visible with a delay with respect to the detection of more than 5 minutes.

Triggers falling into the 'prompt' category will initiate the follow-up observations fully automatically while 'afterglow' type triggers require the shift crew to schedule these observations in coordination with a GRB expert on-call. Follow-up observations of 'afterglow' localisations are possible to be triggered even up to 18 hours after the event. If delays are greater than 4 hours additional multi-wavelength information has to be available. Such multi-wavelength information can be counterpart detections or in the best case also redshift measurements.

Additionally, different visibility criteria are applied for the two cases: 'prompt' localisations should be observable for at least 5 minutes above an altitude angle of 30 deg. The follow-up of afterglow localisations are restricted to altitude angles of more than 45 deg. The temporal phase space is dramatically smaller for prompt follow-up cases. This is compensated by allowing for larger zenith angles which effectively increases the phase space for follow-up opportunities in order to have sufficient number of low temporal delay follow-ups.

Swift-BAT detected GRBs are selected for a potential follow-up based on the detection quality flags which the *Swift* team provides in their initial detection alerts. The following requirements apply in both the 'prompt' and 'afterglow' follow-up case:

1. `Definitely not a GRB = false`: This flag indicates a known different phenomenon which would lead to a significant detection in *Swift*-BAT (e.g. terrestrial flashes or charged particles hitting the instrument).

2. `Point source = true`: This flag indicates if the rate increase is indeed originating from a single point-like region in the sky. An extended emission would point towards another phenomenon or systematic effect.

3. `GRB identified = true`: This flag indicates that all observables point towards this detection being a GRB and not any other type of X-ray transient.

4. `Target in Ground/Flight catalog = false`. These criteria specify if a known source is found to be a consistent counterpart to the transient.

5. `StarTrack lost lock = false`. This indicates if the star tracker operated nominally and thus gives confidence in the validity of the reported localisation.

Fermi-GBM detected GRBs are followed up if a minimum burst significance of 10 sigma was reached. In addition, a requirement on the detection quality stating that the localisation is *Definitely not a GRB* (see above) to be false is applied.

Fermi-LAT detected GRBs are announced either through an online detection algorithm or an offline algorithm. In case of an online detection, the localisation is announced immediately. We do not impose any further requirements in such a case. In the case of an offline detection of the GRB, the localisation is typically available only within several hours. Therefore only the 'afterglow' follow-up case applies.

In order to estimate the rate of triggers that pass all criteria the public alert database (voeventdb) from 4πSky[1] was used. All described trigger conditions were applied to all alerts in the years of 2015 and 2016. The obtained numbers of triggers passing all criteria, averaged over both years are summarised in Table 4.2. As the numbers are relatively small, they may vary more strongly from year to year, largely due to the random locations of GRBs. Not all follow-up opportunities result in observations. Among the reasons for missed opportunities are weather conditions which prevent observations (e.g. clouds or rain), technical issues like a malfunctioning internet connection in Namibia as well as maintenance of the telescopes.

GRB observations amount to two hours per trigger which are taken as soon as possible for the respective case (prompt/afterglow). The expected follow-up rate is in the order of one every month.

The Neutrino follow-up program

The sources of the astrophysical neutrino flux measured by IceCube [55] are still not identified. As the limits for stable point-sources of neutrinos are getting more and more constraining, the search for transient sources are gaining in relevance. As neutrinos are produced in hadronic interactions in which also γ-rays are being produced, the search for transient γ-ray counterparts is a promising endeavour. Potential sources range from Active Galactic Nuclei (AGN) flares, to GRBs (see section 3.4).

Both IceCube and Antares share information on detections of neutrino candidates within seconds. This is the basis for the current H.E.S.S. follow-up campaigns to search for γ-ray

[1] `http://voeventdb.4pisky.org/`

Instrument	*prompt*	*afterglow* ($\leq$ 4 h delay)
Fermi-GBM	10	6
Fermi-LAT	$\leq$ 1	1
Swift-BAT	5	4
Total	**15**	**11**

Table 4.2: Estimated GRB follow-up opportunities per instrument and follow-up type. These numbers were estimated by averaging the follow-up opportunities which would have been possible with the described trigger criteria in 2015 and 2016. Due to bad weather conditions H.E.S.S. will not be able to follow up on all opportunities.

counterparts of astrophysical neutrinos on various timescales. Programs are in place for both IceCube and Antares neutrino candidates. These will be presented here.

IceCube Neutrino follow-up

IceCube provides information about detected neutrino candidates in multiple streams via their real-time alert system [173]. The available streams are:

- Gamma-ray follow-up (GFU): The gamma-ray follow-up correlates neutrino-like events with a list of known GeV- TeV γ-ray emitting active galactic nuclei [181]. This stream is in place for each experiment individually. IceCube sums neutrino candidates around the position of the predefined sources over long periods of time (up to months) in order to detect potential neutrino 'flares'. The amount of alerts the receiving experiment gets is adjusted to the amount of time the experiment is willing to spend on such follow-up observations by adjusting the signal to noise ratio requirement for each neutrino used by the algorithm.

- Optical follow-up (OFU): This is a similar approach as the GFU but does not use a predefined source lists, which removes a biasing factor. The timescales on which neutrinos are correlated are short ($\mathcal{O}(s)$). Typically doublet or triplet events are sufficient to trigger an alert [173].

- High Energy Starting Events (HESE): HESE events are track-like events where the vertex of the neutrino interaction is contained within the instrument volume of IceCube. This event class restricts the energy range to $E_\nu > 20$ TeV. At these energies background contributions from atmospheric neutrinos are non-negligible. Therefore alerts are only issued if the deposited energy is above 6000 p.e. which further increases the energy threshold of this event class to energies above a few hundred TeV. The ratio of astrophysical event rates to atmospheric background event rates rises to $> 30\,\%$ [173].

- Extremely High Energy Events (EHE): EHE events have an even higher energy and differ from HESE events topologically as their point of interaction is not contained in the instrumented volume, which results in a through-going track topography. EHE typically have energies above 100 TeV. Only about one of such events is expected per year.

The GFU and OFU streams are not yet commissioned for the Southern hemisphere but will become available in the near future. In addition to follow-up observations based on these streams, more observations were requested for the case that a counterpart to an astrophysical neutrino was able to be identified.

H.E.S.S. is currently the only IACT supporting a fully automated response to neutrino candidate events. This results in the shortest correlation timescales probable. Observations are only performed if the localisation of the neutrino candidate is visible at zenith angles of less than 60 deg. Observations are carried out for 2 hours per trigger as soon as possible.

Antares Neutrino follow-up

The volume of the Antares neutrino telescope is not as large as the one of IceCube. Therefore Antares is mostly sensitive to lower-energy neutrinos compared to IceCube. At lower energies the contribution from atmospheric neutrinos is large, which reduces the chances of neutrino-like events being of astrophysical origin. On the bright side, the denser instrumentation of the Antares detector allows for a better angular reconstruction than achievable in IceCube. Neutrino candidate events are reconstructed in near real time in order to alert other experiments [174, 182]. The event selection is similar to the IceCube streams and is controlled by the Antares collaboration.

Observations are restricted to zenith angles of less than 60 deg, same criterium in place for IceCube neutrino follow-up observations.

The Gravitational Wave follow-up program

Gravitational Waves were first proposed by Einstein [183] to propagate through space at all times as a consequence from his theory of general relativity [184]. Phenomena in which large masses are strongly accelerated were thought to be emitters of strong gravitational waves transients, although for many decades the direct observation of gravitational waves seemed out of reach. An indirect proof of the existence of gravitational waves was established by measuring the energy loss of the pulsar PSR B1913+16 in a binary system by Hulse and Taylor [185]. The energy loss of the pulsar was in the order of the expectation of gravitational wave radiation from the rotation of the two objects [186]. The most extreme scenario producing gravitational waves transients are mergers of two black holes. The first such detection was achieved in 2015 with GW150914 [52] by LIGO [187]. The gravitational wave observatories are steadily improving the communication of such detections to the community enabling faster searches for electromagnetic counterparts of gravitational waves. H.E.S.S. is among the partner experiments which perform follow-up observations of gravitational wave detections.

The LIGO Virgo consortium has not yet reached their aimed-at response time of announcing detections. Announcements and subsequent follow-up observations usually take place with delays of multiple hours. LIGO/VIRGO design goal for the circulation of alerts to multi-wavelength and multi-messenger partners is in the order of a few minutes. For the major part of the year 2017, the Advanced LIGO was running alone. This resulted in large positional uncertainties in the direction reconstruction of up to several hundreds of square degrees and poses a major challenge for any experiment that performs pointed observations. In H.E.S.S., an algorithm to determine likely and probable regions for potential follow-up observations by correlating the localisation uncertainty with galaxy catalogs [188]

has been developed. Observation time was allocated for proof-of-principle observations based on gravitational wave triggers.

In 2018 this program will be extended since several interesting gravitational wave events could be detected. Especially the case of GW170817 being the first GRB with a solid connection to a NS-NS merger strengthens the case for follow-up observations of gravitational waves. The proposed observations are grouped according to the merger types which are expected to be detected at different rates. The merger types cover BH-BH, BH-NS and NS-NS mergers as well as electromagnetic counterparts.

Other programs

A number of different follow-up programs are approved in addition to the already mentioned ones. As the probed phenomena are substantially different from the ones discussed in chapter 3, their discussion will remain brief.

- SGR/AXP/High-B-pulsar flares: X-ray telescopes also detect flares from magnetars or highly magnetic pulsars. Flares from such objects are called Soft-Gamma-Repeaters or Anomalous X-ray Pulsars. These events are quite similar to GRBs in their initial detection phase, even though being of galactic origin. H.E.S.S. runs a follow-up program which searches for flares that are detected by *Swift*-BAT and occur near to an object in a predefined list of known highly magnetised pulsars and soft gamma repeaters. A minimum photon count in BAT of 10000 is required in addition to the spatial coincidence with objects in this list.

- Flaring Stars: In 2013, Swift detected an X-ray flare and declared it a GRB [189]. This flare was later to be found to originate from a nearby star which underwent an extreme flare, more than 2000 times stronger than flares from X-class stars. As solar flares are already capable of accelerating cosmic rays up to energies of a few GeV, extreme flares such as the 2013 event are potentially accelerating particles up to energies at which γ-rays could trace them [190]. H.E.S.S. is searching for *Swift*-BAT detections of bursts in spatial coincidence with catalogued nearby variable stars.

- Fast Radio Bursts (FRBs) [191] are a novel class of radio transients. The term refers to bursts of radio emission with millisecond duration. Since the nature of this phenomenon is unclear, potential counterparts in γ-rays are not ruled out. Information about FRBs is shared with H.E.S.S. by the SUPERB project of the Parkes radio telescopes [192], enabling follow-up observations.

4.3 The H.E.S.S. Transients Alert System

This section will describe the H.E.S.S. transient alert system, its functionalities and its design. It was developed over the course of this thesis and fully commissioned in September 2016. Since then it is the central hub to receive and process transients alerts covering the full spectrum of previously introduced phenomena. It connects the detections of transients to the follow-up observation strategies defined by the H.E.S.S. Collaboration. As such, it has several key tasks:

- Receive alerts from a wide range of experiments and observatories.
- Link all approved follow-up programs and their criteria to incoming alerts.
- Evaluate for each alert if any of the associated science case requirements are fulfilled.
- Report the follow-up opportunities to experts and the shift crew.
- Issue follow-up observations fully automatically for time critical alerts.
- Allow to initiate observations regardless of the systems state.
- Provide results for the observations on a timely basis in order to decide on the continuation of the observation.

The alert system tries to achieve these goals in several steps. The key sub-components of the system are the alert receiver, a pipeline which associates alerts to science cases, processes and filters them, the Target of Opportunity (ToO) scheduling interface and the Real Time Analysis (RTA). A schematic overview of the different components and their interplay is shown in Fig 4.2.

In the following, the description of the individual components will follow the chronological order of the operations of the system as indicated in Fig 4.2. First, the used alert structure and transport mechanisms will be motivated, followed by a description of the Alert Receiver which is the interface between other experiments and H.E.S.S. Next will be the parsing of the alert through which the alert can be associated to the observation programs and criteria defined by the collaboration. Then, the ToO scheduling will be described which handles the communication between transient follow-up opportunities and the telescope steering. Finally, the RTA will be described. The RTA analyses the observational data in real time such that transients in very-high-energy γ-rays can be identified and observed further.

Alert format and transport

The reaction to transient alerts depends on receiving alerts in the first place. The different transient alert distribution mechanisms were briefly introduced in section 4.1. The format of the alerts and the way alerts are transferred is therefore crucial. Ideally, the choice of alert format and transport are standardised throughout the community, such that compatibility between different experiments and observatories is ensured.

The format and the protocol of the alerts that are distributed by the GCN were a 160 B binary packets. In recent years, the International Virtual Observatory Alliance (IVOA), an institution that connects the different communities in transient astronomy, defined standards for the format of the alert itself called VOEvent [193] as well as for their transport (VTP, VOEvent Transport Protocol) [194]. Both VTP and VOEvent are supported by GCN in addition to the binary packets.

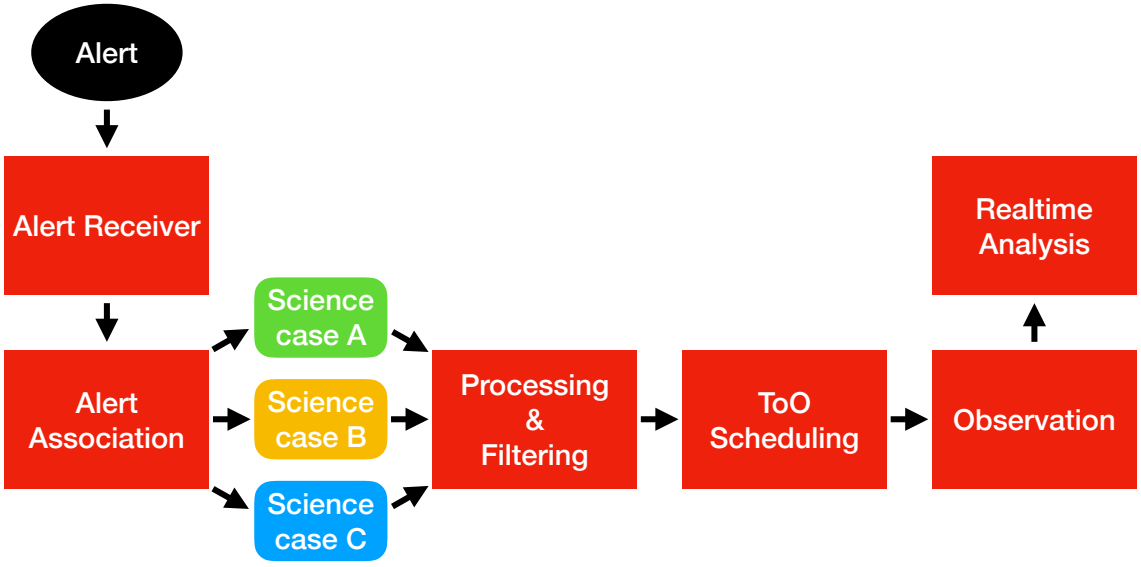

Figure 4.2: Workflow of the Transients Alert System, indicating different steps in the processing of incoming alerts by the individual components. Every alert triggers a separate process. Each alert can be associated to multiple science cases which could be probed. All associated science cases are evaluated following a priority order. After the science cases are processed and filtered, ToO observations are being scheduled. The data from the observations is being analysed in real time.

The IVOA recommended the usage of XML files for the communication of transient celestial events. In these XML files the main aspects of a transient event have to be grouped in the sections *Who*, *What*, *Where-When*, *How*, *Why*, *Citations*, *Description* and *Reference*. Each piece of information given within these fields are identified by variable -*name* and *value*. Optionally a variable can also have a *unit*, *type* and a *description*. This way the alerts are easy to read for machines as well as humans. A useful package that helps with creating, modifying and parsing VOEvent files is voevent-parse [195], which was used throughout the H.E.S.S. system. For a detailed description of the alert format, the reader is referred to [193]. The communication of alerts is organised in a distributed way, namely a network of brokers that can subscribe to each other without the need for a central hub that distributes alerts to everybody. A broker in this network represents an entity that receives alerts from *Authors* and distributes them to subscribed brokers. Brokers keep the connection up at all times, monitored using *iamalive* messages. During every step of sending and receiving alerts, the event is checked to comply with the VOEvent standard.

Alert receiver

Although the format of alerts (VOEvents) and their transfer (VTP) are chosen, transient alerts still need to be received by the computing cluster of H.E.S.S. in Namibia in order to make proper use of the information contained in them. This aspect is handled by the Alert

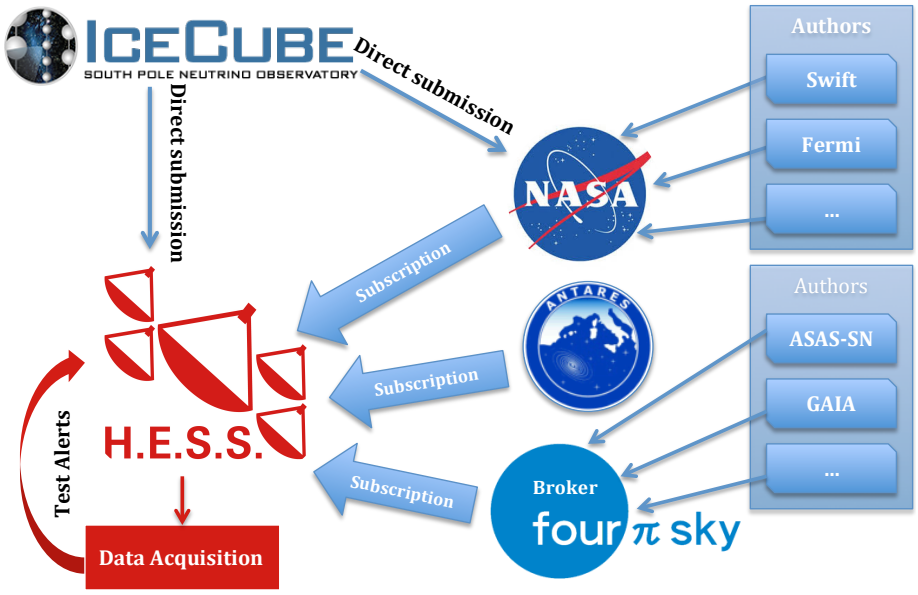

Figure 4.3: Sketch that illustrates to which hubs of alerts H.E.S.S. is connected using VTP [194]. Alerts on high-energy neutrino detections from IceCube are send to GCN (via AMON) but are also directly submitted to the H.E.S.S. broker.

receiver which establishes the connection between different experiments and hubs and stores incoming alerts for further use.

The Alert receiver is based on *Comet* [196], an implementation of the VTP allowing for an easy way to receive and distribute transients celestial events in the VOEvent format. The comet tool runs in receiver mode and is subscribed to alerts from several hubs that distribute alerts and individual experiments as indicated in Fig 4.3. The comet process is running on the central computing cluster on the H.E.S.S. site in Namibia and in a test environment at DESY Zeuthen. The process is monitored by the watchdog tool *monit*[2]. Every alert that is received by the receiver is archived on the clusters. The path of this archived alert file is then given to the filtering pipeline. Archived alerts are frequently used in order to test the systems response for a new release of the transient alert system before it is fully deployed.

The H.E.S.S. alert system is well connected with missions involved in time-domain astrophysics. Subscriptions to brokers such as GCN, 4PiSky, Antares as well as ATOM are in place. Additionally alerts can arrive from IceCube as a direct submission to the H.E.S.S. alert receiver which is realised through whitelisting of the IceCube data centre IPs at the University of Wisconsin-Madison. Furthermore, self-generated test alerts can be received. A sketch of the connections of the H.E.S.S. transients alert system is depicted in Fig 4.3. About 60.000 alerts are received each month.

Alert association and filtering in the alert processing pipeline

Based on the alerts which are received, the transient alert system needs to identify if follow-up observations should be carried out. This evaluation is performed in several processing

[2] `https://mmonit.com/monit/`

steps. First the alert is associated to transient follow-up programs. For this task, several alert configurations are considered for each alert (as indicated by the different science case boxed A-C in Fig 4.2). Secondly, the triggering criteria are being evaluated based on information which is either stated in the alert itself or which can be deduced from it.

Both tasks are performed by the association and filtering pipeline, a python tool that parses alerts in the VOEvent format, correlates it to science case definitions, explores follow-up opportunities and alerts experts, shifters and the central data acquisition. For every incoming alert an individual process of this pipeline is started by the alert receiver.

Alert association to science cases

In a first step, important information of the alert is extracted using *voevent-parse* [195]. Most important are the coordinates and uncertainty of the localisation, the IVORN, a unique identifier for the alert, as well as the timestamps of the alert and the astrophysical transient event itself. Additionally the authoring experiment and the alert type is extracted from the alert.

Using this information the alert is associated to the predefined follow-up requirements. Each alert can be considered to address multiple science cases. A list of all alert types of relevance for transient follow-up observations and their associated science cases is given in Table 4.3. In addition to the alerts given in this table there are several alerts that are used as test alerts to monitor the system, as well as a few alert types that are treated as *spam*. Alerts matching the spam category are automatically removed from the archive, usually due to their high occurrence rate. Out of the roughly 60.000 alerts which are received monthly only around 18.000 are stored in the archive. If all auxiliary (e.g. pointing directions of spacecraft) and test alerts are subtracted 1500 alerts per month remain. Alerts which are listed in Table 4.3 amount to roughly 50 alerts per month which relates to an alert reduction by a factor of 1000 through the association to science cases. A monthly overview of received, stored and science related alerts is shown in Fig 4.4.

The intermediate result of the association are multiple pairs of the alert itself and a science case definition (in form of a configuration file). Further evaluation is performed pair by pair. An ordering in importance is in place to ensure that time critical science cases are evaluated first.

Processing and Filtering

Once the pairing of the alert with a number of science cases has been performed, the follow-up requirements need to be evaluated. Each pair of alert and science case has its own configuration file in which the follow-up requirements are defined. Such requirements fall into different categories. Visibility requirements are based on the time of the event and the localisation coordinates, which are common parameters for essentially all alerts. Parameters indicating the alert quality or measurements typically differ from alert type to alert type and instrument to instrument. Therefore, each alert-science case pair has to be handled individually.

Visibility

Requirements on the visibility of the position are common for all science configurations. They are defined by a limit in altitude for the observation, a minimum and maximum delay of the follow-up window with respect to the astrophysical event as well as a minimum dura-

Type of Alert	linked science cases
Fermi#LAT_Updated_Pos	GRB prompt, GRB afterglow
Fermi#LAT_Offline_Pos	GRB afterglow
Fermi#GBM_Gnd_Pos	GRB prompt, GRB afterglow
BAT#GRB_Pos	GRB prompt, SGR/AXP prompt, GRB afterglow, SGR/AXP afterglow, Flaring Star Prompt, Flaring Star Afterglow
AMON#ICECUBE_COINC	Neutrino prompt, Neutrino afterglow
IceCube#HESE	Neutrino prompt, Neutrino afterglow
AMON#ICECUBE_EHE	Neutrino prompt, Neutrino afterglow
AMON#ICECUBE_HESE	Neutrino prompt, Neutrino afterglow
Antares#Alert	Neutrino prompt
MAXI#Unknown	Flaring Star Prompt, Flaring Star Afterglow
MAXI#Known	Flaring Star Prompt, Flaring Star Afterglow
LVC#GXXXX_Initial	Gravitational Wave
LVC#GXXXX_Updated	Gravitational Wave
LVC#Counterpart	Gravitational Wave EM
HESS#FireDrill	FireDrill

Table 4.3: List of different alert types in combination with their associated science cases for which they are employed. Each pair of alert identifier and science case has its own follow-up requirements. The Alert identifiers from AMON are duplications to the IceCube HESE alerts that H.E.S.S. receives directly from IceCube. Both are used for the sake of redundancy.

tion of the observation window. These visibility criteria are the main separating conditions between the *prompt* and *afterglow* follow-up cases.
To incorporate different timescales to probe, the search window for potential follow-up opportunities is selected dynamically in relation to the typical observation duration which is stated in each configuration. The time range which is probed is binned differently depending on the time difference to the event time. A fine binning close to the event time allows for precise evaluation of the visibility conditions and therefore precise start and stop times of potential observation windows. Larger binning allows to cover the transients position over multiple day-night cycles without too much computation time.

The altitude and azimuth angles of the sun, the moon and the target position are calculated for every point in the time grid using *astropy* [197] and *pyephem*[3]. Based on the altitude angles of the sun, moon and target, the visibility requirements are verified. The employed darkness criteria require the sun and the moon to be at altitudes below $-18\,\mathrm{deg}$

[3] http://rhodesmill.org/pyephem/

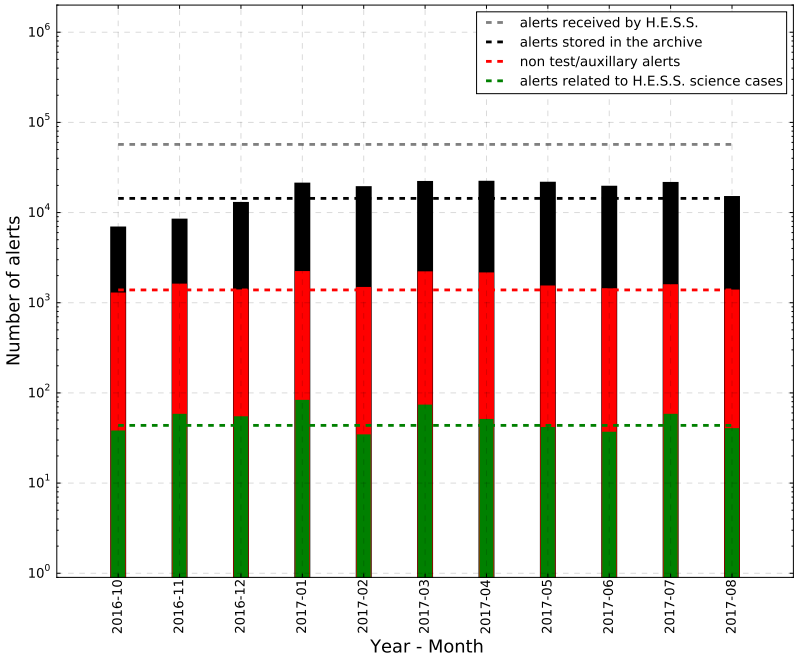

Figure 4.4: Overview of the number of alerts which are received by the H.E.S.S. alert archive per month. In the order of 18.000 alerts are stored per month. If all auxiliary alerts (e.g. pointing directions of spacecraft) and test alerts are subtracted, around 1500 alerts remain per month. In the order of 50 alerts per month are related to science cases with running transient observation programs.

and $-0.5\,\mathrm{deg}$ respectively. Every found follow-up opportunity window needs to be at least as long as the minimum observation duration which is specified in each configuration. The earliest possible follow-up window is used in order to alert experts and the shift-crew. In the case of *afterglow* triggers, this alert will be a mail that outlines the alert, the science case that passed all criteria as well as a graphical representation of the follow-up window that was found (see Appendix A.4 for an example). The shift-crew will also be alerted by a pop-up that states a summary of the alert as well as instructions.

A special reaction scheme is in place to allow for a faster reaction to transients that are observable without delay. Therefore, a quick test is done to determine if the position of the alert is visible at the time at which the alert is processed. In the case that the delay between the event time and the time at which the visibility is being evaluated falls into the required time range for the probed science case, the position will directly be forwarded to the scheduling part of the alert system. If not, the previously described algorithm will search for future follow-up windows and announce an afterglow opportunity.

Alert quality parameters, measurements and special filtering routines
Alert quality parameters and measurements are different from alert type to alert type and instrument to instrument. This requires to specify which parameter is given in which section of the alert file and what the required value of each parameter is. The requirements for the

individual follow-up programs that are evaluated in some cases are presented in section 4.2. Requirements based on flags or values in the alert file are read from the science case configuration and validated on the alert file. Flag-based requirements are typically indicators on the data quality and type of detection. Values that are commonly checked are for instance the significance or counts of the detection.

In addition, *special* filtering algorithms can be used in order to e.g. correlate catalogs with objects of interest with the localisation of the transient (as it is done for the follow-up of SGRs or flaring stars). Also more complex algorithms which determine a full follow-up schedule as for instance in the case of follow-up observations of Gravitational Wave detections [188] are possible to be included. These special requirements are implemented on a case by case basis in the system as the follow-up strategies are being established. Each processing of an alert will only trigger the calculations which are needed to perform the filtering. This modular approach makes this filtering system flexible and scaleable. Information on each step of the filtering process is written into log files for each science case that is being tested.

Auxiliary science case parameters
Once an alert passed all criteria for follow-up observations, a reaction of the transient system is desired. The details of the reaction is specified in each configuration by a set of parameters specifying the following: is the alert self-generated (e.g. for testing purposes), should the telescopes be allowed to slew in reverse mode, should potential observations be started fully automated and what is the priority[4] of this science case.

The configuration file approach allows for good flexibility as it allows to change the behaviour by changing the configuration instead of the pipeline. Adding another follow-up science case can be achieved by simply defining a new configuration file and linking alert types to it.

Target of Opportunity observation scheduler

The Target of Opportunity (ToO) scheduler is the interface of the alert system to the array control software of H.E.S.S. It is responsible for the automatic reaction of the telescopes to transient alerts. This ToO scheduler is only used in the case of alerts which can be followed up promptly. Afterglow-type observations are added into the schedule with the help of scripts as they are not as time critical and not integrated into this component.

The ToO scheduler is represented by a state controller within the central data acquisition software [41, 40]. The two main states of this controller are *Safe* and *Running*. In the safe state, all automatic reactions of the array to alerts are turned off. The controller can be in the safe state either because the receiver process is not running, or for safety reasons during the night whenever the shift crew has to access the array. The main functionality of this controller are (i) the interface through which alerts are received from the filtering pipeline and (ii) the interface to the telescope steering software. In between, several corner cases depending on the array status are handled.

Once the filtering pipeline has determined that an automated reaction should take place, a reduced set of information about this alert is compiled and sent to the controller using the Common Object Request Broker Architecture (CORBA) [198] that is applied throughout

[4]The priority parameter is only used for fully automated reactions which will be described in more detail in the following section.

the data acquisition software of H.E.S.S. The reduced alert contains the IVORN, author experiment, alert type, alert id, science case name, priority rank, coordinates, altitude limit, event and alert time stamps, the maximum observation time as well as flags that specify if the reverse slewing mode is allowed and if the alert is self-generated. The state of the controller is verified to be in *Running* before an incoming alert can trigger the automatic repointing of the telescopes. As this has been verified, the automatic repointing procedure first contacts the run manager to verify that it can receive the repointing command. Furthermore, another pop-up is issued to let the shift-crew know that the automatic procedure was initiated.

Finally, the sky location currently viewed by CT5 is evaluated in order to avoid stopping the data taking in case that the new target position is already in the field of view. Should this be the case, the current observation is prolonged for 28 minutes. Only if repositioning needs to be done, the alerts parameters are given to the run manager with the repointing command. This will lock the interface for new alerts for a brief 40 s time in order to let the system react. Alerts that enter the ToO scheduler during this time interval are queued in a list of pending alerts. The controller loops over the list of pending alerts and determines if one of the alerts queued is: a) of higher priority than the alert that is already being observed, b) an update to the alert that is already being observed, c) outdated and therefore removed from the list or d) now scheduled because the currently being followed alert has just timed out.

A special transition mode allows for a faster start of the observations whenever the ToO scheduler initiates new observations [40]. This is done through the usage of the so called *ToOObservationRun*. This run type marks all dependencies that CT1-4 normally impose on CT5 during the run transitions as optional. Therefore the observations start as soon as the new target position enters the field of view of CT5. CT1-4 will typically join the observation a few ten seconds later. The speed up is only applicable in the start of a new observation run. The previous run abortion is still determined by the normal *ObservationRun* processes. The stopping and starting of run incorporates many camera related processes as well as the slewing. Among the camera processes are e.g. switching between high-voltage and low-voltage, determining and setting the correct camera (trigger) settings for the next pointing as well as finalising reading the buffered data. The slewing of CT5 in reverse mode is supported only in the *ToOObservation* run type.

For every automatic repointing, a VOEvent alert is generated and sent to the Automatic Telescope for Optical Monitoring (ATOM) [199] located at the H.E.S.S. site. This allows for optical observations for every transient follow-up performed by H.E.S.S. This feature is currently under development.

Realtime analysis

The analysis of the data that is being taken is usually only possible once the data was transferred to the computing centres in Europe. Including the calibration and reconstruction of the data this can take up to a few months. In order to get preliminary analysis results already during the data taking or the day after, an analysis chain is running on the data acquisition cluster in Namibia. This feedback allows to judge if certain observations should be prolonged during the night or if more data should be taken on a source in the consecutive

night. The real time analysis provides valuable feedback for any kind of observations and not only in the case of transients.

The reconstruction method that is being used in the Real Time Analysis (RTA) is a mixture of a Hillas parameter based image reconstruction with the addition of a multivariate gamma hadron selection [200]. Based on the observation, the RTA decides which reconstruction mode is being used. In case of the standard ObservationRun the stereo mode is used, which employs the data from all telescopes and requires the showers to be seen by at least two telescopes in order to make use of stereoscopy. For ToOs the Mono mode is chosen where the full reconstruction is done using only CT5 data [201] in order to allow for the lowest possible energy threshold.

As the data is analysed during the observation, the standard calibration methods can not be applied. There is no flat fielding which is being applied and the conversion factor from ADC counts to photo electrons is a fixed ratio. A quality criteria is applied for each pixel which requires the pedestal to sit in the usual range in order to be used in the analysis. The pedestal calibration factors are calculated as a weighted mean between the value obtained for the previous event and the new event for each pixel [202].

The results obtained from this analysis were used to communicate results of H.E.S.S. observations in several cases: the detection of a flaring episode of the flat spectrum radio quasar PKS 1510-089 [203] and the blazar 3C 279 [204]. Also non-detections of a VHE-γ-ray counterparts to the astrophysical neutrino candidates detected by IceCube [205, 206] were announced making use of the RTA results.
An extension of the realtime analysis functionality to feed back its results to the transient alert receiver is currently under development. Such functionality would allow for the fully automated triggering of follow-up observations for known and unknown targets based on the measured VHE γ-ray activity.

4.4 Performance of the Transients Alert System

Discussing the performance of the system encompasses several aspects. A central quantity is the reaction time with which H.E.S.S. is able to perform observations in response to a celestial transient event. This reaction speed is however a combination of multiple contributing factors.

Along with the reaction speed, numbers for the alert reduction which were mentioned already during the description of the alert receiver and the alert association, filtering and processing pipeline will be summarised again.

Reaction speed

Delay of alert reception

A first delay with respect to the transient event itself occurs between the event time and the time at which the alert is circulated to the community. This delay has some dependence on the strength and time structure of the transient. Also the spacecraft position has an impact on the data downlink speed to earth. The time between the astrophysical event and the alert timestamp was estimated by comparing the authoring time of the alert with the event time

using archival public alerts in the 4πSky database. The delays were found to range in the order of 30 to 100 seconds for *Fermi*-GBM and *Swift*-BAT GRB alerts. This is an irreducible delay for any follow-up observation.

H.E.S.S. intrinsic delays
The ToO scheduler receives reduced alerts from the filtering, association and processing pipeline in case that the alert should be followed up automatically. The delay with which the alert is received by the tracking of CT5 with respect to the time at which the alert was received by the alert receiver was estimated to be below 5 seconds. This number depends on the number and complexity of the applied filtering algorithms and varies from one science case to the next. This estimate includes all steps described in the previous section.

The transition to ToO observations is the main aspect which adds a non-negligible delay to the reaction to alerts. This transition covers the whole process of stopping the current observation, up to the first event being observed from the new target sky region. This delay was estimated using the self-triggered test alerts as well as real alerts. In total 41 automatic repointing procedures were selected for this study. Three main contributions are identified:

- Stopping the run, which includes switching from high-voltage to low-voltage in the cameras and finalising the processing of all recorded data. In total 10 to 25 seconds are spent in this transition.
- The time needed for slewing from the old to the new coordinates depends on the distance between the coordinates. Hofverberg et al. [39] evaluated the CT5 slewing speed to $1.67\,\mathrm{deg\,s^{-1}}$. The azimuth and elevation drives allow CT5 to move between 78.5 and 638.5 deg and -32 to 175 deg respectively. If this range would be exceeded over the course of the next observation run, the telescope is not allowed to use the fastest way to the new target coordinates. This can result in longer slewing times than expected for the angular distance between the old and new coordinates.
- Starting the new run also adds a delay in the range of 2 to 20 seconds. This includes camera processes like setting the new high voltage values, setting the new trigger configuration as well as the tracking process of switching from slewing to the fine tracking mode.

The distribution for each of these contributions is shown in Fig 4.5 as well as the combined stopping and starting of the run, which is independent of the slewing distance. The total delay as a function of the angular distance between the old and new coordinates is shown in Fig 4.6 on a case by case basis. Additionally the expectation using the baseline from stopping and starting the run in addition to the slewing time is shown. The spread of this expected time range originates from the minimum and maximum values in the combined stopping and starting delay distribution in Fig 4.5. The colour code of each bar decomposes the transition time into the three previously mentioned components.

The six cases in which the total time needed for the transition to the ToO observation significantly exceeds the expectation are resolved when the actually slewed distance is taken into account instead of the angular distance between the old and new coordinates (as mentioned above). If one includes the delay of less than 5 seconds required for the alert association, filtering and processing, Fig 4.6 highlights that the full reaction of the H.E.S.S. Transients system to alerts of less than 100 seconds is commonly achieved. This is in the

order of the delay with which transient alerts are circulated. For a more detailed decomposition of the large number of individual hardware and software processes of all relevant systems, the reader is referred to Balzer et al. [41, 40].

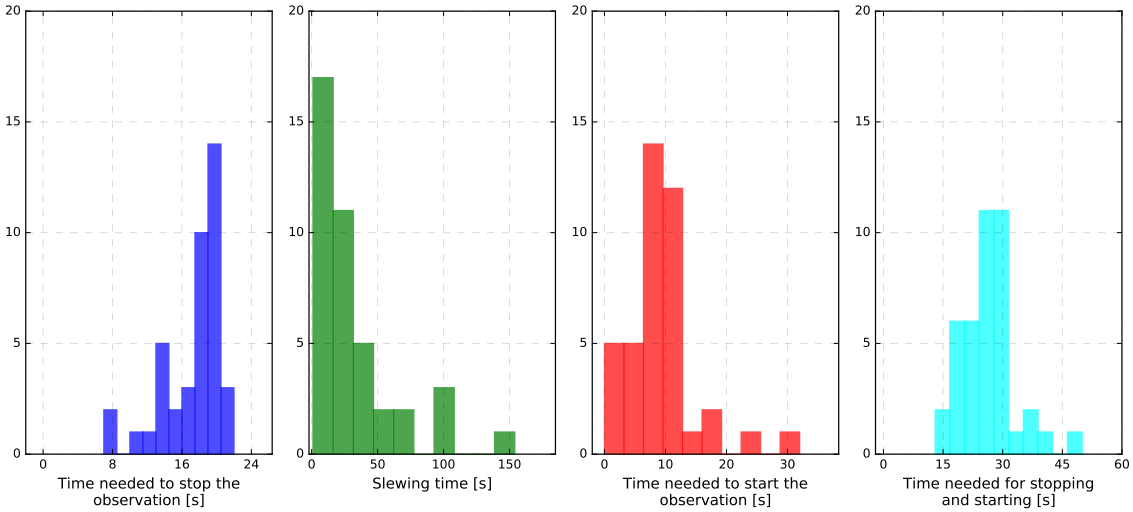

Figure 4.5: The three panels on the left show histograms of transition delays due to the stopping of the ongoing run (blue, left), slewing to the new target position (green, left centre) and starting the next observation (red, centre right). The right panel (cyan) shows the histogram of the sum of both stopping and starting the run which are independent of the angular distance between the previous and new target positions. This can be taken as a baseline delay which ranges between 15 and 50 seconds with a mean of below 30 seconds. The histograms are based on the full sample of all 41 automated pointing transitions.

Alert reduction

The alert receiver receives in the order of 60.000 alerts each month. Even though the delay between the alert authorship and the reception of the alert is in the order to one to two seconds, a relatively large delay is already present at this stage due to the detection of the transient itself. The delay times between the astrophysical event and the authorship of the alert varies depending on the alert type and the instrument and range between a few seconds and several hours.

The Filtering and processing pipeline classifies 45.000 alerts as "spam". It further associates alerts to the science case definitions in place for which H.E.S.S. follow-up observations are approved. These science related alerts amount to roughly 50 alerts per month. An overview is given in Fig 4.4.

4.5 Conclusions

The range of transient phenomena worth to follow-up with IACTs is broad. Many of the desired campaigns are constrained by the information that is published by the many different survey instruments. Complex systems are necessary to access the plentiful science questions

addressable with transients. Here, the system for H.E.S.S. was described which is able to cover many different messengers and timescales. It allows for fully automated reactions to transients alerts and provides immediate results of the observations. The performance evaluation of the alert system demonstrated that repointing the telescopes adds to the delay with which H.E.S.S. can react to alerts in on the same order as the delay due to the detection and circulation of alerts. The modular approach allows for a high level of flexibility, making changes in the triggering conditions or addition of science cases easy.

These developments allowed H.E.S.S. to broaden the transient observation programs. Since its commissioning in 2016, the new alert system allowed for interesting observations, ranging from GRBs, to Neutrino and Gravitational Wave follow-up observations. With the help of this system, H.E.S.S. has successfully arrived in the multi-messenger era of γ-ray astronomy. Selected highlight observations of transients with H.E.S.S. II will be presented in the following chapter.

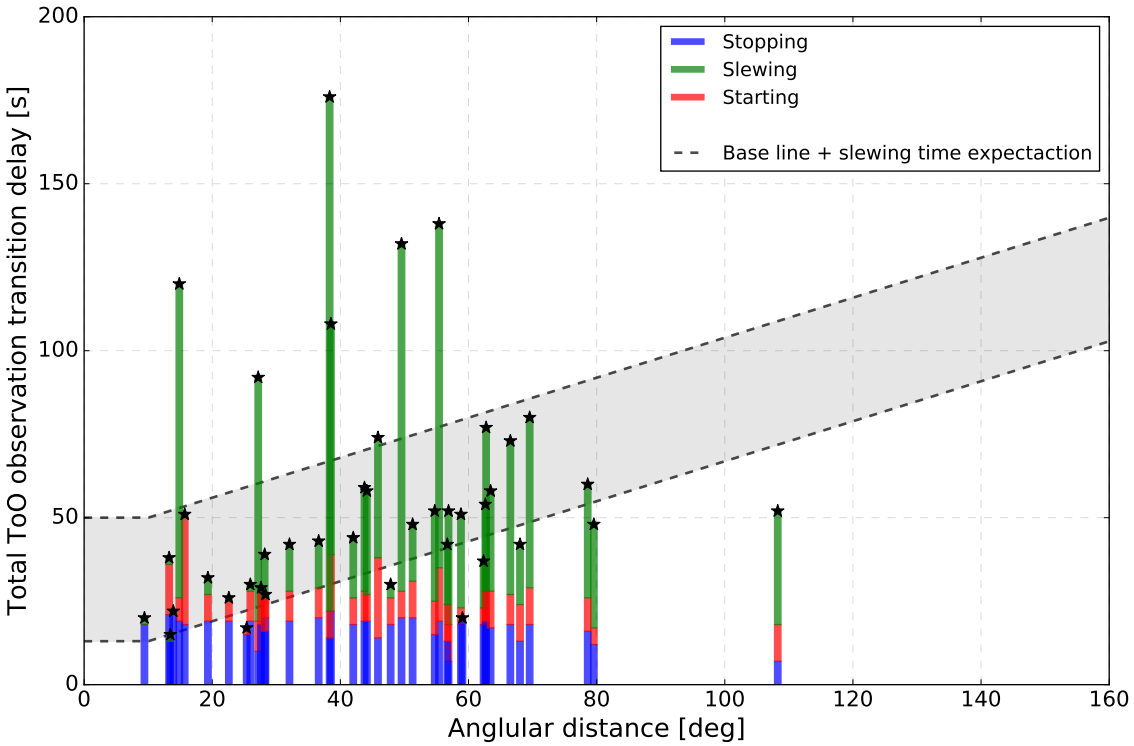

Figure 4.6: The total transition delay from stopping the previous observation to start of the new observation is shown as a function of the angular distance between the old and new coordinates for each of the 41 automatic repointings individually. The colours decompose the total delay into the three contributions of stopping the previous run, slewing to the new target and starting the new observations in blue, green and red respectively. The grey shaded area highlights the expected delay as a function of the angular distance by assuming a constant contribution from stopping and starting of the run in addition to the slewing time with a speed of $v_{slewing} = 1.67\,\mathrm{deg}\ s^{-1}$ [39]. The large delays of the six repointings which exceed the expectation significantly, can be corrected for the actually slewed distance which can differ from the angular distance between the pointing positions due to the azimuth and elevation drive motion range constraints.

Chapter 5

Highlights from Follow-up Observations of Transient Events

As demonstrated in the previous chapter, the transient alert system allows for novel follow-up observations of different transient phenomena. It allows to make best use of CT5 and its low energy-threshold and rapid repointing capabilities. This chapter presents highlights from transient follow-up observations with H.E.S.S. II based on external triggers received and processes by the alert system.

A few selected GRB observations and results will be highlighted. These observations were carried out before the commissioning of the transient alert system but indicate the H.E.S.S. II performance that can be expected from GRB observations since 2012.

Another focus of the system is the connection of H.E.S.S. into the multi messenger community which was manly driven by connections to both neutrino and gravitational wave astronomy (see section: 4.2). With the transient alert system in place since the end of 2016, several important datasets were acquired. After a brief report of the follow-up performance for both messengers, one high-impact dataset for each messenger will be discussed:

- IceCube-170922: a neutrino candidate that was found in spatial coincidence with the blazar TXS 0506+056. This blazar was in a high emission state at GeV γ-rays, which in the subsequent IACT follow-up campaigns was found to be flaring in TeV γ-rays too.

- GW 170817: a gravitational wave originating from a NS-NS merger which was also detected by *Fermi*-GBM as a short GRB.

As follow-up observations can not be repeated due to the transient nature of the target phenomena, special care has to be taken during the analysis of the data. Over the course of this thesis, procedures for the analysis of transient phenomena were developed. These procedures have been reported in section 1.3 and are common for all results which will be discussed here.

5.1 Gamma Ray Burst Follow-up Observations and Results

The results of GRBs observed in the H.E.S.S.I era were published in [207]. The study covered 22 GRB follow-up observations performed in the period from 2003 to 2007. The energy threshold for these observations ranged from 250 GeV to 1.5 TeV. Recalling the EBL

constrains presented in section 3.5, this corresponds to a redshift horizon in the order of $z < 0.5$ which misses the bulk of the GRB redshift distribution. The fastest reaction time achieved was 6.5 minutes. The majority of observations however started with more than 300 minutes delay.

The improvements of H.E.S.S. with the addition of CT5 in 2012 are numerous. H.E.S.S.II allows for faster reactions and lower energy thresholds as described in section 1.3. H.E.S.S.II therefore extends the phase space of the GRB population that can be probed quite dramatically both in terms of the energy range and the delay with respect to the burst. An overview of the observations carried out since 2012 together with a few selected results will be presented in this section. Finally the results will be discussed in terms of sensitivity and their implications in the time-domain of GRB evolution.

GRB Follow-up statistics

More than 30 GRB detections by *Fermi* and *Swift* were followed up by H.E.S.S. since 2012. CT5 was not available for all observations. Among the reasons are technical difficulties or unclear weather situations which made observations with CT5 not possible. The observations for which CT5 was available are displayed in Fig 5.1. Each follow-up is shown in the plane of the two most relevant criteria for GRB observations: The zenith angle under which H.E.S.S. could observe the final burst position, which dictates the energy threshold, as a function of the time of the observation with respect to t_{Burst}. The delay between the observation start and $t_{\mathrm{Burst}}$is a sum of the time necessary for (a) receiving and processing of the alert and repointing of the telescopes, (b) the detection of the event itself and the distribution of the alert, which involves the downlink from the satellites to the ground and ultimately to the H.E.S.S. site. The delay of each individual alert type is the baseline for all H.E.S.S. follow-up opportunities. The typical delay ranges for the distribution of the different alert times utilised in the GRB program are highlighted on the bottom of Fig 5.1 and were derived based on the history of alerts from 2015 and 2016.

Reaction times of less than 100 seconds are achieved on a regular basis. this is compatible with the estimated repointing performance presented in section 4.4 and significantly faster than what was achieved in any GRB follow-up between 2003 and 2007 [207]. The energy threshold is proportional to $\cos(\theta_{\mathrm{zen}})^3$ where the θ_{zen} is the average zenith angle of the observation. The red dashed axis therefore indicates an approximate energy threshold corresponding to zenith angles at which the bursts were observed. The exact threshold for each individual observation however depends among other aspects on the atmospheric conditions and the homogeneity of the pointing pattern. Comparing to the study of GRB observations with H.E.S.S. from 2003-2007 [207] one can see, that CT5 observations with zenith angles below 45 deg yield lower energy thresholds than the best candidates observed with H.E.S.S.I. The green circles in Fig 5.1 highlight the three bursts which will be discussed in more detail in the following.

Selected GRB Observations and Results

The three bursts which will be discussed in more detail are GRB 140818B, GRB 140901A and GRB 150415A. Information on their detection and the H.E.S.S. follow-up observations is given in Table 5.1. A quick summary of the burst, the data and the analysis results for each of the three will be given in the following.

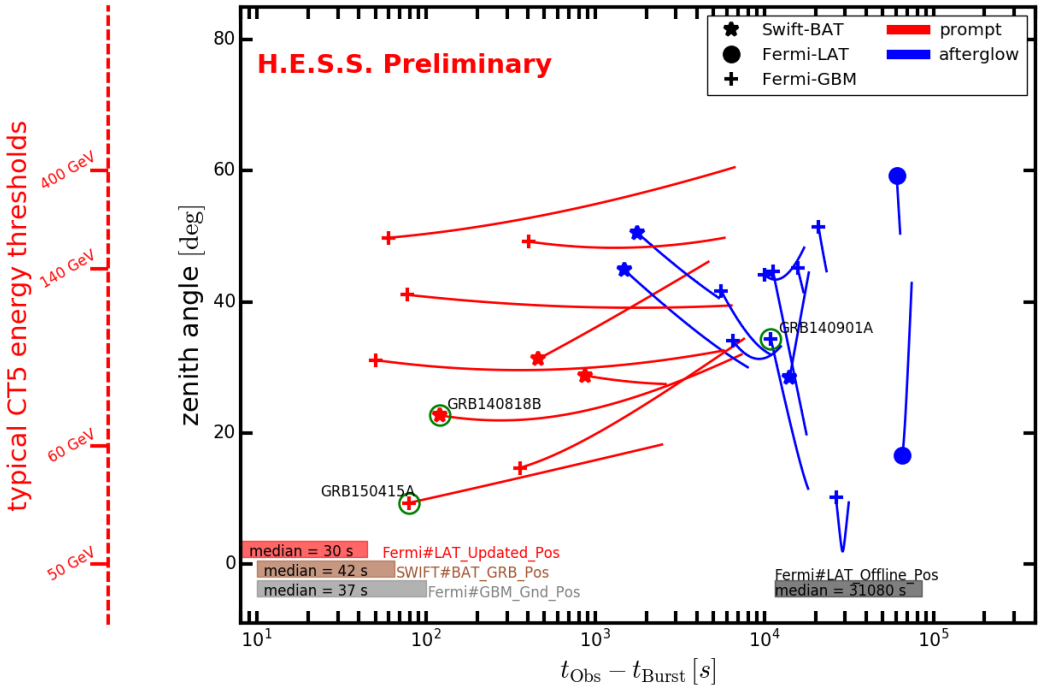

Figure 5.1: Overview of H.E.S.S. GRB follow-up observations from 2012 to May 2017 for which CT5 was available. Each marker denotes the start of an observation. The line following the marker denotes the evolution of the zenith angle under which the final location of the burst was visible from the H.E.S.S. site at the time of the observation. The typical delay timescales for every alert type was evaluated using the public alert archive from 2015 to 2017 and is shown at the bottom of this figure. This delay is the baseline for the H.E.S.S. reaction and repointing speed. Red markers denote observations that were taken in a fully automated way, while the blue ones were scheduled by scripts due to their longer delay. The additional red axis denotes the energy threshold that roughly corresponds to the respective zenith angle.

	GRB 140818B	GRB 140901A	GRB 150415A
General information on the GRB detection			
Observations triggered by	*Swift*-BAT	*Fermi*-GBM	*Fermi*-GBM
T_{90}[s]	18.1	0.16	8.0
Also detected by	UVOT, XRT, IPN	IPN	–
Significance	$10\,\sigma$	$68\,\sigma$	$19\,\sigma$
Redshift	×	×	×
Final position of the GRB			
Right-Ascension (J2000) [deg]	217.15	15.82	220.63
Declination (J2000) [deg]	−1.36	−32.76	−19.34
Position uncertainty (stat.) [deg]	0.05	2.5	3.6
H.E.S.S. Observation parameters			
Average zenith angle [deg]	25	22	13.7
Delay of observation start w.r.t t_{Burst}	120 s	3 hours	80 s
Observation time	2 hours	2 hours	40 minutes
Fully automated reaction	✓	×	✓
Energy Threshold [GeV]	100	80	80

Table 5.1: Summary of information about the three selected H.E.S.S. GRB follow-up observations and their detection in X-rays.

GRB 140818B was a long burst with a duration of $T_{90} = 18.1\,\mathrm{s}$ and was detected by *Swift*-BAT. H.E.S.S. observations were triggered promptly. Data taking started with a delay of only 120 s with respect to the burst time. The location of the burst was observed for two hours with an average zenith angle of 25 deg, resulting in an energy threshold of about 100 GeV. No significant emission could be found over the course of the two hours exposure. The differential energy flux upper limits are shown in the upper left panel of Fig 5.2 together with the measured X-ray flux during the prompt phase which is not contemporaneous with the H.E.S.S. observations. The differential limits obtained between 100 GeV and a few TeV are approximately five orders of magnitude below the prompt flux level measured by *Swift*-BAT.

The soft X-ray afterglow light curve obtained by *Swift*-XRT is available for GRB 140818B and is shown in Appendix A.5 in comparison to the limits obtained at energies of 100 GeV. The X-ray energy flux (0.2 - 10 keV) of this GRB at the time of the H.E.S.S. observations was in the same order as the integral energy flux upper limit above 100 GeV.

GRB 140901A was a short ($T_{90} = 0.16\,s$) intense burst detected by *Fermi*-GBM. H.E.S.S. performed follow-up observations with a delay of roughly 3 hours. The positional uncertainty quoted for this burst of 2.5 deg is about as large as the H.E.S.S. II field of view. The position was observed for two hours with an average zenith angle of 22 deg, allowing for an energy threshold of $\sim$ 80 GeV.

The best spectral fit in X-rays was found to be the band function with the peak at around 1.2 MeV and is shown in the middle panel of Fig 5.2. The band model can be extrapolated into the HE and VHE γ-ray domain (neglecting any potential additional inverse Compton components or absorption features). This extrapolated energy flux overshoots the H.E.S.S.

limits. Contemporaneous observations would have been quite constraining, although such an observation is only possible if the GRB is in the FoV serendipitously.

As the burst was only seen by *Fermi*-GBM, the localisation uncertainty is large. The statistical uncertainty of the localisation alone is 2.5 deg. To probe the degradation of the sensitivity across the field of view, the upper limits were derived at a distance of 1.5 degree from the centre. The loss in sensitivity was found to be only marginal, allowing to conclude that the limits shown in the top right panel of Fig 5.2 are approximately representative for a region with a radius of 1.5 deg centred on the best fit location of GRB 140901A.

GRB 150415A was a mid to long duration burst with $T_{90} = 8\,\mathrm{s}$ detected by *Fermi*-GBM. It was followed up promptly by H.E.S.S. Observations started only 80 s after the detection by *Fermi*-GBM. The localisation was updated, which resulted in a repointing of the H.E.S.S. array after the first 28 minutes of observations. This final position was then observed for the remaining 17 minutes of the night.

The statistical position uncertainty of this burst was larger than in the case of GRB 140901A with a radius of 3.6 deg and exceeded the size of the CT5 field of view. The location was observable for roughly 45 minutes with an average zenith angle of 14 deg, resulting in an energy threshold of ~ 80 GeV. In this case, the best fit spectral model for the burst was a power law, which might be a hint for the synchrotron peak lying at energies well above 1 MeV.

Due to the large coordinate update, the final best fit position was not inside the H.E.S.S. FoV during the first 28 minutes of the observations. Therefore, the upper limit calculation was split into two cases. The first 28 minutes of data were analysed offset from the best fit position while remaining well inside the $1\,\sigma$ uncertainty region of the GBM localisation. The last 17 minutes of data were analysed at the best fit position. The limits obtained in both cases are comparable and on the level of 10^{-10} to $10^{-11}\,\mathrm{erg\,cm^{-2}\,s^{-1}}$.

Summary and Discussion

The observations for all three bursts did not reveal any significant emission in the respective fields of view. The observation triggered by *Swift*-BAT (GRB 140818B) has an accurate enough localisation so that the differential flux upper limits could be calculated at the location of the *Swift*-BAT detection. For GRB 140901A and GRB 150415A, detected by *Fermi*-GBM, the H.E.S.S. field of view only roughly cover the $1\,\sigma$ uncertainty region of the GBM localisation. Therefore the differential flux upper limits at the intersection of both observed fields, as well as at the best fit position of the burst were checked in order to estimate the drop in sensitivity away from the observation axis. The limits for all three observations which are shown in Fig 5.2 [208] can be seen as a benchmark sensitivity that H.E.S.S. obtains for observations under similar observing conditions. The differential flux upper-limits are on the level of 10^{-10} - $10^{-11}\,\mathrm{erg\,cm^{-2}\,s^{-1}}$, depending on the energy. This is several orders of magnitude better than what is achievable with *Fermi*-LAT at these energies. For all three bursts an energy threshold of less then 100 GeV was achieved, which enlarges the redshift horizon to around $z < 1$.

While the delay with which the observations were started with respect to the burst are small compared to the H.E.S.S. I era, they remain significant (see section 3.2). If the previously discussed empirical model for the temporal evolution of the X-ray emission of GRBs is considered, a flux reduction of several orders of magnitude is to be expected. A graphical representation of the temporal evolution model with the respective observation delays is

shown in Fig 5.3, showing that these factors range between 10^{-6} and 10^{-15}. Assuming that this temporal evolution model can be scaled into the 100 GeV range, detections in all three cases would basically be ruled out. In the light of the discussion in section 3.2 the temporal evolution looks much more promising at GeV energies. The *Fermi*-LAT found the emission to be systematically starting delayed and lasting longer at GeV energies compared to X-ray energies. A comparable emission evolution model as used in Fig 5.3 is however not found yet in the GeV energy domain. It is also unclear if this trend extends into the 100 GeV energy range which H.E.S.S.II starts to probe. Most importantly it is not clear if the *Fermi*-LAT findings apply to the whole population of GRBs or just to a small fraction of it. A sizeable number of GRB observations with short delays and low zenith angles is required to evaluate these questions.

5.2 Follow-up of Neutrinos and the Case of IceCube-170922

Several observations were carried out under the neutrino follow-up program described in section 4.2. It aims at searching for TeV γ-ray counterparts to the recently discovered astrophysical neutrino flux. The follow-up observations vary between: i) follow-up campaigns to observe sky regions from which historical[1] neutrino candidate events were observed. These follow-ups aim to search for static γ-ray sources which are responsible for the neutrino flux. ii) follow-up observations with a close temporal relation between the observation and neutrino candidates with an accurate direction reconstruction. This strategy makes use of the time domain by probing for correlated γ-ν flux increases of sources. Schüssler et al. [209] gives an overview of a wider set of recent results. Here the focus will be on the rapid follow-up of neutrino candidates.

To date H.E.S.S. performed follow-up observations of 6 neutrino candidate detection alerts. Two of these were issued by ANTARES. All follow-ups are listed in Table 5.2. This sample features observations with delays ranging from roughly 30 s to more than two days. All observations were carried out with the help of the aforementioned alert system. No significant γ-ray emission was detected in these observations. The sensitivity is naturally comparable to the ones presented for the follow-up of GRBs. The most prominent neutrino candidate is *EHE 170922* which will be discussed in more detail in the following.

IceCube-170922 / TXS 0506+056

The Alert *EHE 170922*, called IceCube-170922 hereafter, triggered the longest follow-up observation based on the detection of a neutrino candidate to date. The follow-up can be separated into two campaigns:
The initial follow-up campaign spanned the usual two hours of observations and was triggered by the detection of the high-energy neutrino candidate event *EHE 170922* by IceCube [211]. The track-like morphology of the candidate event inside the IceCube detector provided a good directional reconstruction with an uncertainty of approximately one degree. The chance of this neutrino being of astrophysical origin opposed to it originating from atmospheric showers was estimate to be on the level of 50 %. The energy of the candidate is not that well reconstructible as the vertex of the neutrino was outside of the instrumented

[1] Historical here means that these neutrino candidates were not identified by means of a real-time analysis pipeline

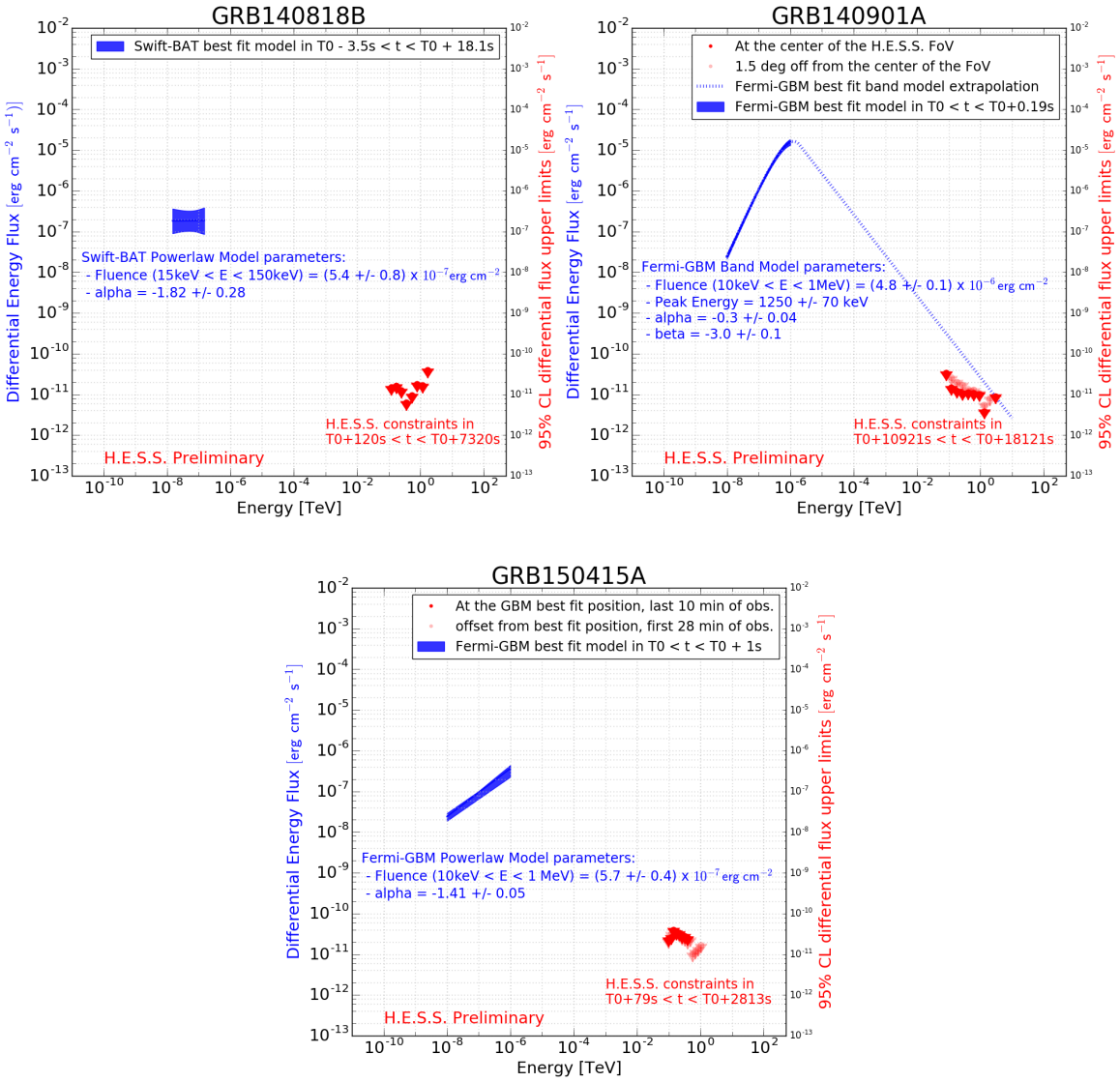

Figure 5.2: The upper limit results obtained from the H.E.S.S. observations for all three bursts (GRB140818B, GRB140901A and GRB150415A) are shown in red. The best fit spectral model for the detection of each burst is shown in blue. For the two observations triggered by *Fermi*-GBM, upper limits obtained offset from the center of the field of view are shown as well.

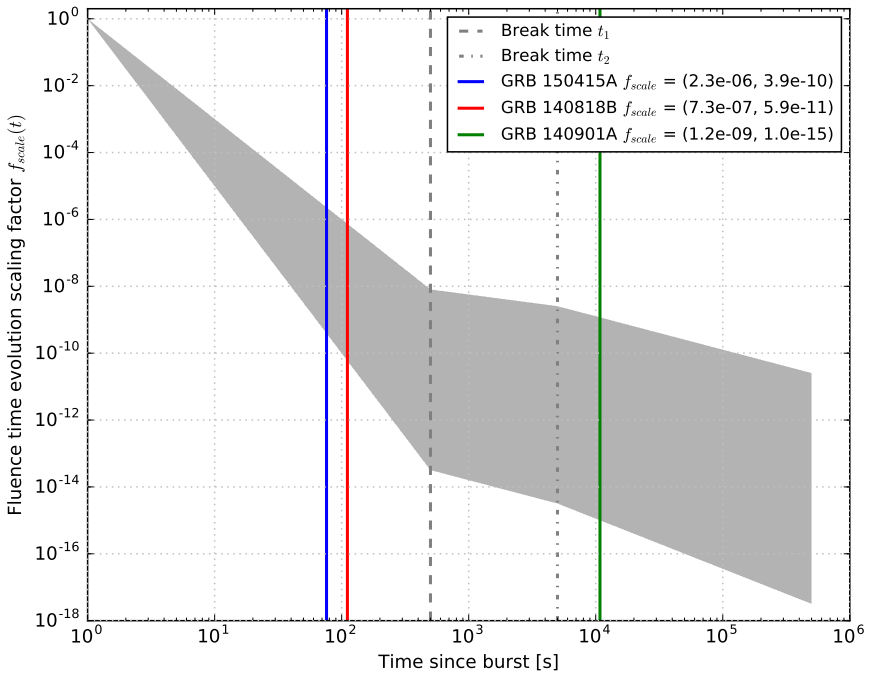

Figure 5.3: The range of the GRB time evolution model described in section 3.2 is shown in grey. The colored bars indicate the different start times of the three presented bursts with respect to $T_{\mathrm{Burst}} + T_{90}/2$, the time after which the X-ray emission starts to decay. The range of the factor by which the X-ray emission supposedly decayed when the observations started is indicated in the legend and ranges between 10^{-6} to 10^{-15}.

Date	Triggering experiment	Alert identifier	Delay of observations	Duration of observations
September 1, 2015	ANTARES	ANT 150901	11h	2h
April 27, 2016	IceCube	HESE 160427	2d 15h	2h
July 31, 2016	IceCube	EHE 160731	16h	2h
November 3, 2016	IceCube	HESE 161103	12h	2h
January 30, 2017	ANTARES	ANT 170130	30s	1h 20m
September 22, 2017	IceCube	EHE 170922	4h	3h 14m

Table 5.2: Summary of neutrino follow-up observations performed by H.E.S.S. EHE-170922 presents the IceCube alert which was followed up with the longest exposure and the shortest delay to date. The long exposure was taken following the Fermi-LAT announcement that the blazar TXS 0506+056 is in a high emission state while being positionally coincident with the neutrino localisation [210]. ANTARES alerts are being communicated privately between the experiments and are therefore not reported on public pages like the GCN.

volume of IceCube. This results in an unknown fraction of energy that was deposited outside of the detector. The best energy estimate is 290 TeV [212]. All three IACTs performed observations towards this sky region shortly after the detection. H.E.S.S. was the first IACT to react with a delay of roughly 4 hours. None of the IACTs detected significant emission at this point [206, 213, 214].
The second campaign was initiated by the announcement by *Fermi*-LAT that the blazar TXS 0506+056 was in a flaring state since April 2017 and is positionally coincident with the neutrino candidate [210]. The flare of this blazar was noted at the time but did not prove to be strong enough to warrant target of opportunity observations on its own. All three IACTs continued their follow-up observations in response to this announcement. H.E.S.S. observed until October 1st, at which point the source location was no longer visible. MAGIC was able to observe the source until October 4th, after which they announced a detection at energies above 90 GeV after in total 13 hours of observations [214]. In contrast, VERITAS announced a non-detection with observations spanning from Sepember 23rd to September 30th at energies above 160 GeV [213].
This event spawned interest beyond the high-energy community in all wavebands as it presents the best indication for an identified neutrino source to date. It clearly highlights the importance of the time-domain in γ-ray astronomy and resulted in an extensive follow-up campaign with more than 10 observatories. The full description of all data can be found in [212]. This paper addresses the question how likely a coincidence between an AGN with a flare strength like the one observed here and such a neutrino candidate event is. In the following, the H.E.S.S. follow-up will be described, followed by a discussion of the chance probability between the AGN and the neutrino.

H.E.S.S. observations of TXS 0506+056

H.E.S.S. accumulated around 10 hours in total towards TXS 0506+056. At the time at which the analysis could be performed, the MAGIC announcement of a detection at E $>$ 100 GeV [214] was already public. Therefore the data was restricted to the periods in which CT5 was available in order to achieve the lowest possible energy threshold. This resulted in 3.25 hours distributed over three nights at zenith angles ranging between 31 and 46 deg, allowing for energy thresholds in the range of roughly 150 GeV. Further monitoring of the sky region was performed since then. This data will not be presented here.

The same analysis prerequisites and steps as outlined in section 1.3 were taken in the analysis of this data. The best fit spectral index of ~ 3.9 measured by MAGIC was used as spectral assumption in the extraction of upper limits. The limits at 95 % confidence level were derived using *TRolke* [215]. Systematic uncertainties in the γ-candidate numbers of 30 % were assumed. Negative excess fluctuations of the measured counts in the *On-region* were avoided by making use of the measured background counts and scaling them to the live-time of the signal region. This avoids limits which would otherwise overshoot the sensitivity of H.E.S.S. The limits and fluxes were calculated for each night of the data set individually and are shown in Fig 5.4 and given in Table 5.3 above the common energy threshold of 175 GeV. Additionally, differential flux upper limits were calculated for the 3.25 h dataset. The differential upper limits of this follow-up as well as the broadband light-curve with observations ranging from Radio to TeV γ-rays can be found in [212].

The limits extracted from the H.E.S.S. and VERITAS observations are not in conflict with the MAGIC detection. Most of the signal of the MAGIC detection has been accumulated

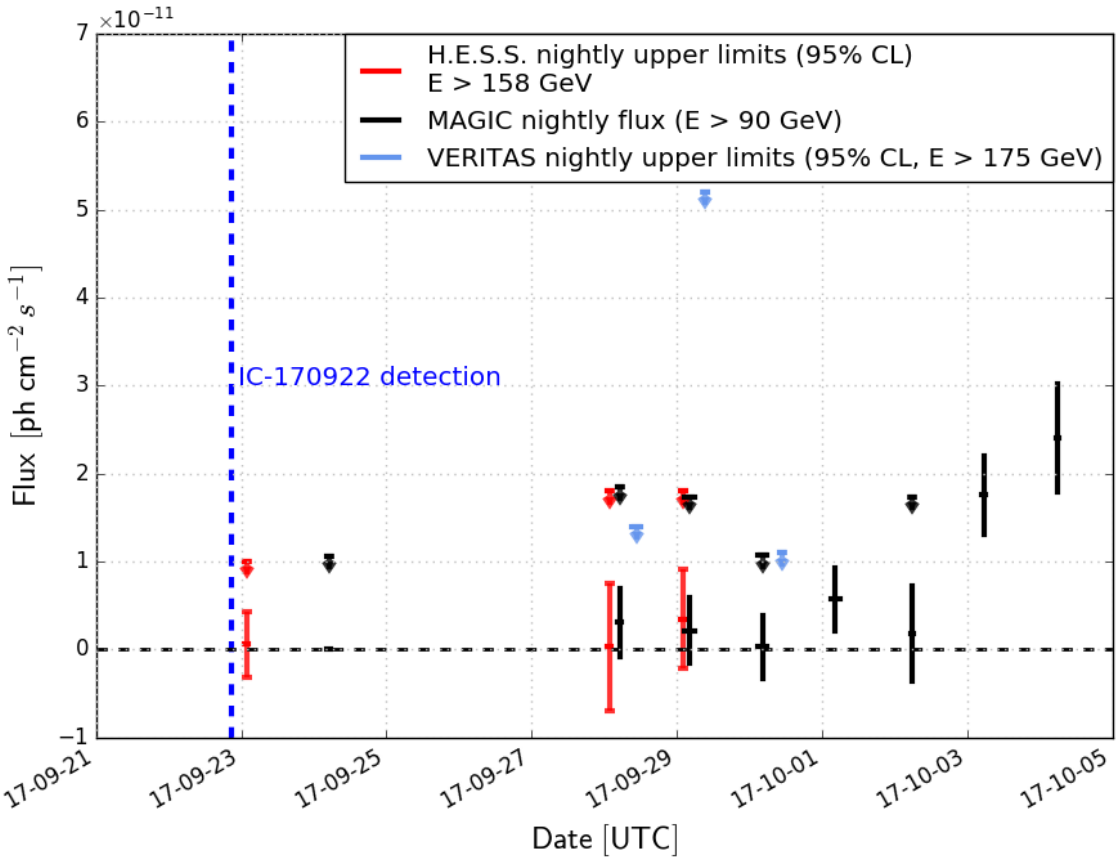

Figure 5.4: Light curve of the VHE γ-ray observations carried out in the follow-up campaign of IC170922/TXS0506+056 by H.E.S.S (red), VERITAS (blue) and MAGIC (black). Note that the measurements are given at different energy thresholds by the different experiments.

in the nights of October 3rd and 4th during which the source location was not observed by H.E.S.S. and VERITAS. The combined VHE γ-ray light curve is shown in Fig 5.4.

Chance coincidence of the neutrino and the flaring blazar TXS 0506+056

AGNs are being discussed as sources of neutrinos since a long time (see e.g. [216]). Drawing a firm connection between the astrophysical neutrino flux and AGNs however presents itself as difficult. Padovani et al. [217] discuss that extreme AGNs might account for a fraction of the neutrino flux, but fail to explain the total neutrino flux level. Individual sources have not yielded a detection of a distinct neutrino source. The time domain therefore offers a new view on the AGN-ν connection by allowing enhanced neutrino production of AGNs in flaring states. The difficulty in this approach lies in the quantification of randomly detecting a neutrino in spatial and temporal coincidence with one of the numerous AGNs. Besides the IceCube-170922/TXS 0506+056 event discussed here, Kadler et al. [218] discussed a coincidence for a similar case of a the blazar PKS B1424-418 flaring in spatial and temporal coincidence with HESE-35. In their paper Kadler et al. build their arguments on the basis of a chance coincidence level of 5 % which was calculated with very specific requirements. As outstanding claims demand outstanding evidence, this 2 σ event is highly debated.

Date	Observation window [UTC]	$dN(E > E_{\mathrm{min}})$ [ph / cm^{-2} s^{-1}]	$dN_{95\,\%\,\mathrm{CL}}(E > E_{\mathrm{min}})$ [ph / cm^{-2} s^{-1}]
September 23, 2017	01:05 - 02:26	$(0.6 \pm 3.7) \times 10^{-12}$	$< 1.0 \times 10^{-11}$
September 28, 2017	01:39 - 02:08	$(0.3 \pm 7.2) \times 10^{-12}$	$< 1.8 \times 10^{-11}$
September 29, 2017	01:12 - 02:51	$(3.5 \pm 5.6) \times 10^{-12}$	$< 1.8 \times 10^{-11}$

Table 5.3: Nightly fluxes and limits for TXS 0506+056 derived from the H.E.S.S. observations assuming an $E^{-3.9}$ energy spectrum above a safe energy threshold of 175 GeV.

E_{min} [TeV]	E_{max} [TeV]	f_γ [cm^{-2} s^{-1} TeV^{-1}]
0.16	0.28	6.6×10^{-11}
0.28	0.48	2.1×10^{-11}
0.48	0.85	4.5×10^{-12}
0.85	1.50	1.8×10^{-12}
1.50	2.63	5.9×10^{-13}
2.63	4.62	3.3×10^{-13}

Table 5.4: Differential γ-ray flux upper limits at 95% confidence level obtained for the full TXS 0506+056 H.E.S.S. data set and assuming an $E^{-3.9}$ energy spectrum.

Here the spatial chance coincidence calculation will be discussed first, followed by considerations for building a temporal coincidence argumentation.

Spatial Chance Coincidence The probability to find a source in spatial coincidence with one neutrino candidate out of N_{Alerts} trials can be calculated as $p_{\mathrm{chance}} = 1 - (1 - N_{\mathrm{sources}} \cdot p_{\mathrm{spatial}})^{N_{\mathrm{Alerts}}}$ where p_{spatial} is the spatial search fraction of the sky given by $PSF^{X\,\%}_{\mathrm{containment}}/4\pi$. In the case of IceCube-170922 these parameters are:

- all 2280 extragalactic *Fermi*-LAT sources as N_{sources},
- the neutrino candidate localisation precision with 90 % (50 %) containment of $PSF^{90\,\%} = 0.97\,\mathrm{deg}^2$ ($PSF^{50\,\%} = 0.15\,\mathrm{deg}^2$) which is specific to the neutrino candidate IceCube-170922.
- the 51 neutrino candidates as N_{Alerts}. This number consists of 41 archival alerts which would have triggered an alert in the case that the real time pipeline system would have been in place at the time. Since this pipeline is in place, 10 neutrino candidate alerts were generated.

Employing these parameters one obtains a chance of 94 % (35 %) to find one source in spatial coincidence with the neutrino candidate.

In order to produce neutrinos at energies above 100 TeV, high-energy hadronic particle populations are vital. Therefore a selected subsample of extragalactic sources which exhibits γ-ray emission at higher energies is a valid choice. Possible samples are e.g. the *Fermi*-LAT 2FHL Catalog with sources detected at γ-ray energies above 50 GeV [219]. In this sample, 299 extragalactic sources are found (including TXS 0506+056). Another choice would be the sources detected in VHE γ-rays [220] in which 75 extragalactic objects are contained. The

extragalactic sky has however not been fully explored by VHE instruments and is limited to close by AGNs due to EBL absorption. Therefore this is not an appropriate choice. Applying 299 potential γ-ray sources to the simple calculation above yields probabilities of 30 % (5.3 %), which is far from being significant.

Considerations for Temporal Coincidence Claims It is clear, that the addition of the temporal coincidence between a flare and the neutrino reduces the number of sources which have to be considered. Especially since not all extragalactic sources have shown to be variable. At the same time, the actual expected timescale for a connection of γ-rays and neutrinos is pretty much unknown and in general different for γ-rays at different energies. AGNs exhibit variability time scales which range between several months and minutes. Explaining this variability with consistent particle populations is challenging for current AGN models. The often observed correlation of X-rays and TeV γ-ray emission in AGN flares lead to the current paradigm favouring leptonic flare models (especially for short time scales). This would rule out any neutrino production in the first place. At the same time Böttcher et al. [221] achieve similar variability time scales in leptonic and hadronic emission scenarios.

In the case of TXS 0506+056 things are even more complicated as different timescales seem to be at play in every energy band: The HE-γ-ray flare which lasted several months on a rather stable level, while the VHE γ-ray flare was detected with a delay of 9 days with respect to the neutrino. This delay makes any claim of temporal coincidence between the neutrino, the HE-γ-ray flare and the VHE γ-ray flare difficult. More importantly the broad-band SED and its temporal evolution will be key to disentangle hadronic and leptonic components. Gao et al. [222] explore such models for a different AGN, finding that the leptonic component can be dominant while still predicting a measurable level of neutrinos requiring only a weak temporal link between the AGN flare and the neutrino. Gao et al. found the VHE and X-ray fluxes to be most constraining for the hadronic component. Time dependent modelling of AGN flares in lepto-hadronic scenarios is very difficult and has many free parameters. Advancing these models can only be achieved with more contemporaneous data in all wavelengths of AGNs. Such data should be obtained also in the absence of a neutrino candidate.

IceCube-170922 Specific Discussion [212] explore a complex likelihood approach including both the spatial and temporal correlation. The spatial correlation is taken into account using the full reconstruction uncertainty profile. The temporal correlation is based on the light curves of all 2280 extragalactic *Fermi*-LAT sources. Background neutrino candidates are taken from the IceCube neutrino Monte Carlo. In this framework the following question is addressed: how likely is it to find a source which is flaring as strongly as TXS 0506+056 between April and September 2017 in spatial and temporal coincidence with one out of 51 neutrino candidate alerts? With this complex procedure a random coincidence of *this* flare with *this* neutrino candidate can be excluded on the 3 sigma level while many model dependent assumptions as outlined before have to be included.

To prove a connection between AGN flares and neutrinos, additional occurrences are needed. In order to claim the connection, a model with very limited and generic γ-ray to neutrino connection should be the test hypothesis. In this regard the tested scenarios in IceCube Collaboration et al. [212] include many assumptions which are directed at this

exact case rather than a general connection claim. Further follow-up observations of neutrino candidates will be very valuable to address if neutrinos and AGN flares are indeed connected.

Conclusion and Outlook

The case of IceCube-170922 demonstrates the importance of neutrino candidate follow-up campaigns. Especially the rapid follow-up and monitoring of neutrino candidate regions seems to provide fruitful datasets and allows to push the discussion of neutrino sources to a new level of detail. With more such events and extensive multi-wavelength follow-up campaigns, a connection of AGN flares and astrophysical neutrinos might be achievable in the future.

As this one event is not sufficient to claim a connection of flaring AGNs with the astrophysical neutrino flux, more contemporaneous data is needed across the messengers and wavelengths. Detailed time-dependant lepto-hadronic flare models need to be explored to build the grounds for the solid foundation for our understanding of a potential AGN-ν connection.

The fact that MAGIC detected a flare only 9 days after the neutrino event also proves the need to extend follow-up campaigns to longer time scales with potentially shorter exposures. To address these tasks, systems like the one developed as part of this work and described in section 4.3 are vital.

This case also presented a need for more functionality in transients alert systems. While the emission state of the TXS 0506+056 was announced to be enhanced already in April, none of the observatories performing follow up observations as a reaction to the IceCube alert took this into account initially. Factoring the history of transient alerts into the reaction scheme to new transient alerts will surely turn out very beneficial for future alerts.

In the bigger context of neutrino candidate follow-up observations it is also important to note that CT5 will remain the largest Cherenkov telescope with the lowest energy threshold for many years to come on the Southern hemisphere. A continued operation of H.E.S.S. into the CTA era would therefore allow to follow-up neutrino candidates with low latency and low energy-threshold.

5.3 Follow-up of Gravitational Waves and the Case of GW 170817

The advent of Gravitational Wave astronomy is undoubtedly one of the major breakthroughs of the past few years for all branches of modern astronomy. Gravitational waves have broad connections to many branches of astrophysics and cosmology. The field of γ-ray astronomy does not remain unaffected by this new branch of astronomy.

As described in section 3.4 there are long postulated connections between the mergers of neutron stars and short GRBs. Gravitational wave measurements allow for precise mass estimation of the merging compact objects. Therefore black holes and neutron stars can be separated very efficiently. LIGO/VIRGO have detected several mergers of two black holes. In August 2018 the first merger of two neutron stars was measured: GW 170817 [223].

The GW follow-up program of H.E.S.S. described in section 4.2 was set up in advance of the 2017 observation run of LIGO and incorporated into the H.E.S.S. transients alert system. The H.E.S.S. follow-up observations of the *golden binary* [224] were part of the largest world wide MWL follow-up campaigns to date. This case will be discussed in more detail in the following. The full description of the H.E.S.S. follow-up can be found in Abdalla et al. [225].

GW 170817

Chain of events

The Gravitational Wave event GW 170817 was detected at 12:41:04 UTC on August 17, 2017 by the Advances LIGO and Advanced Virgo interferometers [223]. The BAYESTAR real-time analysis pipeline [175] identified it to be best described by the coalescence of a binary neutron-star merger. The follow-up observatories including H.E.S.S. were informed 27 minutes after the event. At this stage the event localisation spanned 24.200 deg^2 (90% containment), roughly 60 % of the entire sky. The localisation was based only on the LIGO Hanford instrument due to a noise artefact in the Livingstone LIGO instruments data.

Fermi-GBM detected the gamma ray burst GRB 170817A only two seconds after the GW detection [226]. The temporal evolution of the burst identified it as a short and weak burst with a duration of 2 seconds, a duration in the transition regime between short and long bursts. This burst was localised to a sky region larger than 10 degrees in radius (68 % containment).

At 17:54:51 UTC an updated GW probability map was provided which now included data from both LIGO Hanford and Livingstone instruments as well as from the Virgo instrument [227] (BAYESTAR_HLV). This improved the localisation to a region of only 31 deg^2, confirmed the binary neutron star hypothesis and located the merger event at a distance of 40 ± 8 Mpc. This relatively small region overlapped with the localisation of GRB 170817A and is shown in Fig 5.5.

10.87 hours after the initial detection of GW 170817 the One-Meter Two-Hemisphere (1M2H) collaboration detected a counterpart in near-infrared with the 1 m Swope telescope at Las Campanas Observatory in Chile. This counterpart was found to be near the early-type galaxy NGC 4993 which has a measured distance of 42.5 Mpc and got the Swope Supernova Survey identifier SSS17a. The optical transient was independently detected by five additional teams (see [228], [229], [230], [231] and [232]). The first counterpart detection in X-rays was achieved by Chandra roughly 9 days after GW 170817 [233]. A radio counterpart was identified on September 2-3 by the Jansky VLA [234, 235]. The identification of SSS17a allowed to focus all further follow-up observations on the counterpart across the EM spectrum, which is still ongoing to date. The broandband emission seen is found to be consistent with a blue kilonova [158].

H.E.S.S. follow-up of GW170817

Follow-up strategy The BAYESTAR_HLV map presents the most precise GW localisation to date. Still it spans multiple fields of view of H.E.S.S. In order to scan the uncertainty region efficiently and maximize the chances that the observations cover regions of potential counterparts two algorithms are used. They make use of the localisation probability maps as well as the GLADE galaxy catalogue [236], which was specifically build for the EM follow-up of GW signals. It includes more than 3 million galaxies and is complete outside of the Galactic plane up to roughly 70 Mpc. The general procedure follows the one outlined by Singer et al. [237]. Specifics on the procedures can be found in [188]. The general concept is the optimisation of the number of galaxies, the fractional coverage of the GW localisation uncertainty region and the observability of the sky region as a function of time. This results in an optimised scanning pattern of the sky region of interest. As H.E.S.S. receives a GW alert, this pattern is calculated automatically and communicated to experts and the shift-crew.

Obtained data The obtained observations are summarized in Table 5.5. During the first night of H.E.S.S observations the counterpart SSS17a was not yet identified. This lead to the observations being distributed across the localisation uncertainty region as given by pointings 1a-c which are illustrated in Fig 5.5. The counterpart SSS17a was in the field of view in pointing 1a. This presents the earliest ground based pointed observations towards SSS17a after the NS-NS merger. The rest of the follow-up campaign concentrated on the counterpart and was continued until September 22 (pointing 6a). The source location was no longer visible from the H.E.S.S. site after that night.

Table 5.5: H.E.S.S. follow-up observations of GW 170817. All pointings were taken with the default run duration of 28 min.

ID	Observation time (UTC)	Pointing coordinates [deg]	<zenith angle> [deg]
1a	2017-08-17 17:59	196.88, -23.17	59
1b	2017-08-17 18:27	198.19, -25.98	58
1c	2017-08-17 18:56	200.57, -30.15	62
2a	2017-08-18 17:55	197.75, -23.31	53
2b	2017-08-18 18:24	197.23, -23.79	60
3a	2017-08-19 17:56	197.21, -23.20	55
3b	2017-08-19 18:24	197.71, -23.71	60
5a	2017-08-21 18:15	197.24, -24.07	60
6a	2017-08-22 18:10	197.70, -24.38	60

Analysis and Results The data obtained towards SSS17a was analysed night by night using the model analysis framework [43] with all prerequisites described in section 1.3. Events were reconstructed in monoscopic mode using information only from CT5. The 'loose' cut configuration was used to allow for a relatively low energy-threshold of $\approx$ 240 GeV, regardless of the large zenith angles of the observations (see Table 5.5). Significance maps were derived using the ring background method [46] for the first night individually (see Fig 5.5) as well as for all data combined as depicted in Fig 5.7. Although there are several sources in the sky region covered in the H.E.S.S. follow-up that are known γ-ray emitters in the GeV energy range, none of them is known to emit γ-rays in the VHE γ-ray energy range. The most prominent candidate for emission into the TeV energy range is PKS 1309-216, which is located at an angular distance of 1.6 deg from SSS17a. To avoid potential influence of this source in the background estimation, a circular region with a radius of 0.1 deg around the position of PKS 1309-16 was excluded from the analysis. The analysis did not find any significant γ-ray emission from the direction of SSS17a in both cases.

Using the γ-ray statistics obtained with the multiple-off background estimation, upper limits were derived at a confidence level of 95 % assuming a generic power-law with index -2. Integral upper limits for each night are shown in Fig 5.6 as well as in Table 5.6. The EBL effect was evaluated using the model of A. Franceschini et al. [238] assuming NGC 4993 being the host galaxy ($z = 0.0009787$ [239]). The correction factors increase with energy from 10 % at 1 TeV to roughly 30 % at 10 TeV and are thus negligible as the statistics at these energies are marginal due to the short exposures and the monoscopic analysis. γ-ray

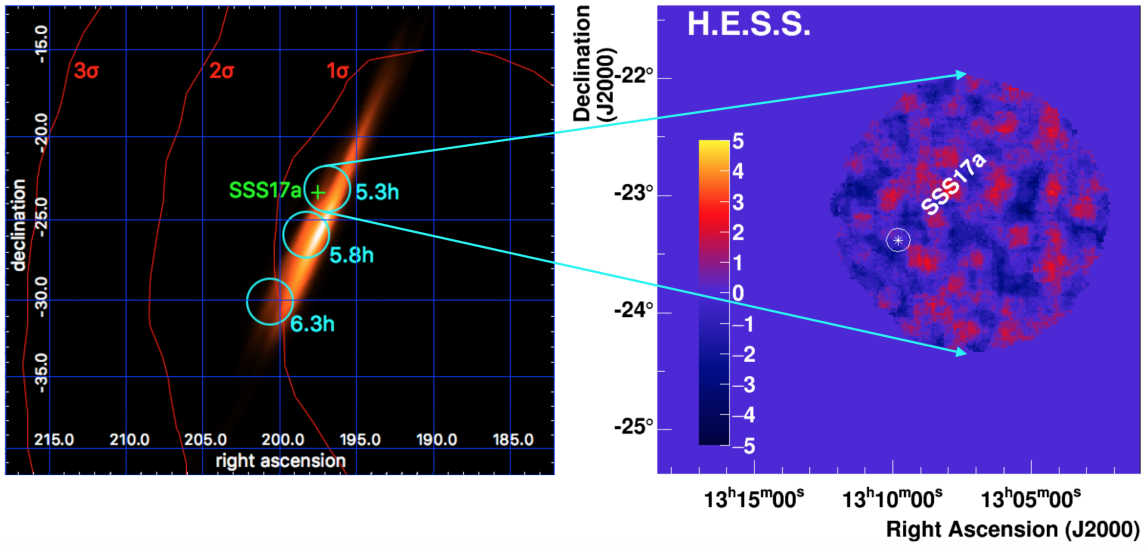

Figure 5.5: Left: pointing positions of the H.E.S.S. GW 170817 follow-up campaign from the first night. The delay with respect to the merger as well as the positions are indicated by the circles. SSS17a marks the later identified counterpart of the gravitational wave. The color map indicates the localisation uncertainty provided by LIGO/Virgo (BAYESTAR_HLV. The red rings show the GRB 170817 localisation uncertainty regions for 1, 2 and 3 σ containment. Right: significance distribution of the first observation run which covered the position of SSS17a.

emission in the time range from 0.22 days to 5.23 days after the NS-NS merger is excluded at the level of $\sim 3 \times 10^{-12}\,\mathrm{erg\,cm^{-2}\,s^{-1}}$ level at energies above $\sim$ 300 GeV.

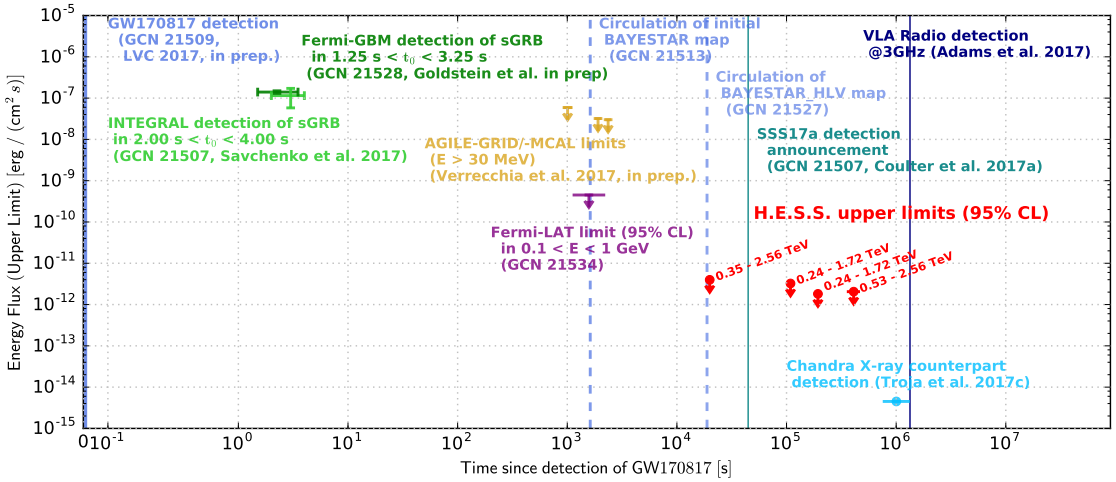

Figure 5.6: Lightcurve illustrating the chain of events. Times are given for the circulation of the updated localisation information on the GW event as well as the different counterpart detection times. The integral energy flux limits from H.E.S.S. observations are depicted in red.

Table 5.6: Limits on the high-energy gamma-ray flux obtained during the monitoring of SSS17a with H.E.S.S.

pointings (see Tab.5.5)	time since GW trigger [days]	f_γ [erg/cm^2/s]	Energy band [TeV]
1a	0.22	$< 4.0 \times 10^{-12}$	$0.35 - 2.56$
2a+2b	1.22	$< 3.2 \times 10^{-12}$	$0.24 - 1.72$
3a+3b	2.22	$< 1.8 \times 10^{-12}$	$0.24 - 1.72$
5a+6a	4.23+5.23	$< 2.1 \times 10^{-12}$	$0.53 - 2.56$
all	0.22 – 5.23	$< 1.6 \times 10^{-12}$	$0.24 - 10.0$

Discussion and outlook

The successful follow-up of GW 170817 presents the first VHE γ-ray observations of a proven NS-NS merger. The importance of this still evolving transient event depends on the classification and the rate of the class. Evaluating this rate itself is quite difficult, as the nature of the GRB is still being debated: With the distance of 40 Mpc GRB 170817 is the closest GRB detected to date. At the same time it just barely triggered *Fermi*-GBM with a significance of just $\sim 6\,\sigma$. The duration of 2 seconds puts it into the transition region between the short and long GRB populations. Also the resulting object class is not distinguished, as the mass is exactly at the transition mass between neutron stars and black holes. A plausible conclusion

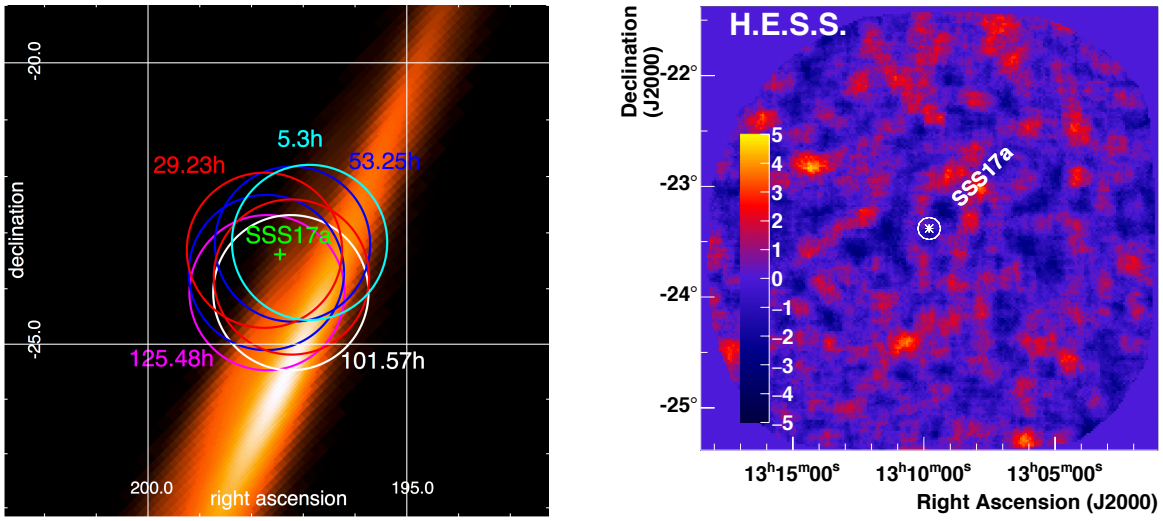

(a) SSS17a: H.E.S.S. pointings

(b) SSS17a: H.E.S.S. significance map

Figure 5.7: Left plot: H.E.S.S. pointing directions during the monitoring campaign of SSS17a. For details see Tab. 5.5. The circles denote a FoV with a radius of 1.5 deg and the shown times are the start times of each observation with respect to the detection of GW170817. Right plot: Map of significances of the gamma-ray emission in the region around SSS17a combining all observations obtained during the H.E.S.S. monitoring campaign.

is to categorise GRB170817 as sub-luminous event. This is however a not well established class of GRBs.

Currently, the most debated scenarios try to interpret GRB 170817 with different models for the relativistic outflow. In the description of jets a top-hat distribution of the Lorentz factor in the outflow is commonly used. This scenario can explain GRB 170817 in the case that it is observed with a relatively large off-axis angle. A more complex scenario allows for structure in the angular distribution of the outflows Lorentz factor. This can be motivated by the outflows propagation trough the neutron rich environment of the immediate merger environment. This is called the structured jet scenario. Margutti et al. [240] discuss these two scenarios and concluded, that both explanations are currently possible without the need to open a new non-thermal and roughly spherical transient class.

The temporal spectral evolution of the emission in radio and X-rays (as well as potentially TeV γ-rays) might be able to distinguish between the two cases over the course of the surprising evolution of the afterglow emission. Currently both the radio and X-ray emission continue to rise with a temporal behaviour following $\sim t^{0.7}$ [240] resulting in a brightening of a factor 5 within 100 days since the merger. In case that both components are originating from synchrotron emission, an Inverse Compton component reaching into the sensitivity range of H.E.S.S. could be present. As GW 170817 is located in the Southern hemisphere, H.E.S.S. will be the only instrument sensitive enough to follow the event and monitor the γ-ray emission in the coming years.

Shortly after the detection of GW 170817 the second observation run of LIGO/Virgo concluded. The next run is scheduled to start in fall 2018 with increased sensitivity for both LIGO instruments as well as the Virgo instrument, which joined the previous run mostly

for commissioning reasons shortly before the end of the observation run in 2017. Many new Gravitational Wave detections are anticipated. The successful follow-up campaign of GW 170817 proved that the current algorithms provide suitable follow-up strategies. While the observation schedule is derived largely automatically, such follow-up campaings would greatly benefit from more automation by reducing the chances for human mistakes in the scheduling. Here, the success of this follow-up was only possible due to the careful execution of the requested observations by the shift crew in Namibia. Functionalities to enable such follow-up campaigns automatically are mandatory for CTA.

5.4 Conclusions and Outlook

The observational results presented here were acquired with the help of the transient alert system which was developed as part of this thesis. The broad variety of transients that were observed is a clear success. Increased collaboration between different branches of astronomy and infrastructures would enrich time-domain astronomy for all participants. Large sets of contemporaneous data have shown to challenge our current understanding of transient phenomena.

The growing sample of GRBs observed with low energy-threshold and short delays will prove very helpful for constraining the class of GeV γ-ray emitting GRBs. With larger and larger numbers of non-detections of GRBs at 100 GeV, the common perception (in the TeV community) that a high-energy component is common to all GRBs might have to be revised.

Especially the scientific collaboration with the two new branches of astronomy, namely neutrino and gravitational waves, allowed for exciting observations. IACTs like H.E.S.S. II sit in a phase space that is able to provide key insights into the nature of the phenomena both with regards to tracking hadronic components in AGN flares and in searching for inverse Compton emission in kilonova afterglows.

The follow-up of neutrino candidates and gravitational wave events are strong science cases to argue in favour of a continued operation of H.E.S.S. beyond 2020. While the Northern site of CTA will be in operation at this time, there will be no other IACT with comparable sensitivity down to below 100 GeV other than H.E.S.S. Much of the transient follow-up procedures have been automised which should allow to carry out transient follow-up programs with a reduced collaboration in the future.

Chapter 6

Summary & Outlook

Summary

This work briefly summarised the rapid development of γ-ray astronomy to the current generation of experiments. Novel astrophysical messengers have entered the field in the last few years with the advent of both neutrino and gravitational wave astronomy, marking the birth of multi-messenger astronomy. This development allows for more complex studies involving no longer only the full range of the electromagnetic spectrum in multi-wavelength studies. H.E.S.S. is therefore faced with new opportunities and challenges in this rapidly evolving field.

In this work, two very different scientific topics were discussed in which both the multi-wavelength and multi-messenger approach has been applied: i) Inferring the cosmic-ray flux in the starburst galaxy NGC 253 from γ-ray observations in comparison to the physical conditions inferred from radio, near-infrared and X-ray observations, and ii) extending the H.E.S.S. transients observation programs further into the time-domain with the addition of neutrinos and gravitational waves as new messengers.

As an example of a classic multi-wavelength study, data from observations with H.E.S.S. towards the starburst galaxy NGC 253 (currently the faintest γ-ray source at TeV energies) has been reanalysed. Thanks to the improved understanding of the dataset, the systematic uncertainties of this measurement no longer dominate the measurements precision. The γ-ray spectrum was discussed under the assumption that it originates from hadronic interactions of cosmic rays and allowed for the discussion of different cosmic-ray escape scenarios. Employing measurements of the system in radio emission, near infrared radiation and X-rays, a theoretical range of the cosmic-ray flux in NGC 253 has been calculated. The γ-ray flux traces the part of the cosmic-ray spectrum which is absorbed in the galaxy itself through hadronic interactions. The updated measurements indicate that this level of calorimetric absorption of cosmic rays lies in the range from 10 % to the calorimetric limit of 100 %. This highlights, that a large fraction of the energy density in cosmic rays, which lies in the order of 10^{41} erg, is being fed back into the system. This result is not only important as a potential influencing factor to the overall evolution of starburst systems, but also enables further discussion about starburst galaxies as potential sources of neutrinos and ultra-high-energy cosmic rays.

The time-domain of high energy multi-messenger events is promising plentiful scientific rewards. In order to probe more such events with H.E.S.S., a new transients alert system has been developed as a part of this work. It enables to follow-up on all detections of

transients from any wavelength or messenger, including neutrinos and gravitational waves. An increased activity in this field with Cherenkov telescopes presents a paradigm shift, as larger amounts of observation time needs to be accounted for unpredictable events. In order to exploit the time-domain as much as possible, the fifth telescope (CT5) has been added to the H.E.S.S. array in 2012, which allows to repoint faster and has a lower energy threshold compared to the smaller telescopes (CT1-4). Further challenges are present in the reaction scheme of the array to transient alerts and have been discussed based on Gamma Ray Bursts as an exemplary transient target phenomenon. The new transients alert systems design, functionality and performance has been described. It was shown, that the system allows for fully automated observations with an average delay with respect to the transient of less than 100 seconds. The 100 seconds mark was shown to be a sum from spacecraft constraints and the H.E.S.S. performance, with a baseline of 15-50 seconds response without the slewing time. A wide array of transient targets will be studied with this system in the future, among which are Gamma Ray Bursts, astrophysical high energy neutrinos and gravitational waves. New exploratory observations can easily be incorporated into this system.

Utilising H.E.S.S. II with the new transient alert system, several interesting follow-up observations were performed. A selection of highlights were analysed as part of this thesis. The importance and implications of the derived results were discussed:

- Gamma-Ray Burst follow-up observations with delays below 100 seconds and energy thresholds in the order of 100 GeV: The limits from these observations can be taken as a benchmark for future GRB observations under similar observation conditions. With the current performance, H.E.S.S. might be able to probe into the high-energy γ-ray emitting population of GRBs or put stringent constraints on the rate of such GRBs.

- Neutrino candidates are followed up with observations by H.E.S.S. regularly. One especially interesting case was the neutrino candidate IceCube-170922 which was found to be spatially coincided with the flaring blazar TXS 0506+056. While H.E.S.S. was unable to detect γ-rays from this blazar, MAGIC was able to detect a flare with a delay of 9 days with respect to the neutrino candidate arrival time. A potential association of the neutrino with the blazar was discussed. Establishing a firm connection between flaring blazars and neutrinos in general is currently limited by the rarity of such coincidences. This work proved that H.E.S.S. is prepared to participate in more contemporaneous follow-up campaigns.

- Finally, this thesis reported on the successful participation in the multi-messenger observation campaign to search for a counterpart of Gravitational Waves with H.E.S.S. In the neutron star neutron star merger event GW170817 which was accompanied by a Gamma Ray Burst, H.E.S.S. was observing the sky location of the counterpart as the first ground-based pointing instrument, thanks to the reaction scheme implemented in the alert system. While no TeV γ-ray counterpart could be identified, the readiness of H.E.S.S. to take part in the multi-messenger era of astronomy has been demonstrated.

All three cases demonstrate that H.E.S.S. is pushing to new frontiers in multi-messenger γ-ray observations. Many lessons can be learned from the observations that were presented here. They will provide important knowledge for the realisation of improved and more complex programs with the upcoming Cherenkov Telescope Array.

Outlook

A glimpse into the future of γ-ray astronomy shows the Cherenkov Telescope Array (CTA), with 120 telescopes distributed over two sites. With a factor ten increase in sensitivity and a factor two to five improved angular resolution, CTA will undoubtedly improve in basically all aspects of γ-ray astronomy. This also applies to the topics covered in this work.

CTA will probe γ-rays from starburst systems, bringing improvements in the case of NGC 253 and starburst galaxies in general. Thanks to the improved sensitivity at high energies, CTA will likely be able to see a deviation from a single power-law at the very-high-energy end of the NGC 253 γ-ray spectrum. A major study will be the identification of the origin of such a cutoff. Either γ-γ absorption attenuates the γ-ray flux or the number of individual sources in the starburst nucleus which are able to accelerate cosmic rays to such high energies starts to shrink. Similar studies will be able to be performed with many other objects: M82, the Northern counterpart to NGC 253; Arp220, an ultra luminous infrared galaxy with an even stronger star-forming activity compared to NGC 253; NGC 4945 and NGC 1068, two Seyfert galaxies with starburst activity. While all these objects are detected at GeV energies by *Fermi*-LAT, they were not yet detected in VHE γ-rays. With detections of all these objects, CTA will effectively open the view on star-forming galaxies as a population at VHE γ-ray energies in contrast to the current picture, which is limited by our knowledge of NGC 253 and M82.

Gaining more knowledge about starburst galaxies with H.E.S.S. in the future can only be achieved at the cost of unreasonable amounts of observation time. This is however not the case for multi-messenger transients. Unfortunately, all observations of transients presented here did not yield a detection. Still it demonstrated the readiness of H.E.S.S. to perform such observations on a regular basis. Either during the upcoming observation runs of the gravitational wave detectors LIGO, VIRGO and KAGRA or in the case of the next detection of a neutrino candidate.

As the sample of high-quality Gamma Ray Burst observations with low-energy thresholds and short delays grows, the frequency of high-energy γ-ray components in Gamma Ray Bursts might be probed in the future. In addition, many more transient science cases are expected to emerge due to large infrastructures, such as SKA, going online soon. The new observatories will reveal key information on Fast Radio Bursts and hopefully many more transients. New follow-up chances in the γ-ray band, which are currently considered to be exotic, will be established.

With two sites, larger field of views, lower energy thresholds and an even faster reaction time, CTA is likely to detect Gamma Ray Bursts. The rate at which detections are achieved will greatly improve our knowledge of all physics processes involved in such phenomena.

The lesson from the neutrino follow-up of IceCube-170922 is**,** that potential neutrino sources are not required to be detected in a perfect temporal coincidence between a γ-ray flare and a neutrino candidate. Optimising the follow-up of such events will be a future challenge. Contemporaneous multi-wavelength data is of great importance to increase our understanding of the temporal evolution of potential neutrino sources. This will require better coordination not only between the different γ-ray experiments. Optical and X-ray data is just as important in this endeavour which highlights an improved coordination beyond the γ-ray community.

The full exploitation of Gravitational Waves as a new messenger will only be possible in the coming years. With increased detection rates and improved localisation uncertainties,

suitable follow-up strategies will have to be adapted to the growing performance of LIGO and VIRGO. The upcoming observation runs of LIGO and VIRGO will also reveal the uniqueness of the neutron star merger GW170817.

Probing the time-domain of various variables and transient phenomena, H.E.S.S. is currently performing exploratory observations which CTA will be able to build upon. With H.E.S.S. being located in the Southern hemisphere, the different transients science cases present a strong argument to continue H.E.S.S. operations into the CTA era. As CT5 will remain the largest Cherenkov Telescope, H.E.S.S. will still be able to provide compelling results even when CTA exists. With the first prototype of the large telescopes of CTA currently being build on the Northern CTA site, CT5 will remain unchallenged well beyond 2022. With CTA south operating in Chile, the temporally shared night sky will still be limited. At the same time, H.E.S.S. will share major fractions of the night sky with SKA. This could be exploited in numerous contemporaneous observation campaigns, which may reveal currently unexplored synergies between the radio and γ-ray energy bands.

Bibliography

[1] Victor Francis Hess. Über beobachtungen der durchdringenden strahlung bei sieben freiballonfahrten. *Phys. Z.*, 13:1084–1091, 1912.

[2] W Kraushaar, GW Clark, G Garmire, H Helmken, P Higbie, and M Agogino. Explorer XI Experiment on Cosmic Gamma Rays. *The Astrophysical Journal*, 141:845, 1965.

[3] Ray W Klebesadel, Ian B Strong, and Roy A Olson. Observations of gamma-ray bursts of cosmic origin. *The Astrophysical Journal*, 182:L85, 1973.

[4] GW Clark, GP Garmire, and WL Kraushaar. Observation of high-energy cosmic gamma rays. *The Astrophysical Journal*, 153:L203, 1968.

[5] GJ Fishman, CA Meegan, TA Parnell, RB Wilson, W Paciesas, JL Mateson, TL Cline, and BJ Teegarden. Burst and Transient Source Experiment (BATSE) for the Gamma Ray Observatory (GRO). 1985.

[6] V Schonfelder, R Diehl, GG Lichti, H Steinle, BN Swanenburg, AJM Deerenberg, H Aarts, J Lockwood, W Webber, J Macri, et al. The imaging compton telescope comptel on the gamma ray observatory. *IEEE Transactions on Nuclear Science*, 31 (1):766–770, 1984.

[7] AF Iyudin, R Diehl, GG Lichti, V Schönfelder, H Steinle, H Bloemen, W Hermsen, C de Vries, D Morris, J Ryan, et al. COMPTEL observations of 44Ti gamma-ray line emission from Cas A. In *AIP Conference Proceedings*, volume 304, pages 156–160. AIP, 1994.

[8] DJ Thompson, DL Bertsch, CE Fichtel, RC Hartman, R Hofstadter, EB Hughes, SD Hunter, BW Hughlock, G Kanbach, DA Kniffen, et al. Calibration of the energetic gamma-ray experiment telescope (EGRET) for the Compton gamma-ray observatory. *The astrophysical Journal supplement series*, 86:629–656, 1993.

[9] RC Hartman, DL Bertsch, SD Bloom, AW Chen, P Deines-Jones, JA Esposito, CE Fichtel, DP Friedlander, SD Hunter, LM McDonald, et al. The third EGRET catalog of high-energy gamma-ray sources. *The Astrophysical Journal Supplement Series*, 123(1):79, 1999.

[10] WB Atwood, Aous A Abdo, M Ackermann, W Althouse, B Anderson, M Axelsson, L Baldini, J Ballet, DL Band, Guido Barbiellini, et al. The Large Area Telescope on the Fermi gamma-ray space telescope mission. *The Astrophysical Journal*, 697(2):1071, 2009.

[11] Charles Meegan, Giselher Lichti, PN Bhat, Elisabetta Bissaldi, et al. The Fermi gamma-ray burst monitor. *The Astrophysical Journal*, 702(1):791, 2009.

[12] The Fermi-GBM Collaboration. Localization of Gamma-Ray Bursts using the Fermi Gamma-Ray Burst Monitor. 11 2014. URL `https://arxiv.org/abs/1411.2685`.

[13] W Galbraith and JV Jelley. Light pulses from the night sky associated with cosmic rays. *Nature*, 171:349–350, 1953.

[14] A Michael Hillas. Cerenkov light images of EAS produced by primary gamma. In *International Cosmic Ray Conference*, volume 3, 1985.

[15] Trevor C Weekes, MF Cawley, DJ Fegan, KG Gibbs, AM Hillas, PW Kowk, RC Lamb, DA Lewis, D Macomb, NA Porter, et al. Observation of TeV gamma rays from the Crab nebula using the atmospheric Cerenkov imaging technique. *The Astrophysical Journal*, 342:379–395, 1989.

[16] F Aharonian et al. The Crab nebula and pulsar between 500 GeV and 80 TeV: observations with the HEGRA stereoscopic air Cerenkov telescopes. *The Astrophysical Journal*, 614(2):897, 2004.

[17] TC Weekes, H Badran, SD Biller, I Bond, S Bradbury, J Buckley, D Carter-Lewis, M Catanese, S Criswell, W Cui, et al. VERITAS: the very energetic radiation imaging telescope array system. *Astroparticle Physics*, 17(2):221–243, 2002.

[18] Daniel Ferenc, MAGIC collaboration, et al. The MAGIC gamma-ray observatory. *Nuclear Instruments and Methods in Physics Research Section A: Accelerators, Spectrometers, Detectors and Associated Equipment*, 553(1-2):274–281, 2005.

[19] James Anthony Hinton, Hess Collaboration, et al. The status of the HESS project. *New Astronomy Reviews*, 48(5):331–337, 2004.

[20] Hidetoshi Kubo, A Asahara, GV Bicknell, Roger W Clay, Y Doi, PG Edwards, R Enomoto, S Gunji, S Hara, T Hara, et al. Status of the CANGAROO-III project. *New Astronomy Reviews*, 48(5):323–329, 2004.

[21] BS Acharya, M Actis, T Aghajani, G Agnetta, J Aguilar, F Aharonian, Marco Ajello, A Akhperjanian, M Alcubierre, J Aleksić, et al. Introducing the CTA concept. *Astroparticle physics*, 43:3–18, 2013.

[22] H Abdalla, A Abramowski, F Aharonian, F Ait Benkhali, EO Angüner, M Arakawa, M Arrieta, P Aubert, M Backes, A Balzer, et al. The HESS Galactic plane survey. *Astronomy & Astrophysics*, 612:A1, 2018.

[23] Amanda Weinstein et al. The VERITAS Survey of the Cygnus Region of the Galactic Plane. *arXiv preprint arXiv:0912.4492*, 2009.

[24] Diffuse galactic gamma-ray emission with hess. *Physical Review D*, 90(12):122007, 2014.

[25] H Abdalla, A Abramowski, F Aharonian, F Ait Benkhali, AG Akhperjanian, T Andersson, EO Angüner, M Arrieta, P Aubert, M Backes, et al. The population of TeV pulsar wind nebulae in the HESS Galactic Plane Survey. *Astronomy & Astrophysics*, 612:A2, 2018.

[26] The H.E.S.S. Collaboration. Population study of Galactic supernova remnants at very high *gamma*-ray energies with H.E.S.S. *arXiv preprint arXiv:1802.05172*, 2018.

[27] Mathieu De Naurois. *Very High Energy astronomy from HESS to CTA. Opening of a new astronomical window on the non-thermal Universe*. PhD thesis, Université Pierre et Marie Curie-Paris VI, 2012.

[28] Dieter Heck, G Schatz, J Knapp, T Thouw, and JN Capdevielle. CORSIKA: A Monte Carlo code to simulate extensive air showers. Technical report, 1998.

[29] MP Kertzman and GH Sembroski. Computer simulation methods for investigating the detection characteristics of TeV air Cherenkov telescopes. *Nuclear Instruments and Methods in Physics Research Section A: Accelerators, Spectrometers, Detectors and Associated Equipment*, 343(2-3):629–643, 1994.

[30] Heinrich J Völk and Konrad Bernlöhr. Imaging very high energy gamma-ray telescopes. *Experimental Astronomy*, 25(1-3):173–191, 2009.

[31] Pavel A Cherenkov. Visible emission of clean liquids by action of γ radiation. *Doklady Akademii Nauk SSSR*, 2:451, 1934.

[32] Malcolm S Longair. *High energy astrophysics*. Cambridge university press, 2011.

[33] CW Akerlof, MF Cawley, M Chantell, DJ Fegan, K Harris, AM Hillas, DG Jennings, RC Lamb, MA Lawrence, and MJ Lang. Locating very high energy gamma ray sources with arc minute accuracy. In *NASA Conference Publication*, volume 3137, 1992.

[34] VP Fomin, AA Stepanian, RC Lamb, c DA Lewis, M Punch, and TC Weekes. New methods of atmospheric Cherenkov imaging for gamma-ray astronomy. I. The false source method. *Astroparticle Physics*, 2(2):137–150, 1994.

[35] Werner Hofmann, I Jung, A Konopelko, H Krawczynski, H Lampeitl, and G Pühlhofer. Comparison of techniques to reconstruct VHE gamma-ray showers from multiple stereoscopic Cherenkov images. *Astroparticle Physics*, 12(3):135–143, 1999.

[36] Walter F Wargau. Comparing seeing measurements at SAAO/Sutherland, Gamsberg/Namibia and ESO/La Silla. *Monthly Notes of the Astronomical Society of South Africa*, 53:88, 1994.

[37] John M Davies and Eugene S Cotton. Design of the quartermaster solar furnace. *Solar Energy*, 1(2-3):16–22, 1957.

[38] Stefan Gillessen. *Sub-Bogenminuten-genaue Positionen von TeV-Quellen mit HESS*. PhD thesis, 2004.

[39] P Hofverberg, R Kankanyan, M Panter, G Hermann, W Hofmann, C Deil, F Ait Benkhali, et al. Commissioning and initial performance of the HESS II drive system. *arXiv preprint arXiv:1307.4550*, 2013.

[40] A Balzer, M Füßling, P Hofverberg, and RD Parsons. The Performance of the HESS Target of Opportunity Alert System. In *Journal of Physics: Conference Series*, volume 664, page 082002. IOP Publishing, 2015.

[41] Arnim Balzer, M Füßling, M Gajdus, D Göring, A Lopatin, M de Naurois, S Schlenker, U Schwanke, and Christian Stegmann. The hess central data acquisition system. *Astroparticle Physics*, 54:67–80, 2014.

[42] Arnim Balzer. Systematic studies of the HESS camera calibration. Technical report, 2010.

[43] Mathieu de Naurois and Loïc Rolland. A high performance likelihood reconstruction of γ-rays for imaging atmospheric Cherenkov telescopes. *Astroparticle Physics*, 32(5): 231–252, 2009.

[44] Ronald A Fisher. On an absolute criterion for fitting frequency curves. *Messenger of Mathematics*, 1912.

[45] MA RA Fisher. On the mathematical foundations of theoretical statistics. *Phil. Trans. R. Soc. Lond. A*, 222(594-604):309–368, 1922.

[46] D. Berge, S. Funk, and J. Hinton. Background modelling in very-high-energy γ-ray astronomy. *Astronomy and Astrophysics*, 466:1219–1229, May 2007. doi: 10.1051/0004-6361:20066674.

[47] F Aharonian, A Akhperjanian, J Barrio, K Bernlöhr, H Börst, H Bojahr, O Bolz, J Contreras, J Cortina, S Denninghoff, et al. Evidence for TeV gamma ray emission from Cassiopeia A. *Astronomy & Astrophysics*, 370(1):112–120, 2001.

[48] F Aharonian, AG Akhperjanian, K-M Aye, AR Bazer-Bachi, M Beilicke, W Benbow, D Berge, P Berghaus, K Bernlöhr, O Bolz, et al. HESS observations of PKS 2155-304. *Astronomy & astrophysics*, 430(3):865–875, 2005.

[49] Markus Holler. Photon reconstruction for the HESS 28 m telescope and analysis of Crab Nebula and galactic centre observations. 2014.

[50] H Abdalla, A Abramowski, F Aharonian, F Ait Benkhali, AG Akhperjanian, T Andersson, EO Angüner, M Arrieta, P Aubert, M Backes, et al. Gamma-ray blazar spectra with HESS II mono analysis: The case of PKS 2155- 304 and PG 1553+ 113. *Astronomy & Astrophysics*, 600:A89, 2017.

[51] H.E.S.S. Collaboration. Observations of the Crab nebula with HESS. *Astronomy and Astrophysics*, 457:899–915, October 2006. doi: 10.1051/0004-6361:20065351.

[52] BP Abbott, Richard Abbott, TD Abbott, MR Abernathy, Fausto Acernese, Kendall Ackley, Carl Adams, Thomas Adams, Paolo Addesso, RX Adhikari, et al. Observation of gravitational waves from a binary black hole merger. *Physical review letters*, 116(6): 061102, 2016.

[53] Benjamin P Abbott, Rich Abbott, TD Abbott, Fausto Acernese, Kendall Ackley, Carl Adams, Thomas Adams, Paolo Addesso, RX Adhikari, VB Adya, et al. GW170817: observation of gravitational waves from a binary neutron star inspiral. *Physical Review Letters*, 119(16):161101, 2017.

[54] Christopher J Moore, Robert H Cole, and Christopher PL Berry. Gravitational-wave sensitivity curves. *Classical and Quantum Gravity*, 32(1):015014, 2014.

[55] MG Aartsen, M Ackermann, J Adams, JA Aguilar, M Ahlers, M Ahrens, D Altmann, T Anderson, C Arguelles, TC Arlen, et al. Observation of high-energy astrophysical neutrinos in three years of IceCube data. *Physical review letters*, 113(10):101101, 2014.

[56] F Acero, F Aharonian, AG Akhperjanian, G Anton, U Barres De Almeida, AR Bazer-Bachi, Y Becherini, B Behera, K Bernlöhr, A Bochow, et al. Detection of gamma rays from a starburst galaxy. *Science*, 326(5956):1080–1082, 2009.

[57] A Abramowski, Fabio Acero, F Aharonian, AG Akhperjanian, G Anton, A Balzer, A Barnacka, Yvonne Becherini, J Becker, K Bernlöhr, et al. Spectral analysis and interpretation of the γ-ray emission from the starburst galaxy NGC 253. *The Astrophysical Journal*, 757(2):158, 2012.

[58] H.E.S.S. Collaboration. The starburst galaxy NGC 253 revisited by H.E.S.S. and Fermi-LAT: The starburst galaxy NGC 253 revisited by H.E.S.S. and Fermi-LAT, year = 2018. *Accepted in Astronomy and Astrophysics*.

[59] R. C. Kennicutt and N. J. Evans. Star Formation in the Milky Way and Nearby Galaxies. *Annual Review of Astronomy and Astrophysics*, 50:531–608, September 2012. doi: 10.1146/annurev-astro-081811-125610.

[60] Ruben J Diaz, Horacio Dottori, Maria P Aguero, Evencio Mediavilla, Irapuan Rodrigues, and Damian Mast. Hidden trigger for the giant starburst arc in M83? *The Astrophysical Journal*, 652(2):1122, 2006.

[61] RP Norris. The double radio nucleus of Arp 220. *Monthly Notices of the Royal Astronomical Society*, 230(2):345–351, 1988.

[62] Markus Ackermann, Marco Ajello, A Allafort, Luca Baldini, J Ballet, Guido Barbiellini, MG Baring, D Bastieri, K Bechtol, R Bellazzini, et al. Detection of the characteristic pion-decay signature in supernova remnants. *Science*, 339(6121):807–811, 2013.

[63] Stefan Ohm and JA Hinton. Non-thermal emission from pulsar-wind nebulae in starburst galaxies. *Monthly Notices of the Royal Astronomical Society: Letters*, 429(1): L70–L74, 2013.

[64] Nick Indriolo and Benjamin J. McCall. Cosmic-ray astrochemistry. *Chem. Soc. Rev.*, 42:7763–7773, 2013. doi: 10.1039/C3CS60087D. URL `http://dx.doi.org/10.1039/C3CS60087D`.

[65] P. P. Papadopoulos and W.-F. Thi. The Initial Conditions of Star Formation: Cosmic Rays as the Fundamental Regulators. In D. F. Torres and O. Reimer, editors, *Cosmic Rays in Star-Forming Environments*, volume 34 of *Advances in Solid State Physics*, page 41, 2013. doi: 10.1007/978-3-642-35410-6_5.

[66] RA Chevalier and Andrew W Clegg. Wind from a starburst galaxy nucleus. *Nature*, 317(6032):44, 1985.

[67] Vladimir N Zirakashvili and HJ Völk. Simple model of the outflow from starburst galaxies: Application to radio observations. *The Astrophysical Journal*, 636(1):140, 2006.

[68] Felix A Aharonian.

[69] Ervin Kafexhiu, Felix Aharonian, Andrew M. Taylor, and Gabriela S. Vila. Parametrization of gamma-ray production cross-sections for pp interactions in a broad proton energy range from the kinematic threshold to PeV energies. *Phys. Rev.*, D90 (12):123014, 2014. doi: 10.1103/PhysRevD.90.123014.

[70] Particle Data Group. Review of Particle Physics. *Chin. Phys. C*, 40:100001, 2016.

[71] Morad Aaboud, G Aad, B Abbott, J Abdallah, O Abdinov, B Abeloos, R Aben, OS AbouZeid, NL Abraham, H Abramowicz, et al. Measurement of the Inelastic Proton-Proton Cross Section at s= 13 TeV with the ATLAS Detector at the LHC. *Physical review letters*, 117(18):182002, 2016.

[72] Pedro Abreu, M Aglietta, EJ Ahn, Ivone Freire da Mota Albuquerque, D Allard, I Allekotte, J Allen, P Allison, A Almeda, J Alvarez Castillo, et al. Measurement of the proton-air cross section at s= 57 tev with the pierre auger observatory. *Physical Review Letters*, 109(6):062002, 2012.

[73] R Cowsik, Yash Pal, SN Tandon, and RP Verma. Steady state of cosmic-ray nuclei—Their spectral shape and path length at low energies. *Physical Review*, 158(5):1238, 1967.

[74] M Aguilar, L Ali Cavasonza, G Ambrosi, L Arruda, N Attig, S Aupetit, P Azzarello, A Bachlechner, F Barao, A Barrau, et al. Precision measurement of the boron to carbon flux ratio in cosmic rays from 1.9 GV to 2.6 TV with the alpha magnetic spectrometer on the international space station. *Physical review letters*, 117(23):231102, 2016.

[75] Roger Blandford and David Eichler. Particle acceleration at astrophysical shocks: A theory of cosmic ray origin. *Physics Reports*, 154(1):1–75, 1987.

[76] Alberto D Bolatto, Steven R Warren, Adam K Leroy, Fabian Walter, Sylvain Veilleux, Eve C Ostriker, Jürgen Ott, Martin Zwaan, David B Fisher, Axel Weiss, et al. Suppression of star formation in the galaxy NGC 253 by a starburst-driven molecular wind. *Nature*, 499(7459):450, 2013.

[77] Mousumi Das, KR Anantharamaiah, and MS Yun. The central velocity field in NGC 253: possible indication of a bar. *The Astrophysical Journal*, 549(2):896, 2001.

[78] DM Lucero, C Carignan, EC Elson, TH Randriamampandry, TH Jarrett, TA Oosterloo, and GH Heald. H i observations of the nearest starburst galaxy NGC 253 with the SKA precursor KAT-7. *Monthly Notices of the Royal Astronomical Society*, 450 (4):3935–3951, 2015.

[79] Daniel R Wik, Bret D Lehmer, Ann E Hornschemeier, Mihoko Yukita, Andrew Ptak, Andreas Zezas, Vallia Antoniou, Megan K Argo, Keith Bechtol, Steven Boggs, et al. Spatially resolving a starburst galaxy at hard X-ray energies: NuSTAR, CHANDRA, AND VLBA observations of NGC 253. *The Astrophysical Journal*, 797(2):79, 2014.

[80] James S Ulvestad and Robert RJ Antonucci. VLA observations of NGC 253: supernova remnants and H II regions at 1 parsec resolution. *The Astrophysical Journal*, 488(2): 621, 1997.

[81] Kimberly A Weaver, Timothy M Heckman, David K Strickland, and Michael Dahlem. Chandra observations of the evolving core of the starburst galaxy NGC 253. *The Astrophysical Journal Letters*, 576(1):L19, 2002.

[82] A Brunthaler, P Castangia, A Tarchi, C Henkel, MJ Reid, H Falcke, and KM Menten. Evidence of a pure starburst nature of the nuclear region of NGC 253. *Astronomy & Astrophysics*, 497(1):103–108, 2009.

[83] Emil Lenc and Steven J Tingay. The subparsec-scale radio properties of southern starburst galaxies. I. Supernova remnants, the supernova rate, and the ionized medium in the NGC 253 starburst. *The Astronomical Journal*, 132(3):1333, 2006.

[84] Dave Van Buren and Matthew A Greenhouse. A more direct measure of supernova rates in starburst galaxies. *The Astrophysical Journal*, 431:640–644, 1994.

[85] CW Engelbracht, Marcia J Rieke, George H Rieke, DM Kelly, and JM Achtermann. The Nuclear starburst in NGC 253. *The Astrophysical Journal*, 505(2):639, 1998.

[86] VP Melo, AM Pérez García, JA Acosta-Pulido, C Muñoz-Tuñón, and JM Rodríguez Espinosa. The spatial distribution of the far-infrared emission in NGC 253. *The Astrophysical Journal*, 574(2):709, 2002.

[87] Julianne J Dalcanton, Benjamin F Williams, Seth, et al. The ACS nearby galaxy survey treasury. *ApJS*, 183(1):67, 2009.

[88] F Aharonian, AG Akhperjanian, AR Bazer-Bachi, M Beilicke, W Benbow, D Berge, K Bernlöhr, C Boisson, O Bolz, V Borrel, and otherse. A search for very high energy γ-ray emission from the starburst galaxy NGC 253 with HESS. *Astronomy & Astrophysics*, 442(1):177–183, 2005.

[89] AA Abdo, Markus Ackermann, Marco Ajello, WB Atwood, Magnus Axelsson, Luca Baldini, J Ballet, Guido Barbiellini, D Bastieri, K Bechtol, et al. Detection of gamma-ray emission from the starburst galaxies M82 and NGC 253 with the large area telescope on Fermi. *The Astrophysical Journal Letters*, 709(2):L152, 2010.

[90] M Ackermann, M Ajello, A Allafort, L Baldini, J Ballet, D Bastieri, K Bechtol, R Bellazzini, B Berenji, ED Bloom, et al. GeV observations of star-forming galaxies with the Fermi large area telescope. *The Astrophysical Journal*, 755(2):164, 2012.

[91] The Fermi-LAT Collaboration. Fermi large area telescope third source catalog. *The Astrophysical Journal Supplement Series*, 218(2):23, 2015.

[92] The Fermi-LAT Collaboration. Pass 8: Toward the Full Realization of the Fermi-LAT Scientific Potential. 03 2013. URL `https://arxiv.org/abs/1303.3514`.

[93] H.E.S.S. Collaboration. The exceptionally powerful TeV γ-ray emitters in the Large Magellanic Cloud. *Science*, 347(6220):406–412, January 2015.

[94] TH Jarrett, T Chester, R Cutri, SE Schneider, and JP Huchra. The 2MASS large galaxy atlas. *The Astronomical Journal*, 125(2):525, 2003.

[95] Víctor Zabalza. naima: a Python package for inference of relativistic particle energy distributions from observed nonthermal spectra. *arXiv preprint arXiv:1509.03319*, 2015.

[96] Jonathan Goodman and Jonathan Weare. Ensemble samplers with affine invariance. *Communications in applied mathematics and computational science*, 5(1):65–80, 2010.

[97] Daniel Foreman-Mackey, David W Hogg, Dustin Lang, and Jonathan Goodman. emcee: the MCMC hammer. *Publications of the Astronomical Society of the Pacific*, 125 (925):306, 2013.

[98] Torbjörn Sjöstrand, Stephen Mrenna, and Peter Skands. A brief introduction to PYTHIA 8.1. *Computer Physics Communications*, 178(11):852–867, 2008.

[99] G Terreran, ML Pumo, T-W Chen, TJ Moriya, Fransesco Taddia, L Dessart, L Zampieri, SJ Smartt, S Benetti, C Inserra, et al. Hydrogen-rich supernovae beyond the neutrino-driven core-collapse paradigm. *Nature astronomy*, 1(10):713, 2017.

[100] V. L. Ginzburg and S. I. Syrovatskii. *The origin of cosmic rays*. 1969.

[101] Luke O'C Drury. Origin of cosmic rays. *Astroparticle Physics*, 39:52–60, 2012.

[102] C. Carilli and S. Rawlings. Science with the Square Kilometer Array: Motivation, Key Science Projects, Standards and Assumptions. URL `https://arxiv.org/abs/astro-ph/0409274`.

[103] Alessandro De Angelis, Vincent Tatischeff, Marco Tavani, Uwe Oberlack, Isabelle Grenier, Lorraine Hanlon, Roland Walter, Andrea Argan, Peter von Ballmoos, Andrea Bulgarelli, et al. The e-ASTROGAM mission. *Experimental Astronomy*, 44(1):25–82, 2017.

[104] The Cherenkov Telescope Array Consortium. Science with the Cherenkov Telescope Array. 09 2017. URL `https://arxiv.org/abs/1709.07997`.

[105] Ugo Giaccari et al. Arrival directions of the highest-energy cosmic rays detected by the Pierre Auger Observatory. 2017.

[106] Abraham Loeb and Eli Waxman. The cumulative background of high energy neutrinos from starburst galaxies. *Journal of Cosmology and Astroparticle Physics*, 2006(05):003, 2006.

[107] MG Aartsen, M Ackermann, J Adams, JA Aguilar, M Ahlers, M Ahrens, D Altmann, T Anderson, C Arguelles, TC Arlen, et al. Search for prompt neutrino emission from gamma-ray bursts with IceCube. *The Astrophysical Journal Letters*, 805(1):L5, 2015.

[108] Irene Tamborra, Shin'ichiro Ando, and Kohta Murase. Star-forming galaxies as the origin of diffuse high-energy backgrounds: Gamma-ray and neutrino connections, and implications for starburst history. *Journal of Cosmology and Astroparticle Physics*, 2014(09):043, 2014.

[109] F Aharonian, AG Akhperjanian, AR Bazer-Bachi, B Behera, M Beilicke, W Benbow, D Berge, K Bernlöhr, C Boisson, O Bolz, et al. An exceptional very high energy Gamma-Ray flare of PKS 2155–304. *The Astrophysical Journal Letters*, 664(2):L71, 2007.

[110] CA Meegan, GJ Fishman, RB Wilson, WS Paciesas, GN Pendleton, JM Horack, MN Brock, and C Kouveliotou. Spatial distribution of γ-ray bursts observed by BATSE. *Nature*, 355(6356):143, 1992.

[111] Chryssa Kouveliotou, Charles A Meegan, Gerald J Fishman, Narayana P Bhat, Michael S Briggs, Thomas M Koshut, William S Paciesas, and Geoffrey N Pendleton. Identification of two classes of gamma-ray bursts. *The Astrophysical Journal*, 413:L101–L104, 1993.

[112] D Band, J Matteson, L Ford, B Schaefer, D Palmer, B Teegarden, T Cline, M Briggs, W Paciesas, G Pendleton, et al. BATSE observations of gamma-ray burst spectra. I-Spectral diversity. *The Astrophysical Journal*, 413:281–292, 1993.

[113] C Akerlof, R Balsano, S Barthelmy, J Bloch, P Butterworth, D Casperson, T Cline, S Fletcher, F Frontera, G Gisler, et al. Observation of contemporaneous optical radiation from a γ-ray burst. *nature*, 398(6726):400, 1999.

[114] DM Coward, EJ Howell, Marica Branchesi, G Stratta, Dafne Guetta, Bruce Gendre, and Damien Macpherson. The Swift gamma-ray burst redshift distribution: selection biases and optical brightness evolution at high z? *Monthly Notices of the Royal Astronomical Society*, 432(3):2141–2149, 2013.

[115] Neil Gehrels, Guido Chincarini, P Giommi, KO Mason, JA Nousek, AA Wells, NE White, SD Barthelmy, DN Burrows, LR Cominsky, et al. The Swift gamma-ray burst mission. *The Astrophysical Journal*, 611(2):1005, 2004.

[116] R Salvaterra, M Della Valle, S Campana, G Chincarini, S Covino, P D'Avanzo, A Fernández-Soto, C Guidorzi, F Mannucci, R Margutti, et al. GRB 090423 at a redshift of $z \approx 8.1$. *Nature*, 461(7268):1258, 2009.

[117] Charles A Meegan, Geoffrey N Pendleton, Michael S Briggs, Chryssa Kouveliotou, Thomas M Koshut, John Patrick Lestrade, William S Paciesas, Michael L McCollough, Jerome J Brainerd, John M Horack, et al. The third BATSE gamma-ray burst catalog. *The Astrophysical Journal Supplement Series*, 106:65, 1996.

[118] William S Paciesas, Charles A Meegan, Geoffrey N Pendleton, Michael S Briggs, Chryssa Kouveliotou, Thomas M Koshut, John Patrick Lestrade, Michael L McCollough, Jerome J Brainerd, Jon Hakkila, et al. The fourth BATSE gamma-ray burst catalog (revised). *The Astrophysical Journal Supplement Series*, 122(2):465, 1999.

[119] P Narayana Bhat, Charles A Meegan, Andreas von Kienlin, William S Paciesas, Michael S Briggs, J Michael Burgess, Eric Burns, Vandiver Chaplin, William H Cleveland, Andrew C Collazzi, et al. The Third Fermi GBM Gamma-Ray Burst Catalog: The First Six Years. *The Astrophysical Journal Supplement Series*, 223(2):28, 2016.

[120] M Ruderman. Theories of γ-ray bursts. *Annals of the New York Academy of Sciences*, 262(1):164–180, 1975.

[121] Tsvi Piran. Gamma-ray bursts and the fireball model. *Physics Reports*, 314(6):575–667, 1999.

[122] Andreas Von Kienlin, Charles A Meegan, William S Paciesas, PN Bhat, Elisabetta Bissaldi, Michael S Briggs, J Michael Burgess, David Byrne, Vandiver Chaplin, William Cleveland, et al. The second Fermi GBM gamma-ray burst catalog: the first four years. *The Astrophysical Journal Supplement Series*, 211(1):13, 2014.

[123] David Gruber, Adam Goldstein, Victoria Weller von Ahlefeld, P Narayana Bhat, Elisabetta Bissaldi, Michael S Briggs, Dave Byrne, William H Cleveland, Valerie Connaughton, Roland Diehl, et al. The Fermi GBM gamma-ray burst spectral catalog: four years of data. *The Astrophysical Journal Supplement Series*, 211(1):12, 2014.

[124] Markus Ackermann, Marco Ajello, K Asano, Magnus Axelsson, Luca Baldini, J Ballet, Guido Barbiellini, D Bastieri, K Bechtol, R Bellazzini, et al. The first Fermi-LAT gamma-ray burst catalog. *The Astrophysical Journal Supplement Series*, 209(1):11, 2013.

[125] K Hurley, BL Dingus, R Mukherjee, P Sreekumar, C Kouveliotou, C Meegan, GJ Fishman, D Band, L Ford, D Bertsch, et al. Detection of a γ-ray burst of very long duration and very high energy. *Nature*, 372(6507):652–654, 1994.

[126] M Sommer, DL Bertsch, BL Dingus, CE Fichtel, GJ Fishman, AK Harding, RC Hartman, SD Hunter, K Hurley, G Kanbach, et al. High-energy gamma rays from the intense 1993 January 31 gamma-ray burst. *The Astrophysical Journal*, 422:L63–L66, 1994.

[127] MM González, BL Dingus, Y Kaneko, RD Preece, et al. A gamma-ray burst with a high-energy spectral component inconsistent with the synchrotron shock model. *Nature*, 424(6950):749, 2003.

[128] M Ackermann, M Ajello, L Baldini, G Barbiellini, MG Baring, K Bechtol, R Bellazzini, RD Blandford, ED Bloom, Eea Bonamente, et al. Constraining the high-energy emission from gamma-ray bursts with Fermi. *The Astrophysical Journal*, 754(2):121, 2012.

[129] Giacomo Vianello, Nicola Omodei, et al. The First 100 LAT Gamma-Ray Bursts: A New Detection Algorithm and Pass 8. *arXiv preprint arXiv:1502.03122*, 2015.

[130] M Ackermann, M Ajello, K Asano, WB Atwood, Magnus Axelsson, L Baldini, J Ballet, G Barbiellini, MG Baring, Dea Bastieri, et al. Fermi-LAT observations of the gamma-ray burst GRB 130427A. *Science*, page 1242353, 2013.

[131] Asaf Pe'er. Physics of gamma-ray bursts prompt emission. *Advances in Astronomy*, 2015, 2015.

[132] JA Nousek, C Kouveliotou, D Grupe, KL Page, J Granot, E Ramirez-Ruiz, SK Patel, DN Burrows, V Mangano, S Barthelmy, et al. Evidence for a canonical gamma-ray burst afterglow light curve in the Swift XRT data. *The Astrophysical Journal*, 642(1): 389, 2006.

[133] George B Rybicki and Alan P Lightman. *Radiative processes in astrophysics*. John Wiley & Sons, 2008.

[134] E Cohen, JI Katz, T Piran, R Sari, RD Preece, and DL Band. Possible evidence for relativistic shocks in gamma-ray bursts. *The Astrophysical Journal*, 488(1):330, 1997.

[135] Re'em Sari, Tsvi Piran, and Ramesh Narayan. Spectra and light curves of gamma-ray burst afterglows. *The Astrophysical Journal Letters*, 497(1):L17, 1998. URL `http://stacks.iop.org/1538-4357/497/i=1/a=L17`.

[136] Boris E Stern and Juri Poutanen. Gamma-ray bursts from synchrotron self-Compton emission. *Monthly Notices of the Royal Astronomical Society*, 352(3):L35–L39, 2004.

[137] Nicole M Lloyd-Ronning and Vahé Petrosian. Interpreting the behavior of time-resolved gamma-ray burst spectra. *The Astrophysical Journal*, 565(1):182, 2002.

[138] Mikhail V Medvedev. Theory of "jitter" radiation from small-scale random magnetic fields and prompt emission from gamma-ray burst shocks. *The Astrophysical Journal*, 540(2):704, 2000.

[139] Asaf Pe'er and Bing Zhang. Synchrotron emission in small-scale magnetic fields as a possible explanation for prompt emission spectra of gamma-ray bursts. *The Astrophysical Journal*, 653(1):454, 2006.

[140] Peter Meszaros and Martin J Rees. Steep slopes and preferred breaks in gamma-ray burst spectra: The role of photospheres and comptonization. *The Astrophysical Journal*, 530(1):292, 2000.

[141] Željka Bošnjak and Frédéric Daigne. Spectral evolution in gamma-ray bursts: Predictions of the internal shock model and comparison to observations. *Astronomy & Astrophysics*, 568:A45, 2014.

[142] Ariadna Murguia-Berthier, Enrico Ramirez-Ruiz, Charles D Kilpatrick, Ryan J Foley, Daniel Kasen, William H Lee, Anthony L Piro, David A Coulter, Maria R Drout, Barry F Madore, et al. A Neutron Star Binary Merger Model for GW170817/GRB 170817A/SSS17a. *The Astrophysical Journal Letters*, 848(2):L34, 2017.

[143] SE Woosley and JS Bloom. The supernova–gamma-ray burst connection. *Annu. Rev. Astron. Astrophys.*, 44:507–556, 2006.

[144] Tomer Shenar, W-R Hamann, and Helge Todt. The impact of rotation on the line profiles of Wolf-Rayet stars. *Astronomy & Astrophysics*, 562:A118, 2014.

[145] AJ Levan, Nial R Tanvir, RLC Starling, K Wiersema, KL Page, DA Perley, Steve Schulze, Graham A Wynn, R Chornock, Jens Hjorth, et al. A new population of ultra-long duration gamma-ray bursts. *The Astrophysical Journal*, 781(1):13, 2013.

[146] Bin-Bin Zhang, Bing Zhang, Kohta Murase, Valerie Connaughton, and Michael S Briggs. How long does a burst burst? *The Astrophysical Journal*, 787(1):66, 2014.

[147] Omer Bromberg, Ehud Nakar, and Tsvi Piran. Are low-luminosity gamma-ray bursts generated by relativistic jets? *The Astrophysical Journal Letters*, 739(2):L55, 2011.

[148] Rasha Abbasi, Yasser Abdou, T Abu-Zayyad, M Ackermann, J Adams, JA Aguilar, M Ahlers, D Altmann, K Andeen, J Auffenberg, et al. An absence of neutrinos associated with cosmic ray acceleration in gamma-ray bursts. *arXiv preprint arXiv:1204.4219*, 2012.

[149] MG Aartsen et al. Search for time-independent neutrino emission from astrophysical sources with 3 yr of IceCube data. *The Astrophysical Journal*, 779(2):132, 2013.

[150] MG Aartsen, K Abraham, M Ackermann, J Adams, Juan A Aguilar, M Ahlers, M Ahrens, D Altmann, T Anderson, M Archinger, et al. A combined maximum-likelihood analysis of the high-energy astrophysical neutrino flux measured with IceCube. *The Astrophysical Journal*, 809(1):98, 2015.

[151] Nicholas Senno, Kohta Murase, and Peter Mészáros. Choked jets and low-luminosity gamma-ray bursts as hidden neutrino sources. *Physical Review D*, 93(8):083003, 2016.

[152] Eli Waxman, P Mészáros, and S Campana. GRB 060218: a relativistic supernova shock breakout. *The Astrophysical Journal*, 667(1):351, 2007.

[153] Xiang-Yu Wang, Zhuo Li, Eli Waxman, and Peter Mészáros. Nonthermal gamma-ray/X-ray flashes from shock breakout in gamma-ray burst-associated supernovae. *The Astrophysical Journal*, 664(2):1026, 2007.

[154] Li-Xin Li and Bohdan Paczyński. Transient events from neutron star mergers. *The Astrophysical Journal Letters*, 507(1):L59, 1998.

[155] Brian D Metzger. The kilonova handbook. *arXiv preprint arXiv:1610.09381*, 2016.

[156] A Goldstein, P Veres, E Burns, MS Briggs, R Hamburg, D Kocevski, CA Wilson-Hodge, RD Preece, S Poolakkil, OJ Roberts, et al. An ordinary short gamma-ray burst with extraordinary implications: Fermi-GBM detection of GRB 170817A. *The Astrophysical Journal Letters*, 848(2):L14, 2017.

[157] BP Abbott et al. Multi-messenger observations of a binary neutron star merger. *Astrophysical Journal Letters*, 848(2):L12, 2017.

[158] M Nicholl, E Berger, D Kasen, BD Metzger, J Elias, C Briceño, KD Alexander, PK Blanchard, R Chornock, PS Cowperthwaite, et al. The electromagnetic counterpart of the binary neutron star merger LIGO/Virgo GW170817. III. Optical and UV spectra of a blue kilonova from fast polar ejecta. *The Astrophysical Journal Letters*, 848(2):L18, 2017.

[159] Rudy C Gilmore, Rachel S Somerville, Joel R Primack, and Alberto Domínguez. Semi-analytic modelling of the extragalactic background light and consequences for extragalactic gamma-ray spectra. *Monthly Notices of the Royal Astronomical Society*, 422 (4):3189–3207, 2012.

[160] Tomonori Totani. Cosmological gamma-ray bursts and evolution of galaxies. *The Astrophysical Journal Letters*, 486(2):L71, 1997.

[161] GCN and NASA. The Gamma-Ray Bursts Coordinates Network. *http://gcn.gsfc.nasa.gov*, 2009. URL `http://gcn.gsfc.nasa.gov`.

[162] J. S. Bloom, S. G. Djorgovski, S. R. Kulkarni, and D. A. Frail. The Host Galaxy of GRB 970508. *Astrophys.J.*, 507:L25–L28, 1998. URL `https://arxiv.org/abs/astro-ph/9807315`.

[163] Tim D. Staley and Rob Fender. The 4 Pi Sky Transient Alerts Hub. *arXiv*, 06 2016. URL `https://arxiv.org/abs/1606.03735`.

[164] Lukasz Wyrzykowski, Simon Hodgkin, Nadejda Blogorodnova, Sergey Koposov, and Ross Burgon. Photometric Science Alerts from Gaia. 10 2012. URL `https://arxiv.org/abs/1210.5007`.

[165] Rob Fender, Robert Braun, Ben Stappers, Ralph Wijers, Michael Wise, Thijs Coenen, Heino Falcke, Jean-Mathias Griessmeier, Michiel van Haarlem, Peter Jonker, et al. The lofar transients key project. *arXiv preprint astro-ph/0611298*, 2006.

[166] John D Swinbank et al. The LOFAR Transients Pipeline. *Astronomy and Computing*, 11:25–48, 2015.

[167] Benjamin Shappee, J Prieto, KZ Stanek, CS Kochanek, T Holoien, J Jencson, U Basu, JF Beacom, D Szczygiel, G Pojmanski, et al. All sky automated survey for supernovae (asas-sn or. In *American Astronomical Society Meeting Abstracts# 223*, volume 223, 2014.

[168] Robert E Rutledge. The astronomer's telegram: A web-based short-notice publication system for the professional astronomical community. *Publications of the Astronomical Society of the Pacific*, 110(748):754, 1998.

[169] RL Aptekar, DD Frederiks, SV Golenetskii, VN Ilynskii, EP Mazets, VN Panov, ZJ Sokolova, MM Terekhov, LO Sheshin, TL Cline, et al. Konus-w gamma-ray burst experiment for the ggs wind spacecraft. *Space Science Reviews*, 71(1-4):265–272, 1995.

[170] Swift bat intrument description, . URL `https://swift.gsfc.nasa.gov/about_swift/bat_desc.html`.

[171] Swift xrt instrument description, . URL `https://swift.gsfc.nasa.gov/about_swift/xrt_desc.html`.

[172] Swift uvot instrument description, . URL `https://swift.gsfc.nasa.gov/about_swift/uvot_desc.html`.

[173] MG Aartsen, M Ackermann, Joe Adams, JA Aguilar, M Ahlers, M Ahrens, D Altmann, K Andeen, T Anderson, I Ansseau, et al. The icecube realtime alert system. *Astroparticle Physics*, 92:30–41, 2017.

[174] M Ageron, JA Aguilar, I Al Samarai, A Albert, M André, M Anghinolfi, G Anton, S Anvar, M Ardid, AC Assis Jesus, et al. The antares telescope neutrino alert system. *Astroparticle Physics*, 35(8):530–536, 2012.

[175] Leo P Singer and Larry R Price. Rapid bayesian position reconstruction for gravitational-wave transients. *Physical Review D*, 93(2):024013, 2016.

[176] LSST Science Collaborations, Phil Marshall, Timo Anguita, Federica B. Bianco, Eric C. Bellm, Niel Brandt, Will Clarkson, Andy Connolly, Eric Gawiser, Zeljko Ivezic, Lynne Jones, Michelle Lochner, Michael B. Lund, Ashish Mahabal, David Nidever, Knut Olsen, Stephen Ridgway, Jason Rhodes, Ohad Shemmer, David Trilling, Kathy

Vivas, Lucianne Walkowicz, Beth Willman, Peter Yoachim, Scott Anderson, Pierre Antilogus, Ruth Angus, Iair Arcavi, Humna Awan, Rahul Biswas, Keaton J. Bell, David Bennett, Chris Britt, Derek Buzasi, Dana I. Casetti-Dinescu, Laura Chomiuk, Chuck Claver, Kem Cook, James Davenport, Victor Debattista, Seth Digel, Zoheyr Doctor, R. E. Firth, Ryan Foley, Wen fai Fong, Lluis Galbany, Mark Giampapa, John E. Gizis, Melissa L. Graham, Carl Grillmair, Phillipe Gris, Zoltan Haiman, and Patrick Hartigan. Science-driven optimization of the lsst observing strategy. 08 2017. URL `https://arxiv.org/abs/1708.04058`.

[177] J. Wei, B. Cordier, S. Antier, P. Antilogus, J.-L. Atteia, A. Bajat, S. Basa, V. Beckmann, M.G. Bernardini, S. Boissier, L. Bouchet, V. Burwitz, A. Claret, Z.-G. Dai, F. Daigne, J. Deng, D. Dornic, H. Feng, T. Foglizzo, H. Gao, N. Gehrels, O. Godet, A. Goldwurm, F. Gonzalez, L. Gosset, D. Götz, C. Gouiffes, F. Grise, A. Gros, J. Guilet, X. Han, M. Huang, Y.-F. Huang, M. Jouret, A. Klotz, O. La Marle, C. Lachaud, E. Le Floch, W. Lee, N. Leroy, L.-X. Li, S. C. Li, Z. Li, E.-W. Liang, H. Lyu, K. Mercier, G. Migliori, R. Mochkovitch, P. O'Brien, J. Osborne, J. Paul, E. Perinati, P. Petitjean, F. Piron, Y. Qiu, A. Rau, J. Rodriguez, S. Schanne, N. Tanvir, E. Vangioni, S. Vergani, F.-Y. Wang, J. Wang, X.-G. Wang, X.-Y. Wang, A. Watson, N. Webb, J. J. Wei, R. Willingale, C. Wu, and X.-F. Wu. The deep and transient universe in the svom era: New challenges and opportunities - scientific prospects of the svom mission. 10 2016. URL `https://arxiv.org/abs/1610.06892`.

[178] Simon Johnston. Science with the australian square kilometre array pathfinder. *PoSMRU:006,2007*, 11 2007. URL `https://arxiv.org/abs/0711.2103`.

[179] D. R. Lorimer, M. Bailes, M. A. McLaughlin, D. J. Narkevic, and F. Crawford. A bright millisecond radio burst of extragalactic origin. 09 2007. URL `https://arxiv.org/abs/0709.4301`.

[180] F Aharonian, AG Akhperjanian, U Barres De Almeida, AR Bazer-Bachi, B Behera, W Benbow, K Bernlöhr, C Boisson, A Bochow, V Borrel, et al. Hess observations of gamma-ray bursts in 2003–2007. *Astronomy and Astrophysics*, 495(2):505–512, 2009.

[181] MG Aartsen, K Abraham, M Ackermann, Joe Adams, JA Aguilar, M Ahlers, M Ahrens, D Altmann, K Andeen, T Anderson, et al. Very high-energy gamma-ray follow-up program using neutrino triggers from icecube. *arXiv preprint arXiv:1610.01814*, 2016.

[182] S Adrián-Martínez, M Ageron, A Albert, I Al Samarai, M André, G Anton, M Ardid, J-J Aubert, B Baret, J Barrios-Marti, et al. Optical and x-ray early follow-up of antares neutrino alerts. *Journal of Cosmology and Astroparticle Physics*, 2016(02):062, 2016.

[183] Albert Einstein. Über gravitationswellen. *Sitzungsberichte der Königlich Preußischen Akademie der Wissenschaften (Berlin), Seite 154-167.*, 1918.

[184] Albert Einstein. Die grundlage der allgemeinen relativitätstheorie. *Annalen der Physik*, 354(7):769–822, 1916.

[185] Russell A Hulse and Joseph H Taylor. Discovery of a pulsar in a binary system. *The Astrophysical Journal*, 195:L51–L53, 1975.

[186] Joseph H Taylor and Joel M Weisberg. A new test of general relativity-gravitational radiation and the binary pulsar psr 1913+ 16. *The Astrophysical Journal*, 253:908–920, 1982.

[187] Gregory M Harry, LIGO Scientific Collaboration, et al. Advanced ligo: the next generation of gravitational wave detectors. *Classical and Quantum Gravity*, 27(8): 084006, 2010.

[188] M Seglar-Arroyo, F Collaboration, et al. Gravitational wave alert follow-up strategy in the hess multi-messenger framework. *arXiv preprint arXiv:1705.10138*, 2017.

[189] RP Fender, GE Anderson, R Osten, T Staley, C Rumsey, K Grainge, and RDE Saunders. A prompt radio transient associated with a gamma-ray superflare from the young m dwarf binary dg cvn. *Monthly Notices of the Royal Astronomical Society: Letters*, 446(1):L66–L70, 2014.

[190] Stefan Ohm and Clemens Hoischen. On the expected γ-ray emission from nearby flaring stars. *in preparation*, 2017.

[191] DR Lorimer, Matthew Bailes, MA McLaughlin, DJ Narkevic, and Froney Crawford. A bright millisecond radio burst of extragalactic origin. *Science*, 318(5851):777–780, 2007.

[192] EF Keane, ED Barr, A Jameson, V Morello, M Caleb, S Bhandari, E Petroff, A Possenti, M Burgay, C Tiburzi, et al. The survey for pulsars and extragalactic radio bursts i: Survey description and overview. *arXiv preprint arXiv:1706.04459*, 2017.

[193] Rob Seaman, Roy Williams, Alasdair Allan, Scott Barthelmy, Joshua Bloom, John Brewer, Robert Denny, Mike Fitzpatrick, Matthew Graham, Norman Gray, et al. Ivoa recommendation: sky event reporting metadata version 2.0. *arXiv preprint arXiv:1110.0523*, 2011.

[194] Alasdair Allan and Robert B Denny. Voevent transport protocol version 1.1. *Note, International Virtual Observatory Alliance. VOEvent authentication via XML digital signature*, 2009.

[195] T. D. Staley. voevent-parse: Parse, manipulate, and generate VOEvent XML packets. Astrophysics Source Code Library, November 2014.

[196] John Swinbank. Comet: a VOEvent broker. *Astronomy and Computing*, 7:12–26, 2014.

[197] Thomas P Robitaille, Erik J Tollerud, Perry Greenfield, Michael Droettboom, Erik Bray, Tom Aldcroft, Matt Davis, Adam Ginsburg, Adrian M Price-Whelan, Wolfgang E Kerzendorf, et al. Astropy: A community Python package for astronomy. *Astronomy & Astrophysics*, 558:A33, 2013.

[198] Object Management Group. *The Common Object Request Broker (CORBA): Architecture and Specification*. Object Management Group, 1995.

[199] M Hauser, C Möllenhoff, G Pühlhofer, SJ Wagner, H-J Hagen, and M Knoll. ATOM–an Automatic Telescope for Optical Monitoring. *Astronomische Nachrichten*, 325(6-8): 659–659, 2004.

[200] Stefan Ohm, Christopher van Eldik, and Kathrin Egberts. Gamma-Hadron Separation in Very-High-Energy gamma-ray astronomy using a multivariate analysis method. *Astroparticle Physics*, 31:pp., 2009. URL `https://arxiv.org/abs/0904.1136`.

[201] Thomas Murach, Michael Gajdus, and Robert Daniel Parsons. A Neural Network-Based Monoscopic Reconstruction Algorithm for HESS II. *arXiv preprint arXiv:1509.00794*, 2015.

[202] Sebastian Funk. Online Analysis of Gamma-ray Sources with H.E.S.S. Master's thesis, Humboldt University Berlin, 2005.

[203] H.E.S.S. Collaboration. Increased VHE activity from PKS 1510-089 detected with H.E.S.S. ATel 9105, 5 2016.

[204] H.E.S.S. Collaboration. *2018-01-28*, ATEL 11239.

[205] H.E.S.S. Collaboration. H.E.S.S. follow-up of IceCube-160731A. ATel 9301, 8 2016.

[206] H.E.S.S. Collaboration. *2017-09-27*, ATel 10787.

[207] F. Aharonian et al. H.E.S.S. observations of gamma-ray bursts in 2003-2007. *Astronomy and Astrophysics*, 495:505, 2009. URL `https://arxiv.org/abs/0901.2187`.

[208] Clemens Hoischen, A Blazer, Elisabetta Bissaldi, Matthias Füßling, Tania Garrigoux, D Gottschalk, Markus Holler, Alison Mitchell, Paul O'Brien, Robert Parsons, et al. GRB Observations with HESS II. *arXiv preprint arXiv:1708.01088*, 2017.

[209] F Schüssler, M Backes, A Balzer, F Brun, M Füssling, C Hoischen, JP Lenain, M Lorentz, I Lypova, S Ohm, et al. The HESS multi-messenger program: Searches for TeV gamma-ray emission associated with high-energy neutrinos. In *AIP Conference Proceedings*, volume 1792, page 060006. AIP Publishing, 2017.

[210] Fermi-LAT Collaboration. *2017-09-28*, ATel 10791.

[211] IceCube Collaboration. *2017-09-23*, GCN 21916.

[212] IceCube Collaboration, Fermi-LAT Collaboration, MAGIC Collaboration, H.E.S.S. Collaboration, VERITAS Collaboration, et al. Multiwavelength observations of a flaring blazar Multiwavelength observations of a flaring blazar coincident with an IceCube high-energy neutrino. *Science*.

[213] VERITAS Collaboration. *2017-10-09*, ATel 10833.

[214] MAGIC Collaboration. *2017-10-04*, ATel 10817.

[215] J Lundberg, J Conrad, W Rolke, and A Lopez. Limits, discovery and cut optimization for a Poisson process with uncertainty in background and signal efficiency: TRolke 2.0. *Computer Physics Communications*, 181(3):683–686, 2010.

[216] D Eichler. High-energy neutrino astronomy-A probe of galactic nuclei. *The Astrophysical Journal*, 232:106–112, 1979.

[217] Paolo Padovani, E Resconi, P Giommi, B Arsioli, and YL Chang. Extreme blazars as counterparts of IceCube astrophysical neutrinos. *Monthly Notices of the Royal Astronomical Society*, 457(4):3582–3592, 2016.

[218] M Kadler, F Krauß, K Mannheim, R Ojha, C Müller, R Schulz, G Anton, W Baumgartner, T Beuchert, S Buson, et al. Coincidence of a high-fluence blazar outburst with a PeV-energy neutrino event. *Nature Physics*, 12(8):807, 2016.

[219] Markus Ackermann, Marco Ajello, WB Atwood, Luca Baldini, J Ballet, Guido Barbiellini, D Bastieri, J Becerra Gonzalez, R Bellazzini, E Bissaldi, et al. 2FHL: the second catalog of hard Fermi-LAT sources. *The Astrophysical Journal Supplement Series*, 222 (1):5, 2016.

[220] Scott P Wakely and Deirdre Horan. TeVCat: An online catalog for Very High Energy Gamma-Ray Astronomy. In *International Cosmic Ray Conference*, volume 3, pages 1341–1344, 2008.

[221] M Böttcher, A Reimer, K Sweeney, and A Prakash. Leptonic and hadronic modeling of Fermi-detected blazars. *The Astrophysical Journal*, 768(1):54, 2013.

[222] Shan Gao, Martin Pohl, and Walter Winter. On the direct correlation between gamma-rays and PeV neutrinos from blazars. *The Astrophysical Journal*, 843(2):109, 2017.

[223] The LIGO Scientific Collaboration and the Virgo Collaboration. *2017-08-18*, GCN Circ. 21509.

[224] M Coleman Miller. Gravitational waves: A golden binary. *Nature*, 551(7678):36, 2017.

[225] H Abdalla, A Abramowski, F Aharonian, F Ait Benkhali, EO Angüner, M Arakawa, M Arrieta, P Aubert, M Backes, A Balzer, et al. TeV gamma-ray observations of the binary neutron star merger GW170817 with HESS. *The Astrophysical Journal Letters*, 850(2):L22, 2017.

[226] von Kienlin et al. (Fermi-GBM Collaboration). *2017-08-17*, GCN Circ. 21520.

[227] The LIGO Scientific Collaboration and the Virgo Collaboration. *2017-08-17*, GCN Circ. 21513.

[228] Sheng Yang et al. (DLT40). *2017-08-18*, GCN Circ. 21531.

[229] Tanvir et al. (VISTA). *2017-08-18*, GCN Circ. 21576.

[230] Lipunov et al. (MASTER). *2017-08-18*, GCN Circ. 21546.

[231] Allam et al. (DESGW+community team). *2017-08-18*, GCN Circ. 21530.

[232] Arcavi et al. (Las Cumbres Observatory). *2017-08-18*, GCN Circ. 21538.

[233] Troya et al. (Chandra). *GCN Circ. 21765 and Nature in press*, 2017.

[234] Mooley et al. (JVLA/JAGWAR). *2017-09-04*, GCN Circ. 21814.

[235] Corsi et al. (VLA). *2017-09-04*, GCN Circ. 21815.

[236] G Dalya, Z Frei, G Galgoczi, P Raffai, and RS de Souza. VizieR Online Data Catalog: GLADE catalog (Dalya+, 2016). *VizieR Online Data Catalog*, 7275, 2016.

[237] Leo P Singer, Hsin-Yu Chen, Daniel E Holz, Will M Farr, Larry R Price, Vivien Raymond, S Bradley Cenko, Neil Gehrels, John Cannizzo, Mansi M Kasliwal, et al. Going the distance: Mapping host galaxies of LIGO and Virgo sources in three dimensions using local cosmography and targeted follow-up. *The Astrophysical Journal Letters*, 829(1):L15, 2016.

[238] A. Franceschini et al. Extragalactic optical-infrared background radiation, its time evolution and the cosmic photon-photon opacity. *Astronomy and Astrophysics*, 487 (3):837–852, 2008. ISSN 0004-6361. doi: 10.1051/0004-6361:200809691. URL `http://adsabs.harvard.edu/abs/2008A{%}26A...487..837F`.

[239] M. Wenger, F. Ochsenbein, D. Egret, P. Dubois, F. Bonnarel, S. Borde, F. Genova, G. Jasniewicz, S. Laloë, S. Lesteven, and R. Monier. The SIMBAD astronomical database. The CDS reference database for astronomical objects. *Astronomy and Astrophysics, Supplement*, 143:9–22, April 2000. doi: 10.1051/aas:2000332.

[240] Raffaella Margutti, KD Alexander, X Xie, L Sironi, BD Metzger, A Kathirgamaraju, W Fong, PK Blanchard, E Berger, A MacFadyen, et al. The Binary Neutron Star event LIGO/VIRGO GW170817 a hundred days after merger: synchrotron emission across the electromagnetic spectrum. *arXiv preprint arXiv:1801.03531*, 2018.

[241] Fermi LAT performance page, 05 2018. URL `https://www.slac.stanford.edu/exp/glast/groups/canda/lat_Performance.htm`.

Appendix A

Appendix

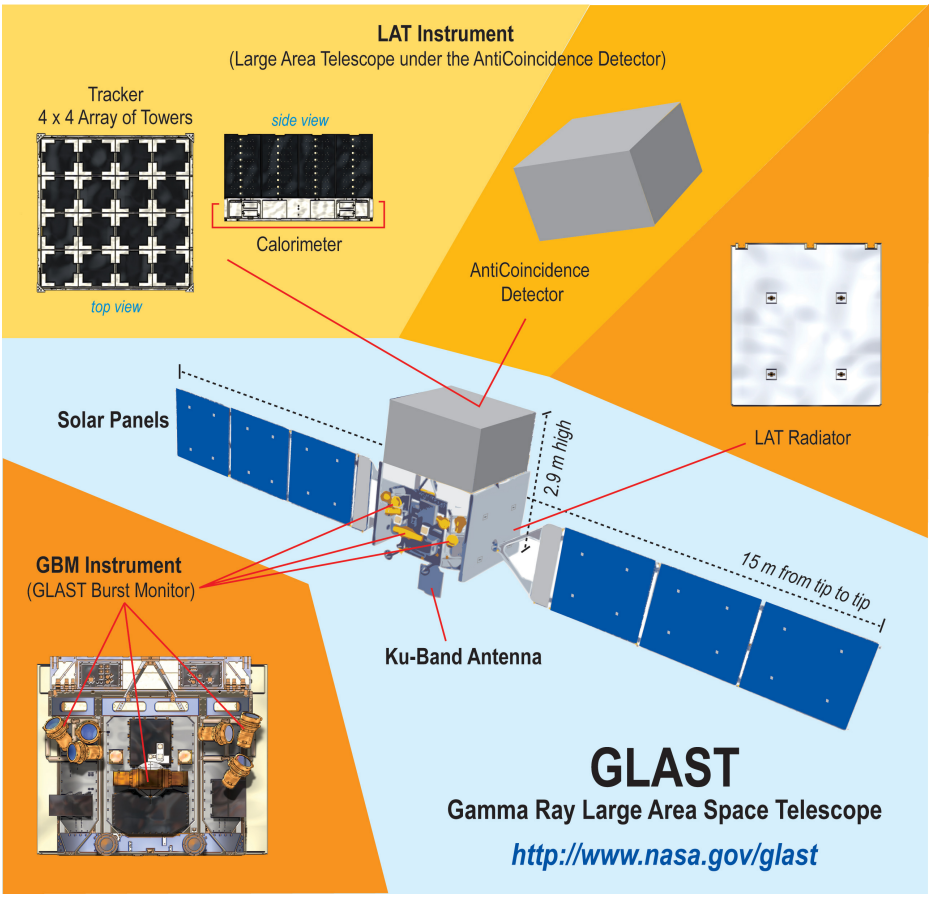

Figure A.1: Schematic overview of the different instruments on board the *Fermi* satellite.

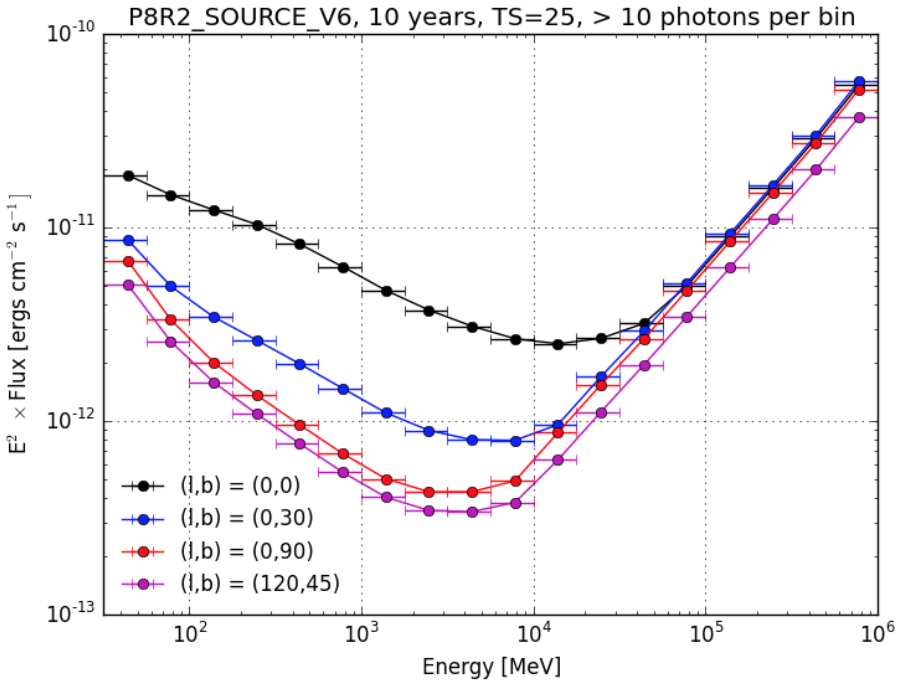

Figure A.2: Differential energy flux sensitivity of *Fermi*-LAT for different target regions, calculated for 10 years of observations of a point source with a spectral index of 2. Requirements on the minimum TS value of 25 and more than 10 photons in each energy bin have been applied. Close to the galactic plane, the sensitivity worsens due to the diffuse galactic emission which presents a background to other sources. The worsening of the sensitivity above 10 GeV corresponds to the lack in statistics at these energies. This figure has been taken from [241].

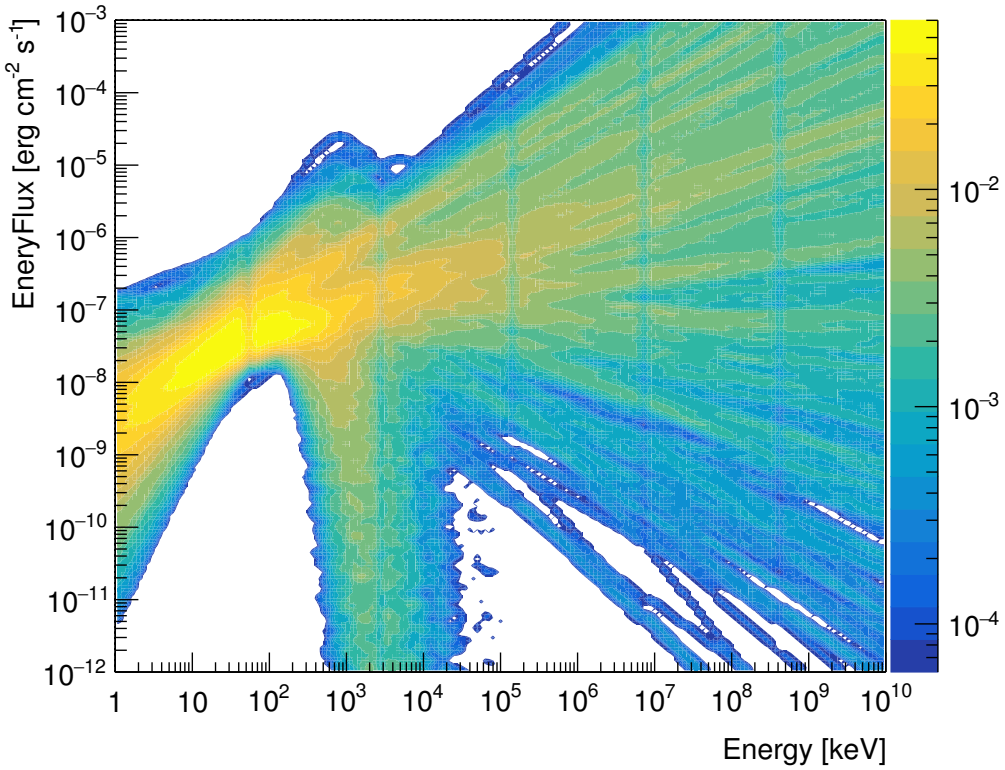

Figure A.3: Density profile of GBM detected time averaged best fit models based on the spectral parameters derived in the energy range from 10 to 1000 keV.

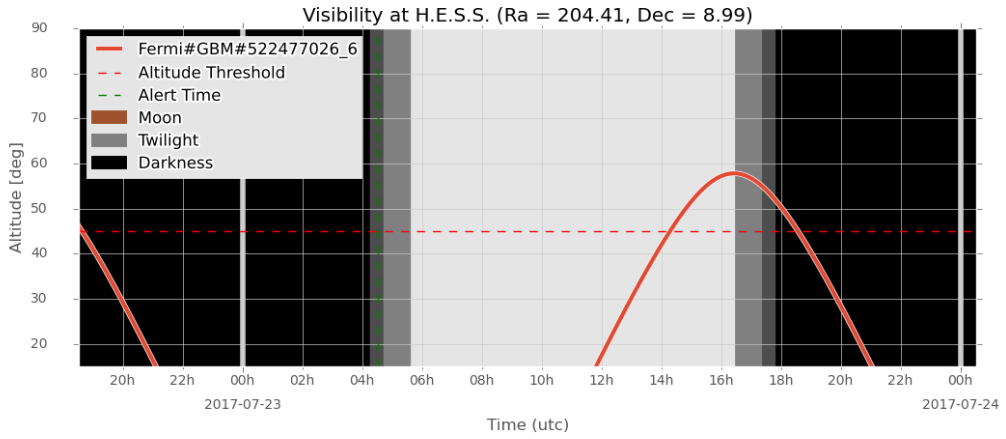

Figure A.4: Example for the graphical representation of a found follow-up window in the case of a Fermi-GBM Ground Position alert from July 2017. The green dashed line indicates the time of the event, black regions show the time in which the darkness requirements are met. The red solid line indicates the Altitude angle evolution as a function of time of the target position while the dashed red line shows the altitude threshold for this science case. The alert was received in a moonless night.

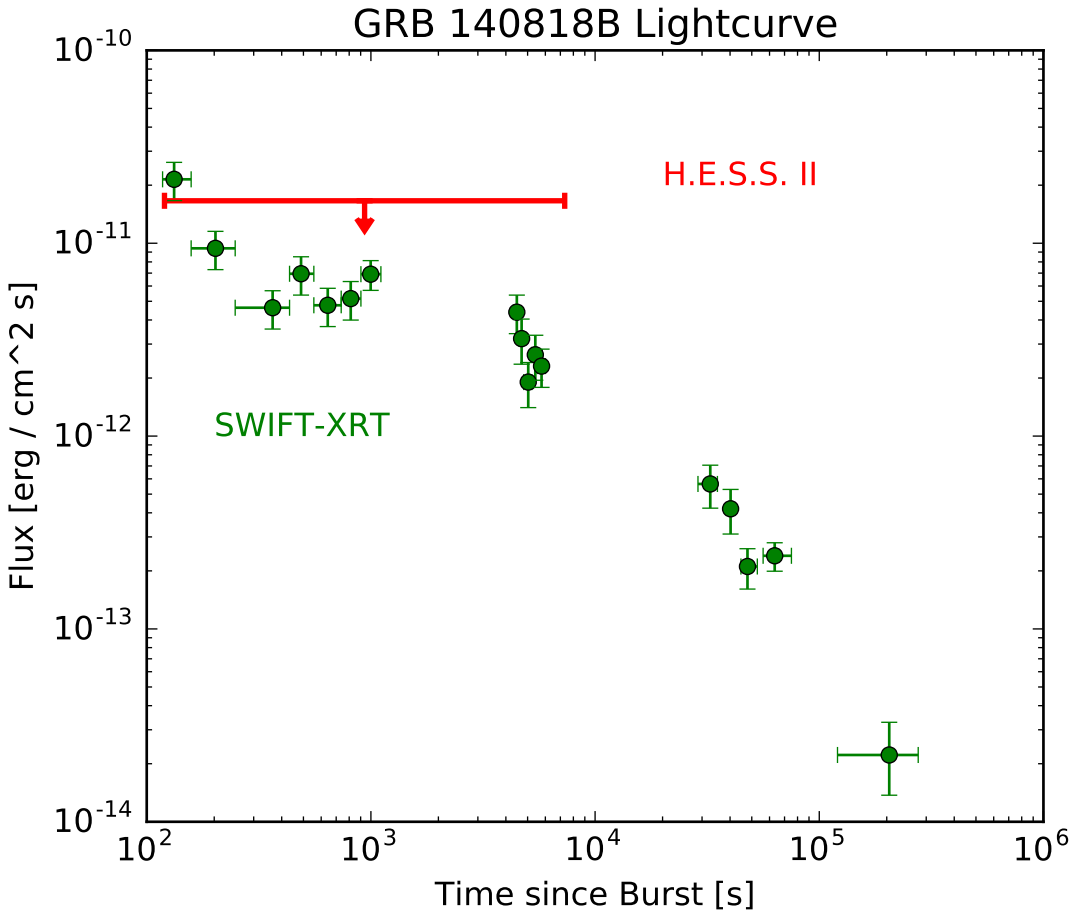

Figure A.5: H.E.S.S. upper limit from the follow-up observations of GRB140818B in comparison to the soft X-ray light curve measured by *Swift*-XRT.

Acknowledgments

My sincere thanks go to Christian Stegmann and Kathrin Egberts who made it possible for me to work with the exciting H.E.S.S. experiment. I thank Prof. Alexander Kappes and Prof. Martin Pohl for kindly agreeing to examine this work. Kathrin Egberts, Stefan Ohm, Matthias Füßling and Andrew Taylor proof read parts of this thesis, which greatly improved the quality of the text – thank you.

I want to express my sincere gratitude to all people who accompanied me over the past years. This includes many allies in the H.E.S.S. Collaboration as well as my Colleagues in Potsdam and Zeuthen. A special thank-you goes to:

- Kathrin, who excelled in supporting me in all my research efforts and was a strong ally in many discussions within the H.E.S.S. Collaboration.
- Matthias, who together with Arnim convinced me and supported me in the work with transients. The success of the novel alert system would not have been possible without their expertise.
- Stefan, who pointed me into the direction of star-forming systems. Beyond his expertise in this field, he played a key role to foster the transient activities within the H.E.S.S. Collaboration together with Matthias and me.
- I thank Eva, Constantin and Sergei for the productive office atmosphere as well as for the exchange about everyday technicalities and the many interesting conversations about non-physics matters.
- Martin, Helge, Stephan, Veronica and Gabor for the many enjoyable lunch breaks.
- Andrea and Ines for their excellent support with all formal matters of university and student life.

Finally I thank Johnsy, who was always there for me, endured my highs and lows throughout the years and always supported me. Likewise I thank my family. Thank you for always being there and your belief in me.